Carbon and sulphur isotopes in marine evaporites from the late Permian to Late Triassic, Yorkshire, UK

CHEUNG, HOI,DIK,ROSALIE,ASHLEIGH

Carbon and sulphur isotopes in marine evaporites from the late Permian to Late Triassic, Yorkshire, UK

Hoi Dik Rosalie Ashleigh Cheung

Thesis submitted in accordance with the regulations for the degree of

Master of Science (MSc) by Research in Geological Sciences

Department of Earth Sciences, Durham University

Under the supervision of Dr Darren R. Gröcke

and Professor H. Chris Greenwell

March 2021

Research conducted at:

Department of Earth Sciences

Durham University, Durham, DH1 3 LE

Abstract

Seawater sulphate has been used widely as a tool for palaeoceanographic reconstructions, but more recently it has been used for stratigraphic correlation. The sulphur isotope ratio ($\delta^{34}S$) of seawater is controlled predominantly through evaporite and/or pyrite formation and burial. $\delta^{34}S$ can be measured from evaporites, pyrite, and carbonate-associate-sulphate (CAS). Organic carbon isotope ratios ($\delta^{13}C$) have been widely used for stratigraphic purposes in geologic time. In this study, a marine sulphur and organic carbon isotope curve are produced from 389 evaporite/sediment samples from the Staithes S-20 borehole, Yorkshire, UK, which spans the late Permian to Late Triassic time interval. The $\delta^{34}S$ and $\delta^{13}C$ curves produced in this study are used to ascertain their use for stratigraphic correlation of Triassic sedimentary successions in the UK which are poorly dated due to the type of depositional environment. The Permian–Triassic boundary that records a major negative $\delta^{13}C$ excursion and positive $\delta^{34}S$ excursion are not recorded in the Staithes S-20 core due to a major hiatus in the upper Sherwood Sandstone Group. The $\delta^{34}S$ data indicate that the Sherwood Sandstone Group is dominantly latest Permian in age in this region and only the uppermost part of the group is Early Triassic in age. The Mercia Mudstone Group ranges in age from the Middle to Late Triassic and provide additional data to fill in major gaps in the global $\delta^{34}S$ curve — which will aid in global correlation as the general undated Staithes-20 core do not allow a detailed sedimentary correlation with other sections of the UK. Although the results from this study are promising, more Triassic cores from around the UK need to be analysed to better understand and constrain the lithostratigraphic relationships that are currently used to correlate Triassic sequences. Additional isotopic analyses (e.g, strontium isotopes) can be performed on the evaporite samples for a more accurate correlation. The combined application of biostratigraphy, sedimentology and chemostratigraphy will help to track the overall changes of marine

sulphate, carbon and pO2, thus develop a greater understanding of the climate and environment of the Triassic.

Keywords: stable isotope stratigraphy, sulphur isotopes, carbon isotopes, evaporites, Triassic, late Permian, Sherwood Sandstone Group, Mercia Mudstone Group

Acknowledgements

I would like to thank my supervisors, Dr Darren Gröcke and Professor Chris Greenwell for their endless contribution, support, guidance and discussions throughout the research, and the continuous support within the Department of Earth Sciences at the University of Durham. I would like to express my gratitude to Durham University for offering the facilities that are required for this project, especially the Stable Isotope Biogeochemistry Laboratory (SIBL) for carrying out analyses and Palaeoecology Laboratory for chemical precipitations of my samples. I thanked Dr Darren Gröcke, the Director of SIBL, for his guidance during my sample preparation. I also thank Mr Ian Chaplin and Miss Sophie Edwards for preparing thin section samples at the Department of Earth Sciences. I also would like to thank the British Geological Survey in Keyworth, Nottinghamshire, to provide access to drill cores for this study. Dr Geoffrey Warrington is thanked for personal communications throughout the project regarding the palynological information. Furthermore, I am very grateful for the support from other postgraduates in my working environment in the annex, Catriona Sellick, Christos Vasilopangos, Hector Escamilla-Garcia, Lauren Kancle, Mohammad Daud Hamidi, Nikolaos Apeiranthitis, Yu Emma Harasawa for shaping a wonderful and comfortable environment to work. Finally, thank you to all my friends, family, relatives and for all the paper I had around me during this year for their invaluable support and encouragements.

Declaration

I confirm that material contained in this thesis has not been previously submitted for a degree by me or any other institution. When relevant, materials from the work of others have been acknowledged.

Hoi Dik Rosalie Ashleigh Cheung, March 2021.

Statement of Copyright

Hoi Dik Rosalie Ashleigh Cheung, March 2021.

Table of Content

List of Figures

1. Introduction

Ancient sediments provide a record of carbon and sulphur isotope ratios, which allows us to interpret the state of carbon and sulphur cycles throughout geological history (Newton and Bottrell, 2007). Stable isotope (e.g., carbon, sulphur, oxygen and strontium) composition of the ancient ocean has been reconstructed since the 1970s and have become increasingly useful as a stratigraphic tool for correlation and dating. Stable isotope stratigraphy is often combined with other dating proxies (e.g., biostratigraphy, palynology and magnetostratigraphy) in order to establish accurate stratigraphic timescales in the geological record. Abundance biostratigraphic fossils are particularly effective for sequence stratigraphy studies and can be used to correlate and establish the approximate timescale for the sediments which spread across a large area with similar lithologies. The higher resolution the record is, the higher the level of confidence the record.

Throughout the geological history, each time interval is characterised by distinct range of isotope values which change overtime as a result of global climate and environmental disturbances. Distinct isotopic trends (positive/negative) can be correlated by wiggle-matching patterns between different sedimentary sections around the world (Fang *et al.*, 2013) and is very useful for lithostratigraphic correlation. Shifts in the isotopic curve through time record changes of the global isotope cycling processes (Newton and Bottrell, 2007), thus reflect the relative changes in both geological and biogeochemical systems.

Figure 1. The Triassic chronostratigraphic timescale modified after Lucas (2010).

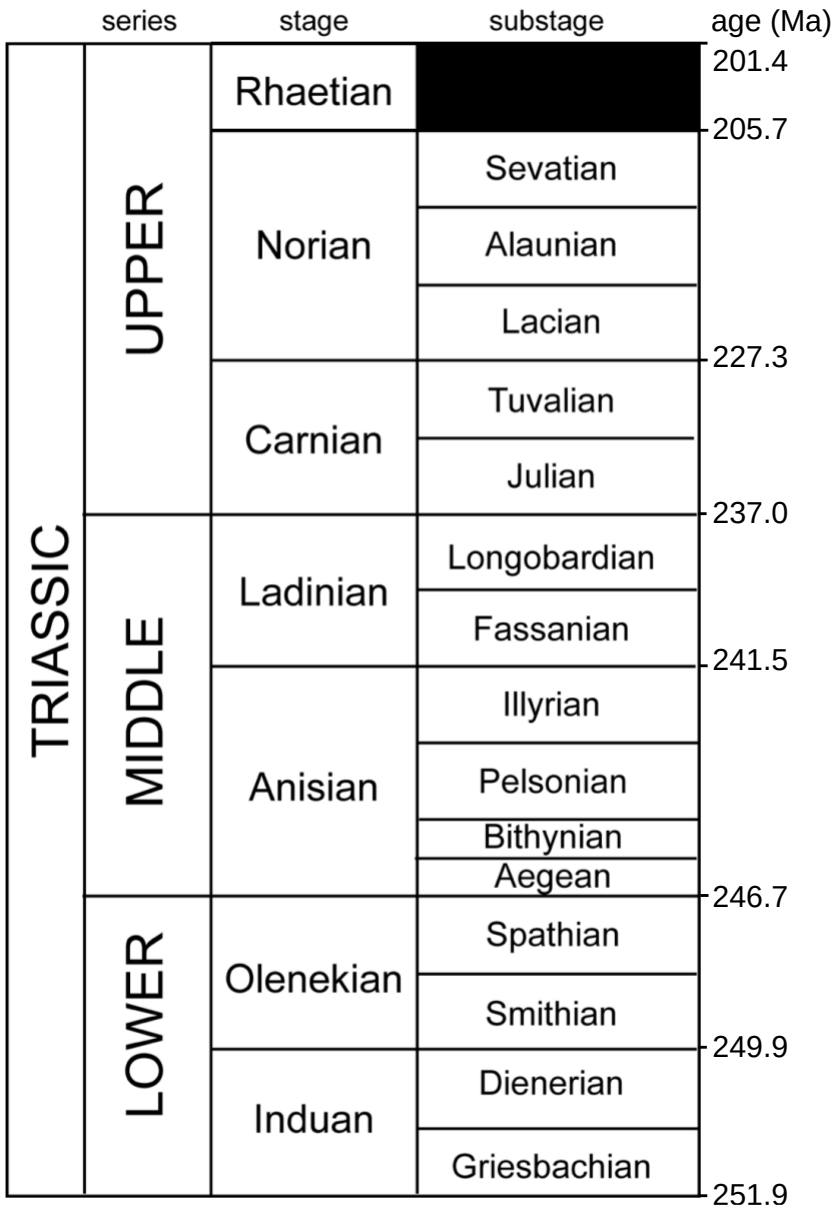

Figure 1 shows the Triassic timescale used in this research. The Triassic of the UK has been intensely studied for many decades, but the majority of our understanding on stratigraphy is solely based on lithostratigraphic relationships, which are not ideal for accurately correlating and dating sediments. This lack of age constraint hinders our wider understanding of climate and environment in the Triassic. In addition, the British Triassic evaporite sequences are difficult to date due to the lack of biostratigraphic useful fossils

and the discontinuous or poorly preserved nature of these sequences. Although there are some palynology and biostratigraphic evidence which give an age constrain indication for the Triassic sediments (see chapter 4 and 5), the British Triassic sediments in our study area (North East Yorkshire) are generally undivided hence it is difficult to correlate based on biostratigraphy and establish an approximate age. However, sulphur and carbon isotope stratigraphy may be a viable technique for stratigraphic correlation in these sedimentary environments. For example, Caruthers *et al.* (2018) demonstrated that $\delta^{13}C$ analysis of organic matter preserved in Silurian evaporite sequences in the Michigan Basin record a global marine signal.

Sulphur isotope ($\delta^{34}S$) stratigraphy has been used to reconstruct global carbon and sulphur biogeochemical cycles on Earth, and recently used as a stratigraphic tool for correlating sections around the world (Paytan *et al.*, 2011; Bernasconi *et al.*, 2017). The Permian/Triassic boundary (PTB) at ~252 Ma marks the transition from the Palaeozoic to Mesozoic Era and also the largest extinction event recorded in the Phanerozoic (Song *et al.*, 2018). The marine sulphur cycle has been severely affected as shown by a large positive shift in $\delta^{34}S$ record across the PTB (see Figure 5) (Claypool *et al.*, 1980; Cortecci *et al.*, 1981; Kaiho *et al.*, 2001; Korte *et al.*, 2004; Newton *et al.*, 2004; Insalaco *et al.*, 2006; Horacek *et al.*, 2010). In contrast, the $\delta^{13}C$ record across the PTB is marked by a pronounced negative excursion (Figure 7) (Korte *et al.*, 2004; Payne *et al.*, 2004; Corsetti *et al.*, 2005; Horacek *et al.*, 2007; Algeo *et al.*, 2008; Horacek *et al.*, 2010; Luo *et al.*, 2010; Sanson-Barrera *et al.*, 2013). The large and rapid $\delta^{34}S$ excursion across the PTB has been proposed to be caused by increased pyrite burial into the Early Triassic related to widespread global anoxia (Newton *et al.*, 2004). The subsequent Early Triassic is characterised with large fluctuations of negative and positive carbon isotope excursions (CIEs) (Figure 7) (Payne *et al.*, 2004; Horacek *et al.*, 2007; Meyer *et al.*, 2013; Sanson-

Barrera *et al*., 2013; Song *et al*., 2014; Caravaca *et al*., 2017; Stebbins *et al*., 2019), which is an indicative of environmental instability (Payne *et al*., 2004), including widespread anoxia, sea-level fluctuation, and low diversity ecosystems (Newton *et al*., 2004; Algeo *et al*., 2011).

Although the large fluctuation in $\delta^{13}C$ and $\delta^{34}S$ across the PTB has been recognised globally, previous studies have mainly focused on the PTB and Early Triassic interval in comparison to the Middle and Late Triassic time intervals (see Figure 5 and 7) (e.g., Boschetti *et al*., 2005; Boschetti *et al*., 2011; Bernasconi *et al*., 2017). Recently, Bernasconi *et al*. (2017) has produced and extended a high-resolution marine evaporite $\delta^{34}S$ curve from portions of the Middle and Late Triassic in Northern Switzerland (Jura Mountains) (Figure 5). Bernasconi *et al*. (2017) also integrated evaporite $\delta^{34}S$ records from previous studies (Cortecci *et al*., 1981; Pearson *et al*., 1991; Worden *et al*., 1997; Fanlo and Ayora, 1998; Insalaco *et al*., 2006; Longinelli and Flora, 2007; Horacek *et al*., 2010; Boschetti *et al*., 2011). Additionally, a global compilation of evaporite $\delta^{34}S$ through geologic time has been compiled by Present *et al*. (2020), which shows that there are significant gaps in the record, especially in the Late Triassic (see Figure 5). Although there are gaps in the evaporite $\delta^{34}S$ record, the possibility of using sulphur isotope stratigraphy as a correlation tool globally has been demonstrated for Cenozoic sedimentary sequences (e.g., Paytan *et al*., 2020). The driving mechanism of this research is to build on the evaporite Triassic $\delta^{34}S$ curve and its application as a stratigraphic correlation tool.

1.1 Chemostratigraphy

The study of stable isotope geochemistry is useful to correlate different sedimentary sections around the world and to investigate environmental changes in both the ancient ocean and atmosphere (Saitoh *et al*., 2014).

Other isotopic systems such as nitrogen, oxygen, strontium as well as elemental analysis (e.g., Fe, Mg, Sr, Na, and Th/U ratios) are often present together to provide new insights to calibrate the PTB extinction event from the geochemical aspects (Tavakoli, 2015) thus reflect the changes in the global cycling processes of different isotope content.

For example, strontium isotope stratigraphy of the Permian and Triassic has been thoroughly investigated by Veizer and Compston (1974); Burke *et al*. (1982); Brookins (1988); Kramm and Wedepohl (1991); Spötl and Pak. (1996); Kampschulte *et al*. (1998), Korte *et al*. (2004) and Tavakoli (2015). Variations in strontium isotope composition of the ocean reservoir reflects the relative ratio between weathering fluxes and the input of strontium from mantle/hydrothermal source. Figure 2 shows the general trend of the decrease in marine $^{87}Sr/^{86}Sr$ values throughout the Permian seawater, from 0.7080 at the earliest Permian to a minimum of 0.7069 at the latest Permian. This was probably caused by the extremely low rates of continental runoff and BSR, indicated as the onset of the supercontinent, Pangaea break up (Kani *et al*., 2008), initiation of a mantle plume (Isozaki, 2009), cessation of basaltic volcanism, the humidification of Pangaea (Korte *et al*., 2006). This is followed by a slight increase in $^{87}Sr/^{86}Sr$ values from the upper Permian to the PTB, with values of 0.7071 to 0.7072, and continues into Early Triassic, up to Middle Triassic (Anisian) age (Korte and Ullmann, 2018). The rise of strontium isotope values is suggested to be related to the enhanced continental weathering under humid climatic conditions from the uppermost Permian and the lack of vegetation land prior to

Spathian (Korte *et al*., 2004). The $^{87}Sr/^{86}Sr$ ratio begin to have a sharper rise in Early Triassic, the increase can be due to a change within the strontium cycle, with the interplay of increase continental strontium flux into the ocean therefore increasing the strontium isotope ratios as well as a reduction in hydrothermal activities (Korte and Ullman, 2018).

Figure 2. $^{87}Sr/^{86}Sr$ record from the latest Carboniferous to Early Triassic, showing a general decrease in $^{87}Sr/^{86}Sr$ values from the early Permian to late Permian, in prior to the rapid increase at/near the Permian-Triassic boundary, into the Early Triassic times. (Korte and Ullmann, 2018)

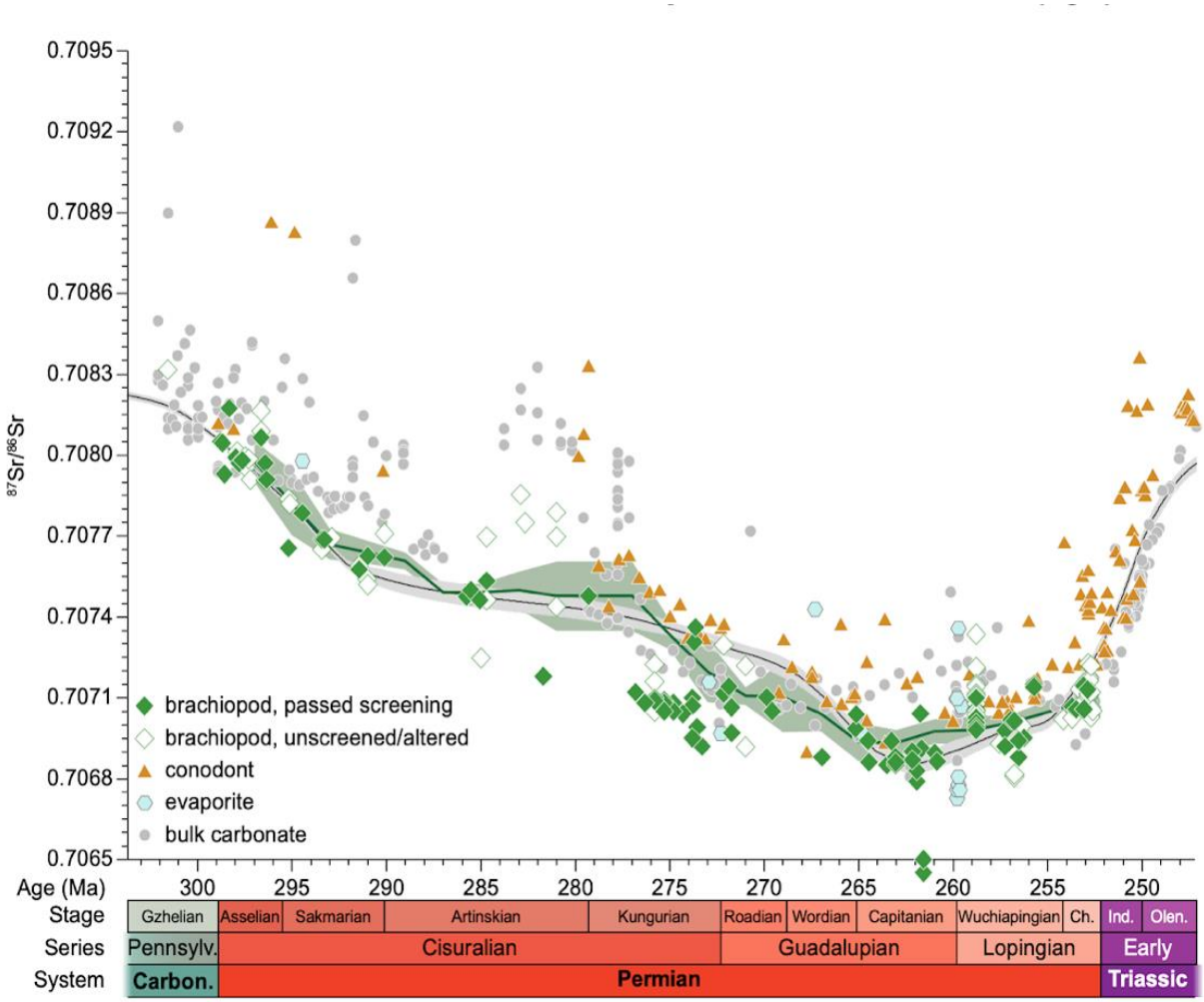

The Earth's oceanic nitrogen cycle has also been significantly affected through the geologic time. Throughout the latest Permian, there is a progressive decline in the $\delta^{15}N$ record, with the negative $\delta^{15}N$ values persist into the Early Triassic. This can be correlated globally, such as in India (Algeo et al., 2007) and South China (Cao et al., 2009; Luo et

al., 2011). Knies et al. (2013) correlated a negative $\delta^{15}N$ shift around the PTB extinction boundary at Buchanan Lake (Texas) to that in Meishan (China). The negative $\delta^{15}N$ trend is suggested to reflect the ecological disturbance and a nitrogen cycle with reduced involvement of oxidised substances (nitrate and nitrite) and increased nitrogen fixation, induced by euxinia in the aftermath of the PTB extinction event (Altabet and Francois, 1994; Cao et al., 2009).

Changes in the Th/U ratio during the latest Permian might also indicate an anoxic environment, which is followed by a rapid decline in the oxygen content across the PTB. The decline in the $\delta^{18}O$ record in the Early Triassic can be explained by the increase of the iron flux entering the oceans during an anoxic episode, which is suggested to be triggered by the demise of land plants (Newton et al., 2004; Tavakoli, 2015).

1.2 Aim and objectives

In this study, bulk sedimentary organic carbon isotope ratios ($\delta^{13}C$) and evaporite sulphur isotope ratios ($\delta^{34}S$) are generated for the Staithes S-20 borehole in the Cleveland Basin, North East Yorkshire, England, UK. A total of 389 core samples from Staithes S-20 were sampled from the Keyworth Core Facility at the British Geological Survey. This study will focus on the application of sulphur isotope ratios ($\delta^{34}S$) of marine sulphate (SO_4^{2-}) from evaporitic sedimentary deposits as a palaeo-seawater proxy for the marine sulphur cycle. The hypothesis is that changes in the $\delta^{34}S$ curve can be used as a stratigraphic tool for correlation of late Permian (Lopingian) to Late Triassic (Rhaetian) sequences in the UK that are poorly constrained chronologically.

The objectives of this study are:

1. To produce a stratigraphic isotope curve for sulphur and carbon isotope ratios from the Staithes S-20 core, spanning the late Permian to Late Triassic time interval.
2. To revise the correlation of sedimentary sequences between British and European successions in the Triassic using isotope stratigraphy.

2. The Sulphur Cycle

Sulphur has four stable isotopes: ^{32}S, ^{33}S, ^{34}S and ^{36}S, with natural abundances of 95.02%, 0.75%, 4.21% and 0.02%, respectively (MacNamara and Thode, 1950). Sulphur isotope ratios are expressed in standard delta notation ($\delta^{34}S$) in per mil (‰), against an international standard (Vienna Canyon Diablo Troilite, VCDT) (Bottrell and Newton, 2006) using the following equation:

$$\delta^{34}S = [((^{34}S/^{32}S)_{sample} - (^{34}S/^{32}S)_{standard}) / (^{34}S/^{32}S)_{standard}] \times 1000 \text{ VCDT}$$

The sulphur element is an important constituent of the Earth's exogenic cycle. Sulphur, in the form of sulphate (SO_4^{2-}) is the second most abundant anion in modern marine environments and plays a major role in the chemical composition of the ocean (Paytan and Gray, 2012). Sulphur occurs in either its oxidised form (dissolved sulphate in seawater and evaporitic sulphate), or reduced form as sedimentary sulphide (pyrite) (Gill *et al*., 2007; Newton and Bottrell, 2007; Paytan and Gray, 2012). The sulphur isotope ratio is ultimately controlled by relative changes between volcanism, weathering and burial (evaporite and pyrite) rates (Paytan *et al*., 2004; Gill *et al*., 2007; Paytan and Gray, 2012; Bernasconi *et al*., 2017).

Pyrite burial is the major sink of sulphur in the ocean (Figure 3 and 4). Pyrite forms through reaction processes between hydrogen sulphide (H_2S) and detrital iron-bearing minerals in anoxic conditions via bacterial sulphate reduction (BSR) (Berner, 1970; Berner 1984). During BSR, when marine sulphate transforms into sulphide (pyrite), the lighter isotope, ^{32}S, is preferentially utilised. Since ^{32}S has a more rapid reduction rate

(Newton and Bottrell, 2007), this leaves the residual sulphate reservoir enriched in the heavier isotope, ^{34}S (Gill *et al.*, 2007). BSR has strong isotopic fractionation (ranging from –70‰ to 15‰) and can be explained by redox cycling and associated disproportionation reactions (Canfield and Thamdrup, 1994; Habicht and Canfield, 1996; 1997; 2001). The $\delta^{34}S$ composition of pyrite displays a wide range of isotope values which may reflect the biogeochemical conditions during its formation in anoxic conditions via BSR. Pyrite $\delta^{34}S$ has been used to track the biogeochemical properties of the sulphate reservoir and redox conditions in the oceans (Detmers *et al*., 2001; Canfield, 2001; Habicht and Canfield, 2001).

The largest input of sulphate into the modern ocean including from riverine/continental weathering ($\delta^{34}S \cong 0–10‰$), volcanism ($\delta^{34}S \cong 0–3‰$) and hydrothermal sources ($\delta^{34}S \cong 0–3‰$) (Figure 4) (Newton and Bottrell, 2007). The removal of sulphur or sulphate from the ocean reservoir are through precipitation of evaporite sulphates during evaporite deposition ($\delta^{34}S_{evap} \cong \sim16‰$)) and burial of sedimentary pyrite ($\delta^{34}S_{pyrite} \cong –15‰$) (Figure 2 & 3; Paytan *et al.*, 2011; Strauss, 1997). The precipitation of sulphate minerals through marine evaporite formation only has minor isotopic fractionation (0‰ to 3‰), and hence does not have a significant effect on the marine reservoir (Holser and Kaplan, 1966).

Figure 3. Main reservoir for marine sulphur cycle, BSR= Bacterial sulphate reduction (from Holser et al., 1989).

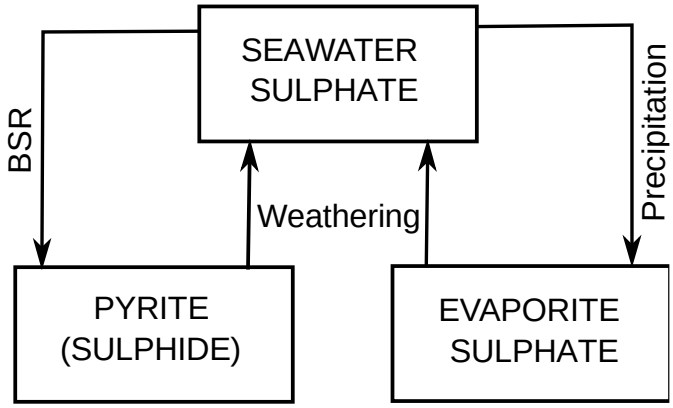

The modern marine sulphur reservoir size is estimated as 1.3 x 10^{21} g (Newton and Bottrell, 2007) with $\delta^{34}S$ value of ~21‰ (Figure 4), at an analytical precision of ±0.2‰ (Rees *et al*., 1978). The enriched $\delta^{34}S$ in buried evaporite sulphates ($\delta^{34}S \cong$ ~16‰) with 3 x 10^{21} g of sulphur in the modern ocean can be balanced out by the pyrite reservoir ($\delta^{34}S \cong$ –12‰). The residence time of marine sulphate is closely linked to the size of the marine reservoir. Due to the large ocean reservoir (1.3×10^{21} g) with respect to the small sulphate fluxes (10×10^{13}g yr^{-1}), marine sulphate has a very long residence time, close to 10 Myrs and ranges from 13 to 20 Myrs depending on the estimate fluxes, with a sulphate concentration of 28 mM (Bottrell and Newton, 2006; Paytan and Gray, 2012; Algeo *et al*., 2015). Therefore, the sulphur isotope composition of the ocean is assumed to be homogeneous with respect to the dissolved sulphate in ocean at any given time. Such uniformity is expected due to the long residence time of sulphur in oceans (up to 12 Myrs), which far exceeds the oceanic mixing time (1–10 kyrs) (Paytan and Gray, 2012). Because of the long residence time of sulphate, the $\delta^{34}S$ of modern seawater sulphate cannot change at a rate faster than the estimated maximum value of 1.1‰ per million year (Algeo *et al*., 2015; Bernasconi *et al*., 2017). However, the residence time of sulphur in ocean oceans may have had fluctuating residence times (e.g., Algeo *et al*., 2015).

Figure 4. Schematic diagram of the pre-industrial global sulphur cycle (adapted from Newton and Bottrell, 2007).

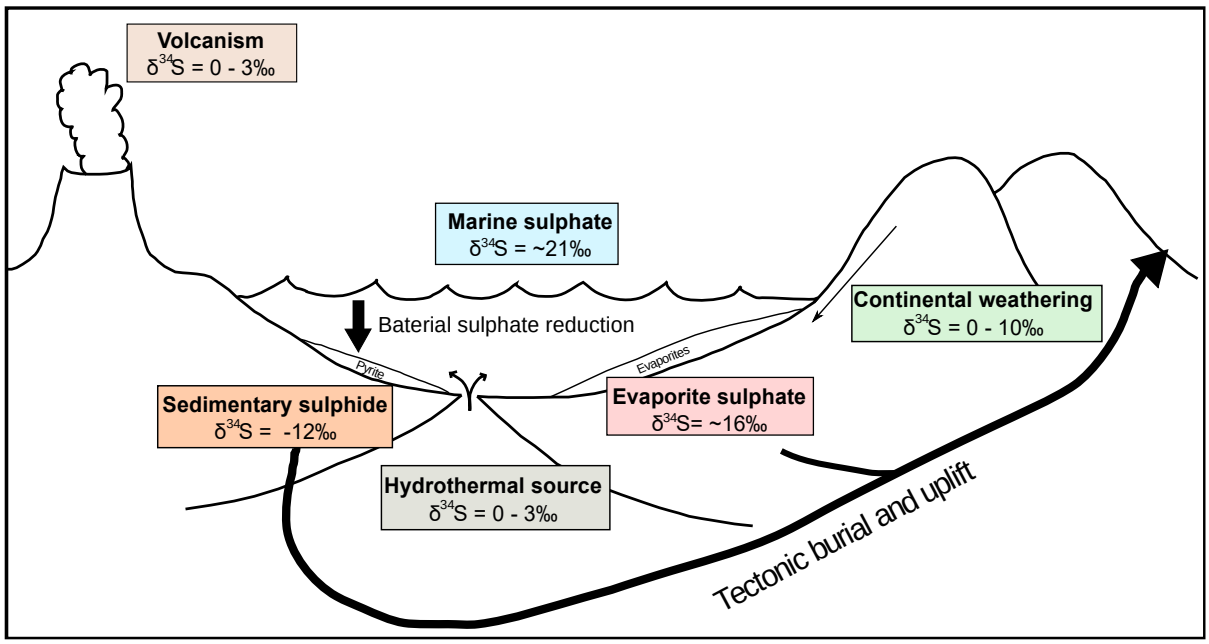

2.1 The Sulphur Isotope Curve

The $\delta^{34}S$ composition of seawater sulphate can be obtained from sulphate-bearing minerals such as, anhydrite ($CaSO_4$), gypsum ($CaSO_4 \cdot 2H_2O$), barite ($BaSO_4$), pyrite (FeS_2) and carbonate-associated sulphate (CAS). Evaporites, such as anhydrite and gypsum contain up to 20 wt% sulphate, show minimal isotopic fractionation from seawater and hence, are ideal proxies for the isotopic composition of seawater sulphate in the geological record (Paytan and Gray, 2012). A marine evaporite $\delta^{34}S$ curve through geological history was first produced during the late 1960's to early 80's (e.g., Holser and Kaplan, 1966; Holser 1977; Claypool *et al.*, 1980). The marine $\delta^{34}S$ record has been used extensively to monitor global changes in the biogeochemical sulphur cycle on Earth (Berner and Berner, 1987; Krouse and Grinenko, 1991). However, more recently, it has been applied as a tool for stratigraphic correlation and relative dating (Paytan *et al.*, 2011; Bernasconi *et al.*, 2017).

One of the biggest challenges of using $\delta^{34}S$ stratigraphy as a correlation tool is the age resolution of the dataset. For example, there are scarce Proterozoic evaporites in South Africa (Cameron, 1982). Additionally, post-depositional alternation (Marenco *et al*., 2008a, b), reservoir effect during crystallisation (Holser and Kaplan, 1966; Alonso-Azcarate *et al*., 2006), and redox cycling of sulphur (Alonso-Azcarate *et al*., 2006), can alter a primary sulphur isotope signature. However, through careful screening and assessment of the mineralogy, diagenesis and elemental composition of the evaporite under investigation will minimise these risks. In addition, sedimentological assessments are required to ascertain that the sulphate minerals being deposited are not post-depositional and/or deposited under non-marine conditions.

Having said that, recent compilations by Crockford *et al*. (2019) and Present *et al*. (2019) have provided more detail to the record, but the overall pattern of the curve has not change in that much detail (see Figure 5). The $\delta^{34}S$ composition of evaporites is characterised by an increase from the Late Proterozoic (18‰) to the pre-Cambrian (35‰), followed by a decrease throughout the Palaeozoic, reaching the lowest of 10‰ in late Permian (Claypool *et al*., 1980). The $\delta^{34}S$ record is then interrupted with a sharp increase at the Early Triassic, continuing into the Cretaceous and experienced a small decrease to ~14‰, and is followed by an increase trend to the present-day $\delta^{34}S$ value of ~21‰ (Yao *et al*., 2019).

Figure 5. (Left) Records of Phanerozoic marine sulphate $\delta^{34}S$ reconstructed from proxy materials (data obtained from Present et al., 2020). (Right) Global marine $\delta^{34}S$ from late Permian (Lopingian) to Late Triassic (Norian) reconstructed from evaporites (Bernasconi et al., 2017; Present et al., 2020).

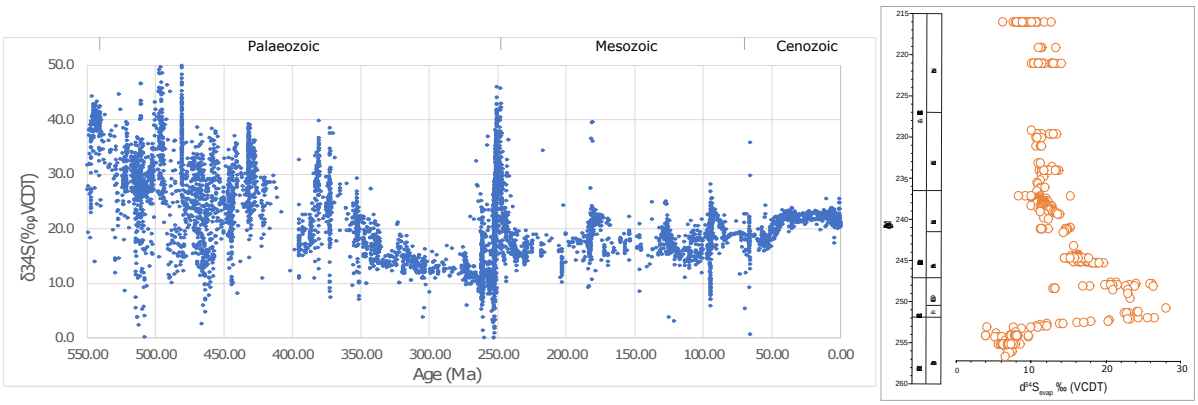

In terms of this study, there have been many sulphur isotope investigations on the PTB and Early Triassic time intervals (e.g., Cortecci *et al.*, 1981; Naylor *et al.*, 1989; Kramm and Wedepohl, 1991; Spötl and Pak, 1996; Worden *et al.*, 1997; Kampschulte *et al.*, 1998; Song *et al.*, 2014; Insalaco *et al.*, 2006; Longinelli and Flora, 2007; Horacek *et al.*, 2010; Peryt *et al.*, 2010; Bernasconi *et al.*, 2017).

It has long been recognised that evaporite $\delta^{34}S$ reached its lowest value (~10‰) in the latest Permian (Peryt *et al.*, 1998; Peryt *et al.*, 2005, 2010). Nine Zechstein evaporite samples from northwest Germany have recorded $\delta^{34}S$ values from 10.7‰ to 11.5‰ (Kramm and Wedepohl, 1991). Upper Permian gypsums recorded $\delta^{34}S$ values of 11.5‰ from the Carniola di Bovegno Formation (Bergamo and Brescia Alps) and the lower part of the Gracilis Formation (Recoaro, Vicenza) (Cortecci *et al.*, 1981), which are in good agreement with those obtained by Pak (1978), with $\delta^{34}S$ values of 9.5‰ to 11.5‰ in Italy and those from Kampschulte *et al.* (1998) with fifty-nine evaporites samples obtained from northern Germany, with a mean value of 11‰. Twelve evaporite sulphate samples from the Zechstein core in Northern Germany recorded an average $\delta^{34}S$ values of 10‰

to 14‰ (Herrmann *et al*., 1967), similar to those obtained by Spötl and Pak (1996), with $\delta^{34}S$ values between 9.8‰ to 13.8‰. Additional sulphate evaporite data from the Southern Alps (Longinelli and Flora, 2007) and Germanic Zechstein (Spötl and Pak, 1996; Kampschulte *et al*., 1998; Peryt *et al*., 2010) exhibit $\delta^{34}S$ values between 10‰ and 15‰. The overall average $\delta^{34}S$ values of 11‰ in late Permian is in close agreement to those obtained from the Persian Gulf (Insalaco *et al*., 2006) and Abu Dhabi (Worden *et al*., 1997), which represents a highly accurate position of the PTB (Bernasconi *et al*., 2017).

The $\delta^{34}S$ record across the PTB and earliest Triassic is interrupted by a large positive shift up to ~30‰ (e.g., Kaiho *et al*., 2001; Korte *et al*., 2004; Claypool *et al*., 1980; Cortecci *et al*., 1981; Newton *et al*., 2004; Horacek *et al*., 2010; Insalaco *et al*., 2006). An abrupt rise in the $\delta^{34}S$ record from the latest Permian to 32‰ at the base of middle Induan is recorded in northern Italy (Horacek *et al*., 2010). Additionally, anhydrite sulphate data from the Persian Gulf recorded $\delta^{34}S$ values of ~8‰ at the PTB, followed by a sharp increase to 30‰ in the Dienerian (Insalaco *et al*., 2006), and a 10‰ rise at the PTB in Abu Dhabi (Worden *et al*., 1997). However, this positive $\delta^{34}S$ excursion gradual declined to values on the order of ~16‰ during the Olenekian (e.g., Cortecci *et al*., 1981; Utrilla *et al*., 1992; Luo *et al*., 2010; Bernasconi *et al*., 2017).

During the early Anisian, the $\delta^{34}S$ composition of seawater sulphate experienced another rapid rise to ~28‰, which has been recorded globally in Italy (Cortecci *et al*., 1981), Austria (Spötl and Pak, 1996); South China (Luo *et al*., 2010) and northern Switzerland (Bernasconi *et al*., 2017). Holser (1977) originally named this rapid rise as the 'Röt-Event', as documented in the evaporites sequence of the Röt Member in Europe (Nielsen

and Rickle, 1964; Nielsen, 1965). Recent biostratigraphy and magnetostratigraphy have confirmed the Röt Member as lower Anisian (Szurlies, 2007).

The Late Triassic $\delta^{34}S$ curve is relatively constant, ranging from 15‰ to 17‰ (Cortecci *et al.*, 1981). Cortecci *et al.* (1981) obtained $\delta^{34}S$ values of ~16‰ in Italy, similar to those from the Alps (Longinelli and Flora, 2007), the Adriatic region and northern Switzerland (Rick, 1990; Bernasconi *et al.*, 2017). Nine evaporite samples from northern Apennines show a mean $\delta^{34}S$ value of 15.5‰ for the Upper Triassic (Boschetti *et al.*, 2011). Furthermore, Upper Triassic evaporites obtained from Cameros Basin, Spain, exhibit $\delta^{34}S$ values between 13‰ to 16‰ (Alonso-Azcárate *et al.*, 2006), similar to those obtained from the Lorraine Basin, France (Fanlo and Ayora, 1998) and northern Spain (Utrilla *et al.*, 1992).

3. The Carbon Cycle

The element carbon (C) has two stable isotopes: ^{12}C and ^{13}C, with natural abundances of 98.9% and 1.1% respectively. It is expressed as $\delta^{13}C$ in per mil (‰), relative to the international standard of Vienna PeeDee Belemnite (VPDB) using the following equation:

$$\delta^{13}C = [((^{13}C/^{12}C)_{sample} - (^{13}C/^{12}C)_{standard}) / (^{13}C/^{12}C)_{standard}] \times 1000 \text{ VPDB}$$

Carbon is stored on Earth in either its reduced organic form ($\delta^{13}C_{org}$, kerogen in sedimentary rocks) or oxidised inorganic form ($\delta^{13}C_{carb}$, carbonate and limestone formations) (Jarvis *et al.*, 2011). The residence time of carbon is up to 10 kyrs in the ocean–atmosphere system, which is much shorter than sulphur isotopes and therefore can be used to a greater time resolution to correlate stratigraphic sections (see Jarvis *et al.*, 2015). The global carbon cycle takes place between different surficial reservoirs (e.g., atmosphere, ocean and terrestrial, Figure 6). Under these surficial reservoirs, carbon can be stored as terrestrial biomass, atmospheric carbon dioxide (CO_2), marine organic matter, dissolved inorganic carbon (DIC) and in the form of methane (CH_4) in the deep marine reservoirs. Over 90% of bio-active carbon is stored in the deep ocean reservoir as bicarbonate (HCO_3^-) (Saltzman and Thomas, 2012). Additionally, carbon is sequestered (e.g., sink of CO_2) during sediment deposition and is released back to the surface during tectonic uplift and weathering processes. Weathering of exposed sedimentary carbon can release it back into the ocean–atmosphere system, thus acting as a source of CO_2 (e.g., Newton and Bottrell, 2007).

Carbon isotope composition of the ocean can be recorded through organic and inorganic sedimentary rocks (Berner, 1990). The marine $\delta^{13}C$ record has been reconstructed since the 1950's (see review by Gröcke 2020 and references therein). Global variations in marine $\delta^{13}C$ ratios reflect changes in the balance of the Earth's marine carbon fluxes, in particular to the amount of carbon between organic and inorganic (Saltzman and Thomas, 2012). Due to the process of photosynthesis, carbon isotope values of photosynthetic organisms are ^{13}C-depleted (^{12}C-enriched) (Newton and Bottrell, 2007) compared to inorganic synthesis. Marine $\delta^{13}C$ is ultimately linked to CO_2 in the atmosphere and through marine circulation processes between the shallow and deep-water column (Saltzman and Thomas, 2012). The uptake rate of ^{13}C-depleted carbon in the shallow and deep ocean can also be affected by ocean stratification and its associated decoupling of the shallow and deep ocean $\delta^{13}C$, as well as variations in bio-productivity rate with changing depth (Magaritz *et al.*, 1992; Horacek *et al.*, 2007). The global carbon isotope cycle can be affected by variations in burial rate and erosion/oxidation rate. More specifically, the burial rate of organic carbon can be affected by sea-level fluctuations, oceanic thermohaline circulation, oceanic anoxia, and terrestrial and marine productivity (Baud *et al.*, 1989).

Figure 6. Schematic diagram of present-day carbon reservoirs (pre-industrial) and carbon isotope composition. DIC = dissolved inorganic carbon. Modified from Newton and Bottrell (2007) and Saltzman and Thomas (2012).

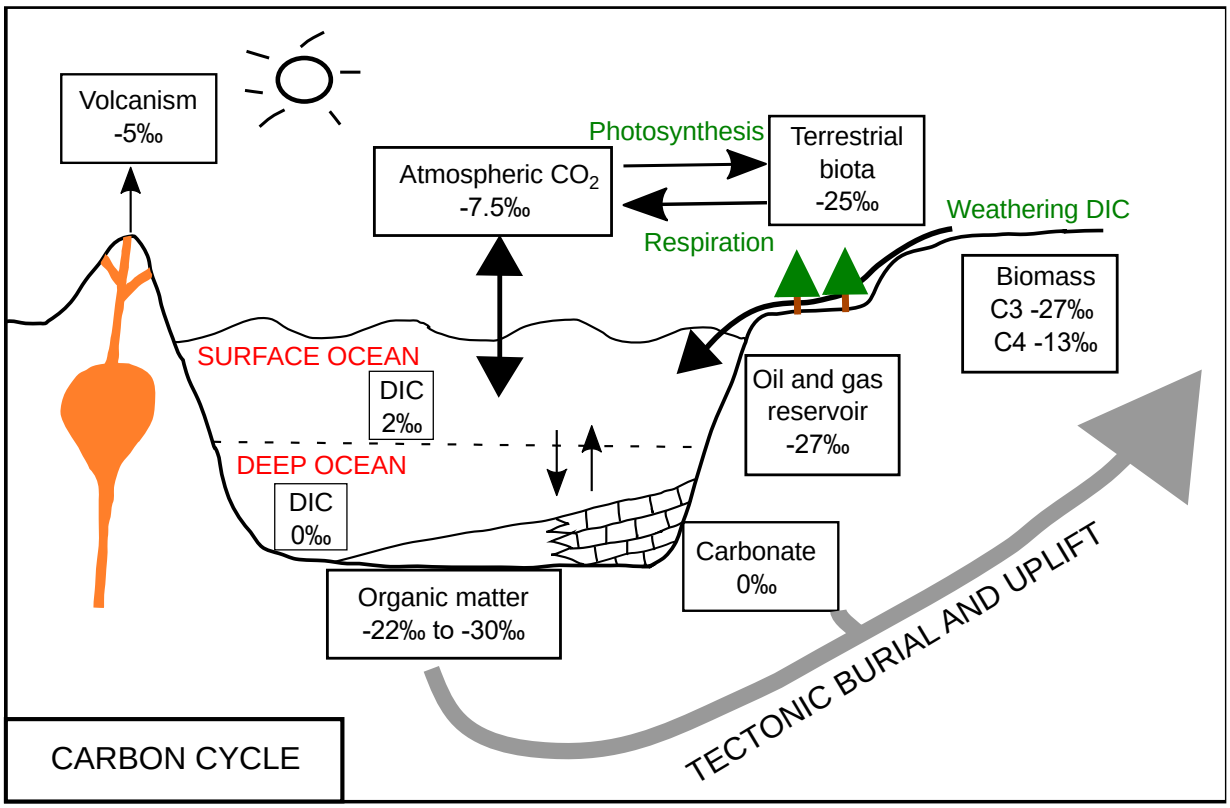

3.1 The Carbon Isotope Curve

The marine $\delta^{13}C$ record of the late Permian to Late Triassic period (see Figure 7) has been studied by many authors (e.g., Korte *et al.*, 2004; Payne *et al.*, 2004; Galfetti *et al.*, 2007; Horacek *et al.*, 2007; Richoz *et al.*, 2007; Algeo *et al.*, 2008; Horacek *et al.*, 2010; Luo *et al.*, 2010; Meyer *et al.*, 2013; Sanson-Barrera *et al.*, 2013; Song *et al.*, 2014; Caravaca *et al.*, 2017; Stebbins *et al.*, 2019; Hu *et al.*, 2020). Most of these studies have focused on the detail of the PTB excursion, and the high-magnitude changes in the Early Triassic.

The typical late Permian $\delta^{13}C_{carb}$ values range from 3‰ to 5‰, with $\delta^{13}C_{org}$ values between –26.5‰ to –24‰ (Korte *et al.*, 2004; Payne *et al.*, 2004), followed by a negative shift at the PTB on the order of 2‰ to 4‰ (Corsetti *et al.*, 2005). The carbonate $\delta^{13}C$

record from southern China displays a decline from 3.7‰ to –0.3‰ at the PTB (Payne *et al.*, 2004). Organic $\delta^{13}C$ values with a large spread in values between –23‰ and –28‰ across the PTB are recorded from Iran (Korte *et al.*, 2004). The negative $\delta^{13}C$ excursion across the PTB (also known as the Lower Griesbachian negative carbon isotope excursion = CIE) has been recognised globally, for example in Iran (Korte *et al.*, 2004), southern China (Payne *et al.*, 2004; Luo *et al.*, 2010), the Southern Alps (Horacek *et al.*, 2007), Vietnam (Algeo *et al.*, 2008), Northern Italy (Horacek *et al.*, 2010) and east Greenland (Sanson-Barrera *et al.*, 2013).

Figure 7. Composite $\delta^{13}C_{carb}$ curve for the Triassic (Cramer and Jarvis, 2020).

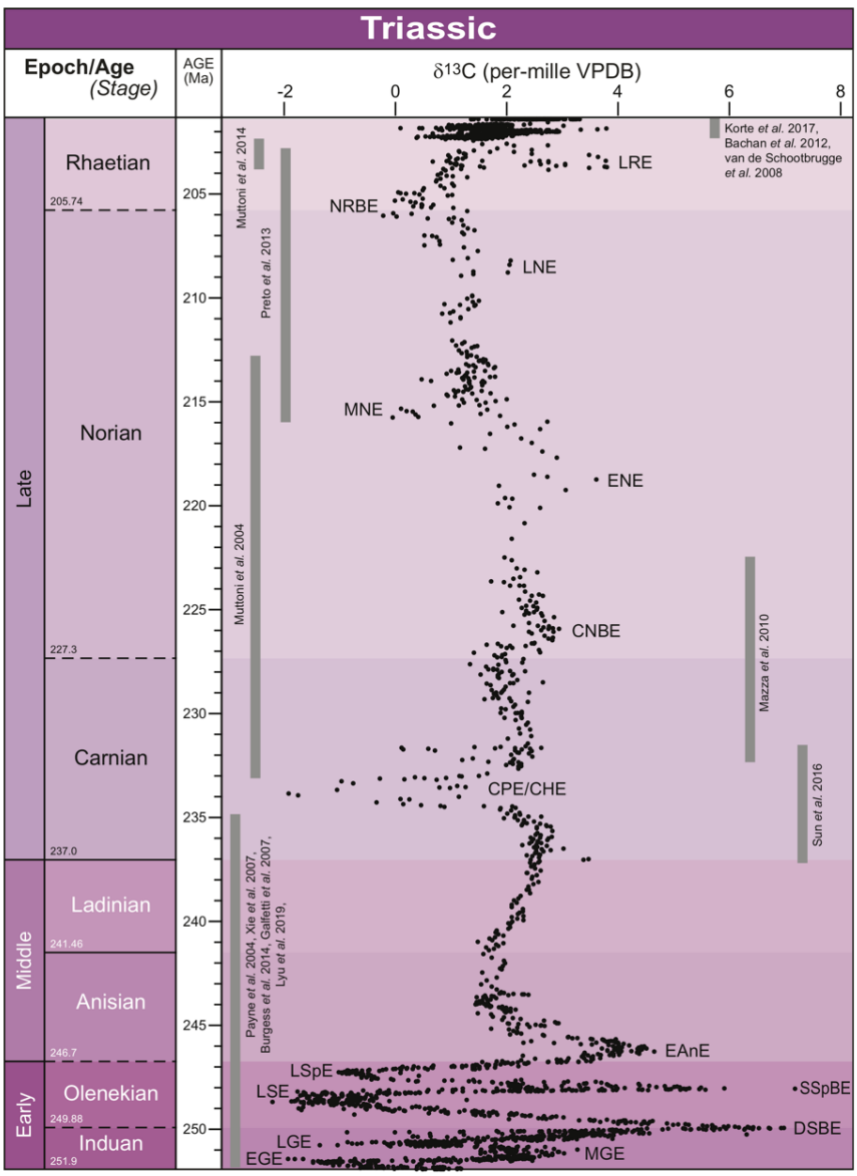

The Early Triassic $\delta^{13}C$ record has been studied extensively (Horacek *et al*., 2007; Meyer *et al*., 2013; Sanson-Barrera *et al*., 2013; Song *et al*., 2014; Caravaca *et al*., 2017; Stebbins *et al*., 2019) due to the occurrence of a series of positive and negative CIEs between 6‰ to 10‰ (Figure 7). Many negative CIEs have been recorded globally at the Griesbachian–Dienerian boundary, Smithian–Spathian boundary and, latest Spathian. Positive CIEs have been recorded globally at the Induan–Olenekian boundary (Richoz *et al*., 2007), Smithian–Spathian boundary and, the base of Anisian (see Figure 7). These $\delta^{13}C$ records are consistent with those obtained in the Southern Alps, Italy (Horacek *et al*., 2007), southern China (Meyer *et al*., 2013; Song *et al*., 2014), northeast Greenland (Sanson-Barrera *et al*., 2013), Western United States (Caravaca *et al*., 2017) and Spiti Valley in India (Stebbins *et al*., 2019).

The cause behind these CIEs is still under debate. Many different explanations have been put forward such as:

(1) Alternation between oxic and anoxic conditions in the oceanic system, which resulted in the fluctuations in the burial rates of organic carbon relative to carbonate.
(2) Environmental disturbances, recoveries and extinctions which caused an imbalance in the carbon cycle. Global diversity began to rise in the Early Triassic and the positive CIEs may be associated with biotic recovery in both the marine and terrestrial ecosystems (Hochuli *et al*., 2016; Brayard *et al*., 2017).

More specifically, negative CIEs can be directly linked to hyper-warming intervals, associated with stagnation of global ocean circulation, limited biodiversity recovery, and a decrease in primary productivity followed by a reduced in BSR processes and burial

rate of organic matter and pyrite (Zhang *et al*., 2018; Stebbins *et al*., 2019). On the other hand, positive CIEs have been linked to oceanic overturning of deep water, resulting in an increase in primary productivity with a concomitant increase in organic carbon burial (Caravaca *et al*., 2017). The positive CIE at the Smithian–Spathian boundary (SSB) has been proposed to be the result of the Siberian large igneous province eruption putting an excessive amount of atmospheric CO_2 into the ocean, leading to high productivity and burial of organic carbon (Galfetti *et al*., 2007). The subsequent drawdown of CO_2 would have stimulated and enhanced polar cooling (Knoll *et al*., 1996; Galfetti *et al*., 2007).

The $\delta^{13}C$ record in the Middle and Late Triassic is relatively stable compared to the Early Triassic record. A long-term relatively stable $\delta^{13}C$ record continued into the Late Triassic, until the short period before the Triassic–Jurassic boundary which show several negative and positive CIEs in the Queen Charlotte Islands, Canada (Williford *et al*., 2009), the Northern Calcareous Alps (Austria) (Felber *et al*., 2015) and the Eastern Tethys (Northern Tibet) (Hu *et al*., 2020).

4. Geological Setting

During the late Permian, Britain was located at a low latitude (15–20°N) in the interior of Laurasia of northern Pangaea (Figure 8), resulting in a hot and dry climate (Tollmann and Kristan-Tollmann, 1985; Howard *et al*., 2008). When Pangaea was starting to break apart 200 million years ago (Figure 8), rocks formed at that time were a combination of the Pangaea and the Variscan mountains that collided during the Late Carboniferous (Howard *et al*., 2008, Smith, 1989; Warrington and Ivimey-Cook, 1992; Chadwick and Evans, 1995).

The Central European Basin (CEB), also known as the Southern Permian Basin, Germanic Basin or the Northwest European Basin is an ancient giant evaporite basin (Ziegler, 1990; Beutler and Szulc, 1999; Doornenbal and Stevenson, 2010). The CEB extends from west England to the Southern North Sea, Northern Germany (Legler *et al*., 2005), Eastern Poland and from the North-South Scandinavian Plateau to the Brabant Massifs, Armorican Massifs and the Vindelician-Bohemian Massifs (Scholze *et al*., 2017). The CEB is estimated to have a length of 2,500 km with a width of 600 km (Legler *et al*., 2005; Scholze *et al*., 2017), and is filled with approximately 2 km of siliciclastic, carbonate and evaporite sedimentary sequences from the Zechstein Group (Ziegler, 1990).

Figure 8. Palaeocoastline and continental margin reconstructions of Pangaea during the late Permian to Late Triassic. The present-day coastlines are shown in black lines (Kocsis and Scotese, 2020)

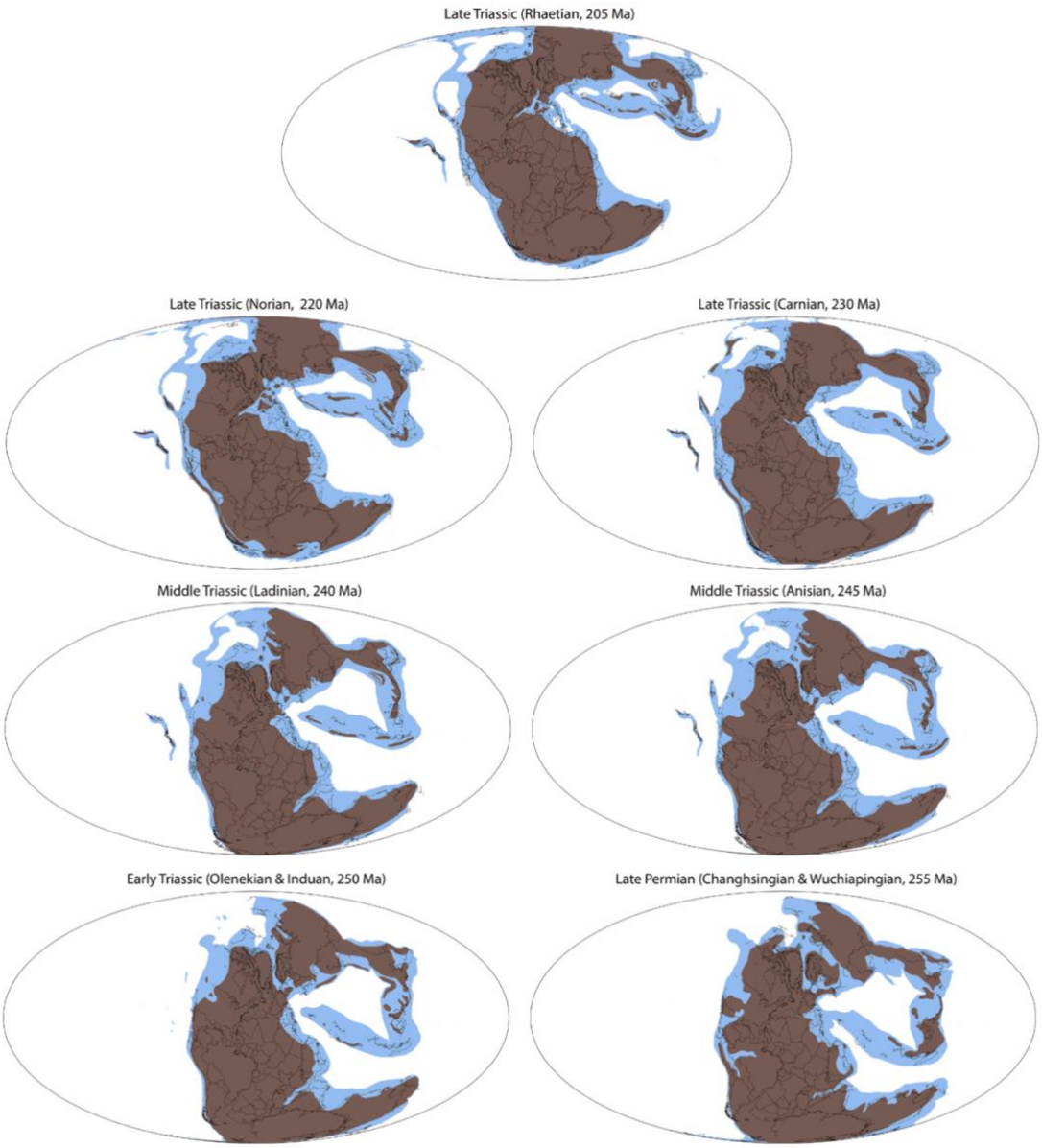

Figure 9. Location map showing Triassic basin-infilled deposits and late Permian Zechstein Basin and Bakevellia Sea. The orange star represents the location of the Staithes S-20 borehole, North East England (modified from McKie and Williams, 2009).

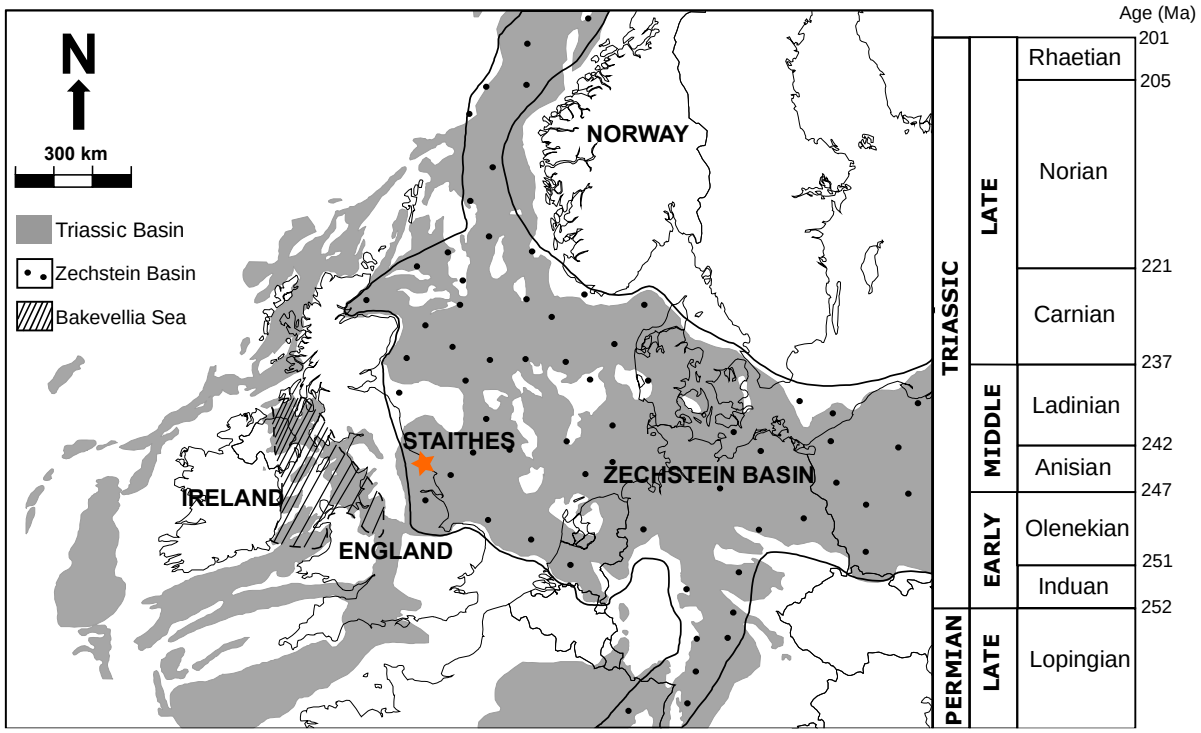

Towards the end of the Permian, the marine sea-level transgression emerged and transformed the Zechstein Basin be fully marine (Smith, 1989; Scholze *et al.*, 2017). Major evaporation has resulted in the formation of thick evaporite successions, the late Permian Zechstein Evaporites (Kent, 1967; Warrington and Ivimey-Cook, 1992). Palaeogeographic reconstruction indicates that the Zechstein Sea was connected to the open ocean by a long and narrow channel between Greenland, Norway and eastern UK (Figure 9); extended from the Northern Scotland to the Irish Sea, feeding the Bakevellia Sea (Smith *et al.*, 1974). The dating of the Zechstein transgression is based on lithostratigraphy and sequence stratigraphy of faunas in the North East England, Germany and Poland (Smith *et al.*, 1974). The cause of this transgression is suggested to be linked to the final melting of the Gondwana ice sheet, resulting in a rapid and synchronous rise in sea level (Benton *et al.*, 2002).

4.1 Lithostratigraphic Sequences

In Europe, the late Permian stratigraphic sequence is dominated by the Zechstein Group, which consisted of seven evaporative cycles (Z1–Z7) (Howard *et al*., 2008). The overlying Triassic sequences are subdivided into three major lithostratigraphic units in Germany: Buntsandstein, Muschelkalk and Keuper (Figure 10).

The stratigraphy in this case study (North East England) does not follow exactly the classic Zechstein succession, although the main elements of thesis facies do occur (Smith *et al*., 1974). In Britain, the latest Permian successions are composed of the upper Permian evaporites (Figure 10) which consisted of the Magnesian Limestone and the Permian Upper Marls (Ruffell and Shelton, 1999). The overlying Triassic sequences are commonly divided into three major lithostratigraphic units: the Sherwood Sandstone Group (Lopingian/Induan to early Anisian), Mercia Mudstone Group (Anisian to early Rhaetian), and the Penarth Group (Rhaetian) (Figure 10) (Warrington, 2005; Warrington, 1980; Warrington and Ivimey-Cook, 1992; Howard *et al*., 2008). The terms ‘Bunter’, ‘Keuper’ and ‘Rhaetic’ were applied to the British Triassic sequences, based on the lithological similarity with the Germanic successions. These terms were abandoned by the Triassic Working Group due to their implied time connotation. The former ‘Bunter’ and ‘Lower Keuper Sandstone’ units were combined to form the Sherwood Sandstone Group. The former ‘Keuper’ and ‘Rhaetic’ was corresponded to the overlying Mercia Mudstone Group and the Penarth Group (Howard *et al*., 2008).

The Triassic sequences of Britain have been studied extensively and described by Woods (1973), Warrington *et al*. (1980), Smith *et al*. (1986), Warrington and Ivimey-Cook

(1992), Benton *et al*. (2002), Howard *et al*. (2008); Ambrose *et al*. (2014) and Smith *et al*. (2014).

Figure 10. Lithostratigraphic correlation between the Germanic and English late Permian to Late Triassic sequences (Scholze et al., 2017; Szurlies, 2007; Szurlies et al., 2012; Warrington et al., 1980).

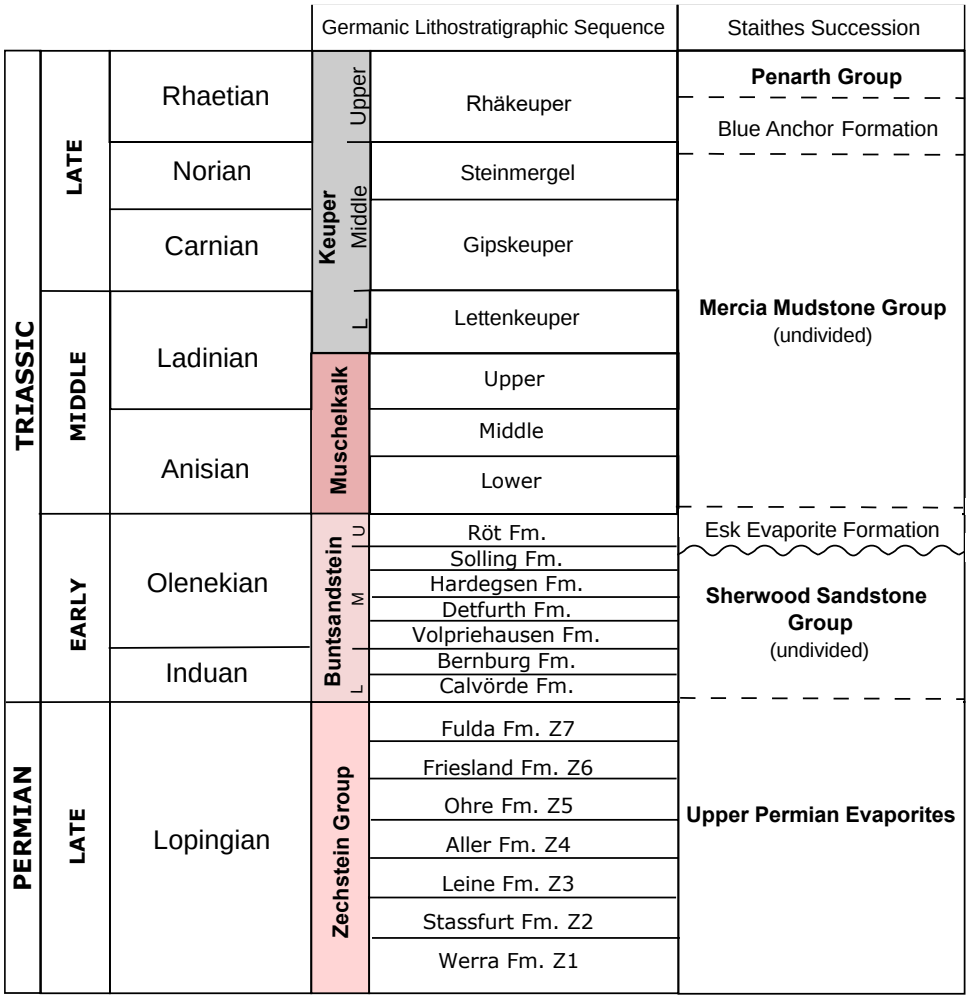

4.2 Sedimentary Deposition and Palaeoclimate

The overall Permian deposition environment has been inferred as arid until the late Permian Zechstein marine transgression occurred. Sedimentation in the late Permian was formed in an epicontinental marine, under an arid to semi-arid condition, governed by

multiple evaporitic cycles of marine ingressions from the Arctic Sea, which resulted in the development of seven evaporitic cycles (Z1–Z7) of the Zechstein Group (Legler *et al*., 2005; Legler and Schneider, 2008; Scholze *et al*., 2016). The siliciclastic-calcareous-evaporitic drying upward sequences are well-correlated across the CEB (Strohmenger and Strauss, 1996; Strohmenger *et al*., 1996; Legler *et al*., 2005). The Zechstein Group has covered the northwest and central Europe (Figure 9) and was replaced by the succeeding Triassic red sandstone deposits (450 Ma). The late Permian deposits are composed of dolomitic limestones (a.k.a. the Magnesian Limestone), calcareous shales (Benton *et al*., 2002) and the overlying saliferous mudstones and evaporites (upper Permian evaporites), with some marine shell fossils and are interbedded with minor land-derived clastic deposits (Ruffell and Shelton, 1999).

The overall deposition of the Early to Middle Triassic sequences were supplied by fluvial systems sourced from monsoonal rains falling on the Variscan mountains during highly erratic pluvial episodes (McKie, 2017), which fed a major river system that flowed into British fault-bounded basins (Howard *et al*., 2008). Runoff from the Variscan mountains significantly decreased by the late Anisian, although the climate became more stable by the Norian (McKie, 2017).

The Early Triassic sediments are composed of the Sherwood Sandstone Group, which spans for approximately 5 million years (from the latest Permian to end of Olenekian) based on microflora evidence in Kingscourt, Ireland (Warrington and Ivimey-Cook, 1992). The top of the Sherwood Sandstone Group is suggested to be associated with the top of the Germanic Hardegsen Formation (Middle Buntsandstein), also known as the ‘Hardegsen Disconformity’. The widespread Hardegsen Disconformity is of late Scythian age (Evans *et al*., 1993) and a result from regional uplift followed by erosion, which

affected much of Northwestern Europe during the deposition of the Germanic Buntsandstein sequences (Trusheim, 1963; Filomena and Stollhofen, 2011).

In Britain, the Middle Triassic sediments are composed of the uppermost part of the Sherwood Sandstone Group and the overlying Mercia Mudstone Group (Warrington and Ivimey-Cook, 1992). In general, the Mercia Mudstone Group comprised of a mixture of basinal, argillaceous, evaporite-dominant deposits (Warrington and Ivimey-Cook, 1992; Howard *et al*., 2008). The laterally coarse-grained clastic sequences also indicate both marine and non-marine sources (Howard *et al*., 2008). Additionally, the halite beds of the Mercia Mudstone Group are more widespread in the southern part of the North Sea and further west in Britain and are dated palynologically as early Anisian to early Carnian (Warrington and Ivimey-Cook, 1992).

The Late Triassic British sediments are composed of the remaining part of the Mercia Mudstone Group, with mostly sulphate evaporites and almost no halites. Blue Anchor Formation, forming the uppermost formation of the group, is characterised with a grey to green-grey colour, and it is widely recorded in England (Howard *et al*., 2008). The top of the Blue Anchor Formation often presents as an unconformable boundary with the succeeding Westbury Formation (Penarth Group) in the Rhaetian (Howard *et al*., 2008).

During the early Rhaetian, deposition of the Mercia Mudstone Group ceased when a marine transgression flooded the saline mudflats (sabkhas) and deposited the widespread, dark grey to black muddy mudstone of the Penarth Group (Warrington and Ivimey-Cook, 1992, Howard *et al*., 2008). The Penarth Group is composed of argillaceous, calcareous and richly fossiliferous mudstones with little to no evaporites and is suggested to have formed during the Rhaetian transgression (Warrington *et al*., 1980). The Rhaetian

sedimentation have suffered from widespread erosion along with the Jurassic and therefore, is not always present in borings (Kent, 1967). Besides, there is no additional indication of other sedimentary units of the Rhaetian known in England (Kent, 1967).

The overall deposition of Permian and Triassic sediments is controlled by the interplay of sea-level change, extension-driven basinal subsidence and climatic fluctuations (Ruffell and Shelton, 1999). Throughout the Triassic, tensional crustal stresses occurred at continental rifts where the North Atlantic Ocean started opening and led to widespread growth of significant faults and rift development (Whittaker, 1985; Ziegler, 1987), which also has an effect on the distribution and character of the sedimentary sequences (Warrington and Ivimey-Cook, 1992).

5. Study Area

5.1 Background of the study area

In this study, 389 late Permian to Late Triassic core samples were taken between the depths of 1,236 ft to 3,472 ft (376.9 m to 1,058.44 m) from the Staithes S-20 borehole, Boulby Mine, Cleveland Basin, northeast Yorkshire, UK (grid reference: NZ476034E/518000N) (Woods, 1973). The borehole was drilled in 1968 by Cleveland Potash, Ltd. To follow up on the discovery of potassium salts in Yorkshire in 1939 (Woods, 1973). The Cleveland Basin is a relatively small extensional sedimentary basin, located in north-eastern part of England (Figure 11), separated from the East Midlands Shelf, in the north-western European seaway.

5.2 Lithology and Sedimentology

Figure 12 shows the stratigraphic column of the Staithes-20 borehole investigated in this study. The English late Permian is characterised by the upper Permian evaporites, followed by the Triassic sequences: Sherwood Sandstone Group, Mercia Mudstone Group and Penarth Group, which marks the end of the Triassic. The lithology and sedimentology of the late Permian and Triassic sequences are described as below.

The bottom of the Staithes core is composed of thick-bedded halites (Appendix Figure 1), micro- and macroscale gypsum nodules (Appendix Figure 2 and 3), with occasional green reduction spots (Appendix Figure 4) in a fine-medium grained, argillaceous red-brown mudstone. The upper Permian Evaporite interval is suggested to be equivalent to the Z7 sequence of the Zechstein cycles (Bourquin *et al*., 2011), which formed in an arid

climate probably in an epeiric marine setting (Benton *et al*., 2002). The presence of green reduction spots in the upper Permian evaporites indicates a reduced, anoxic environment during burial which would otherwise be oxidised at that time of depositional (Spinks *et al*., 2010). The top of the upper Permian Evaporite is defined at a depth of 3,130 ft (954 m) (Figure 12), based on the transition from the argillaceous evaporitic-dominated mudstone to the arenaceous siltstone. It is important to note that the boundary identified in this core is based on lithology and not biostratigraphy due to the lack of biostratigraphic useful fossils.

Figure 11. (Top) Permian and Mesozoic basins of England and Wales (Stone, 2015). (Bottom left) Map of Britain and Cleveland Basin (bottom right) showing the location of Staithes, Yorkshire, England (Caswell and Dawn, 2019).

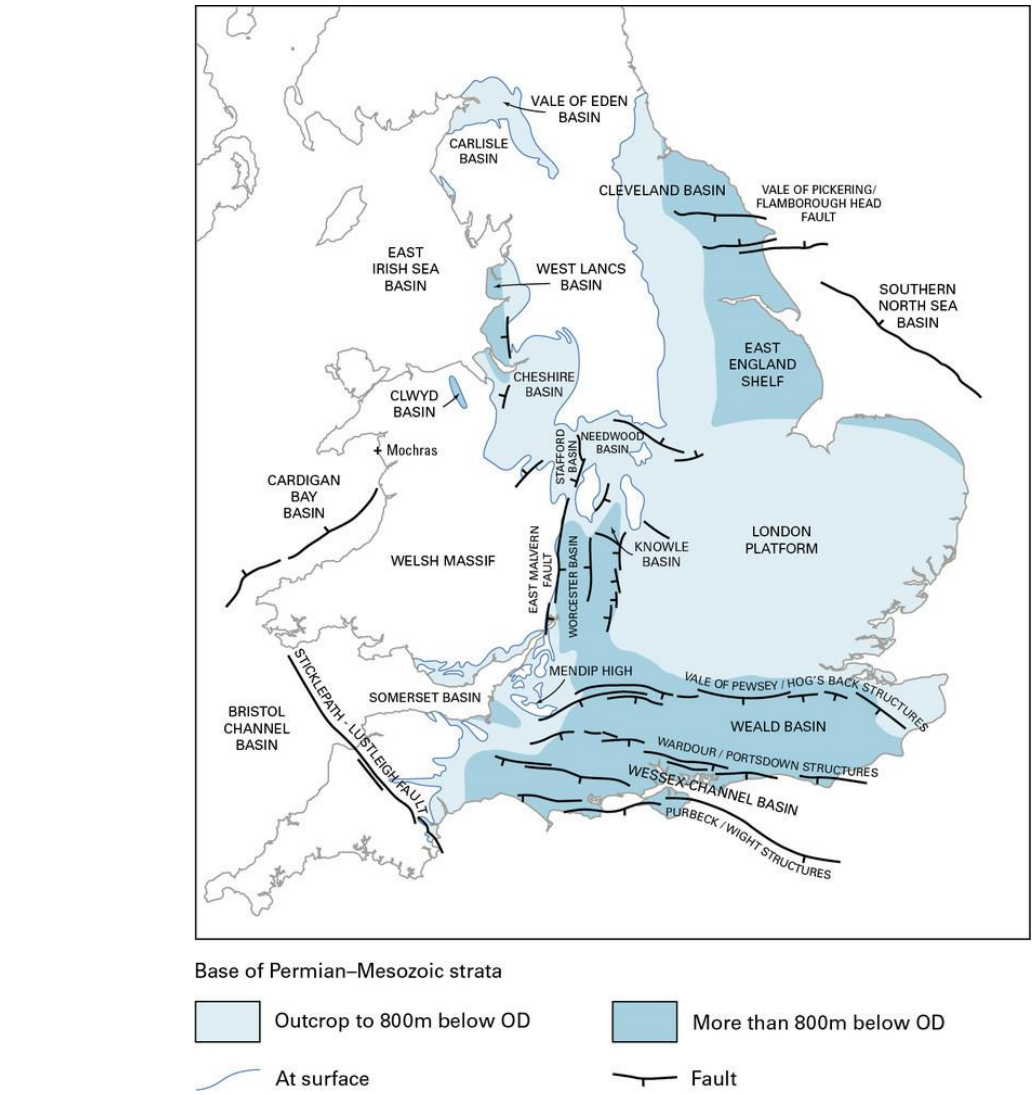

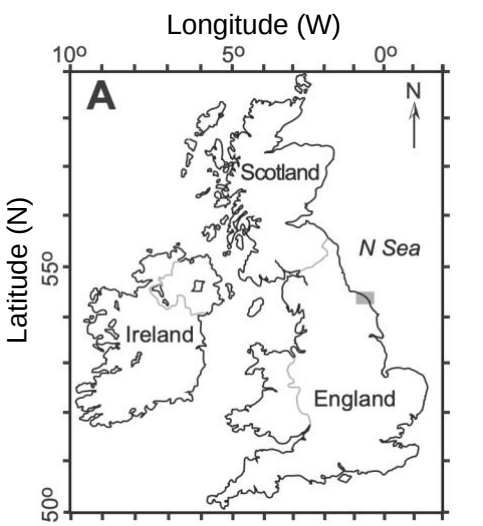

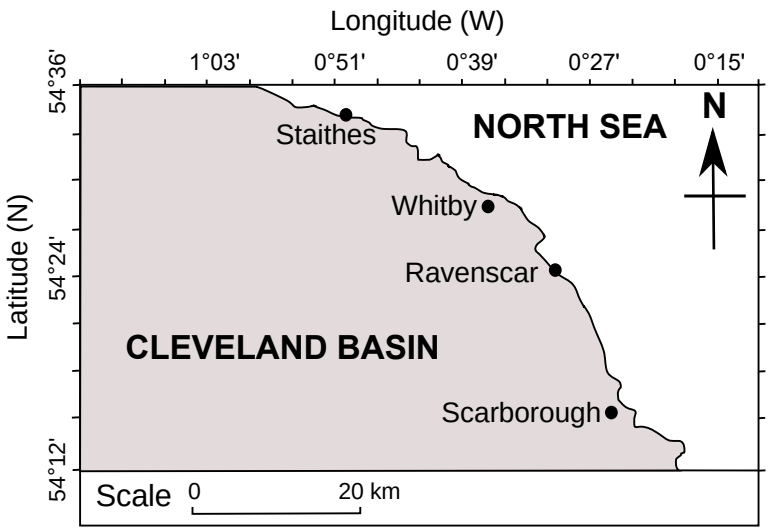

Figure 12. Stratigraphic column of the Staithes-20 borehole (modified after Woods, 1973; including own observations). Formation boundaries are based on lithostratigraphy.

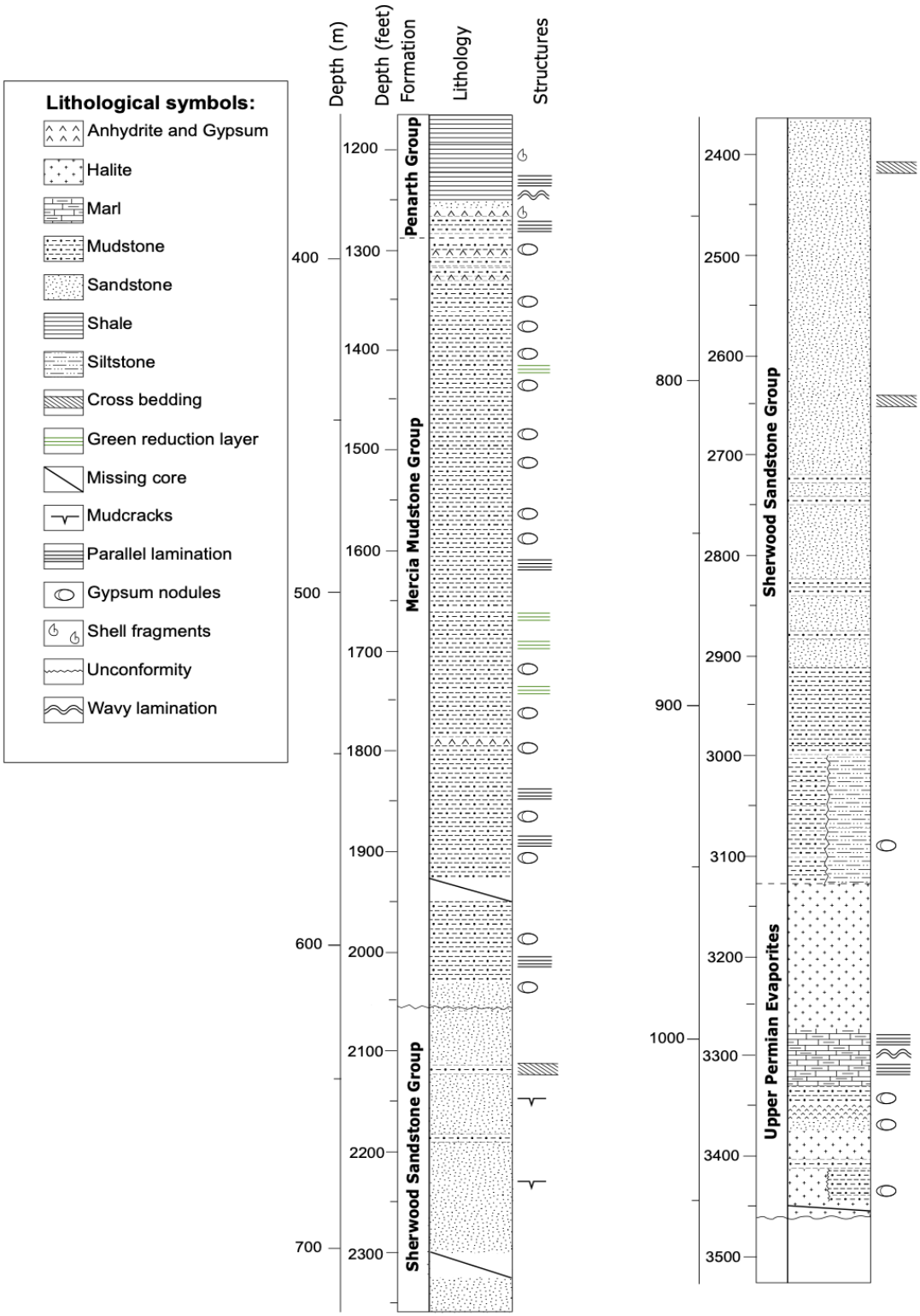

The Sherwood Sandstone Group is previously assigned to the 'Bunter sandstone' (Manning *et al.*, 1970) or the 'Lower Keuper Sandstone' or 'Bunter Marls' (Fowler & Robbie, 1961), and spans the Lopingian/earliest Induan to Anisian, based on palynology evidence in the Kingscourt Outlier, Ireland (Gardiner and Visscher, 1971; Visscher, 1971). The Sherwood Sandstone Group in the Staithes core is composed of dark red to brown massive, medium to coarse-grained sandstones. They are poorly cemented, arenaceous, unfossiliferous and contain many sedimentary structures, such as cross-lamination (Appendix Figure 5) and occasional ripple marks. Unfortunately, age-diagnostic fossils within this succession are rare, hence resulted in difficulties associated with the chrono-stratigraphic subdivision and correlation of the group (Jeans, 2006).

The Sherwood Sandstone Group is suggested to have formed in a semi-arid and warm climate as evidenced by the bisaccate pollen from the latest Permian in the northwest Europe (Kürschner and Herngreen, 2010), dominated by aeolian and fluvial sandstones. The depositional environment has also been suggested to be influenced by a strong monsoonal circulation pattern based on climatic models (Kutzbach and Gallimore, 1989; Parrish, 1993; Selwood and Valdes, 2007). The lower part of the Sherwood Sandstone Group was largely restricted by fault-bounded basins; the upper part of the group was formed in a terrestrial-marine environment, possibly in a shallow hypersaline water body with constant replenishment of seawater (Warrington and Ivimey-Cook, 1992). During the marine transgression in the early Anisian, the upper part of the Sherwood Sandstone Group retreated southwards and was replaced by the subaqueous hypersaline and evaporitic-mudflat environment of the Mercia Mudstone Group (Warrington and Ivimey-Cook, 1992). The boundary between the Sherwood Sandstone Group and the Mercia Mudstone Group in the Staithes core at a depth of 2,088 ft (636 m), as defined by the transition from sandstone-dominated facies to mudstone-siltstone-dominated facies.

Palynology evidence at ~2,088 ft (636 m) is confirmed as of early Anisian age by G. Warrington (personal communication, 2019).

The Mercia Mudstone Group represents the early Anisian to earliest Rhaetian of the Triassic. The Mercia Mudstone Group in the Staithes-20 core is generally undivided with the overall composition consisted of red argillaceous, subordinate silt-mudstone, with anhydrite and gypsum nodules commonly occurred throughout the interval. Thin beds of anhydrite, gypsum and desiccation cracks are developed at particular horizons throughout the thin interbedded sandstones (Howard *et al*., 2008).

Warrington *et al*. (1980) proposed that the Esk Evaporite Formation forms the lowermost part of the Mercia Mudstone Group at the East Midlands Shelf (North) at a depth of approximately 2,037 ft to 2,060 ft (621 m to 628 m), spanning the latest Olenekian to earliest Anisian. The Esk Evaporite Formation is also known as the 'Röt halite' and 'Keuper halite', which is composed of interbedded mudstone–halite with collapsed structures (Warrington *et al*., 1980). This formation can be observed in the Staithes core and hence can be assigned as the Esk Evaporite Formation. However, the top boundary of this formation is unclear.

The rest of the Mercia Mudstone Group is generally undivided. The uppermost part of the Mercia Mudstone Group is composed of the Blue Anchor Formation, which can be commonly observed in sedimentary sections across England, including at St Audrie's Bay (west Somerset coast), south Glamorgan (Warrington and Ivimey-Cook, 1995) and South Devon coast (Gallois, 2001). It is composed of fine-grained, dominated dark grey to light grey and grey-green coloured muddy mudstones with little evidence of bioturbation (Warrington *et al*., 1980; Howard *et al*., 2008). This formation can be observed in the

Staithes core; however, the exact boundary cannot be placed due to the very similar lithologies appeared throughout the Mercia Mudstone Group.

In the Staithes-20 core (Figure 12), the boundary between the Mercia Mudstone Group and the above Westbury Formation of the Penarth Group is defined at depth 1,280 ft (390 m), marked by the transition from the grey-green mudstone (Blue Anchor Formation) to the dark grey to black fossiliferous mudstone (Westbury Formation).

The deposition environment of the Mercia Mudstone Group is proposed to be playas, inland sabkhas or shallow-water bodies of hypersaline brine, with minor wind-blown dust and a marine-terrestrial origin and a constant replenishment source from the Tethys Ocean (Porter, 2003), based on trace-fossil records from North Cheshire (Benton *et al*., 2002). Alternatively, strontium isotope data from the Central European Basin recorded during the Muschelkalk regression (Middle Ladinian) suggests a decrease in salinity, indicating a normal marine to brackish environment, with an occasional influx of freshwater from increased monsoonal activities (Korte *et al*. 2003). This wet period is suggested to have ended in the late Ladinian, by the depositional of evaporitic mudstones and inland sabkha deposits (Aigner and Bachmann, 1989; Simms and Ruffell, 1989, 1990).

The Penarth Group spanned from the early Rhaetian to end of Rhaetian, based on biostratigraphy and palynological evidence (Porter, 2003). The bottom of this group, Westbury Formation, also known as ‘Westbury Beds’ or ‘Black Shales’, is composed of argillaceous, calcareous, brown, dark grey to black coloured (Appendix Figure 6), laminated silty mudstone with minor subordinate fine-grained sandstones, and some bivalve’s shell impressions. Green reduction laminated layers (Appendix Figure 7 and 8), nodules (Appendix Figure 9, 10 and 11), bands of anhydrite (Appendix Figure 12 and

13), halite and mud clasts (Appendix Figure 14) are occasionally exposed in the fine-grained mudstone. The depositional environment of the Penarth Group is the result of a rapid marine transgression resulting in marine conditions. Therefore, forming the grey-green colour laminated layers by the reducing conditions during the Rhaetic marine transgression (Woods, 1973). The top of the Penarth Group boundary is not identified in the Staithes core as the studying of the core finished at depth of 1,236.83 ft (377 m).

6. Methodology

This study analysed 389 evaporite samples collected from the Staithes-20 borehole between the depths of 1,236.83 ft to 3,472.58 ft (377 m to 1,058 m) for sulphur isotope analysis. All samples consisted of anhydrite/gypsum nodules and veins, and massive halite beds. Core samples were washed and cleaned with a toothbrush using tap water, then dried at room temperature. A selection of samples was chosen for thin-section analysis. The remaining samples were placed into zip-lock bags until further preparation. Each sample was drilled with a Dremel 8200 hand-drill and a Dremel diamond wheel point bit (2 mm). Before drilling each sample, the surface material was removed and discarded. A toothbrush was used to brush off the surface dust from the sample and the drill bit. For each sample, between 50–200 mg of evaporite and sediment was drilled out. The drill bit was cleaned before and between each sample. The drilled powder was transferred into a 1.5 ml microcentrifuge tube.

Sulphur precipitation was performed on halite samples due to the fact that halite has little sulphur. This was done by crashing the halite sample down to chips and transferring it into a 50 ml centrifuge tube to the 5 ml line. 50 ml of 10% NaCl solution (50 grams of NaCl added to 500 ml of double-deionised H_2O) was added and mixed thoroughly. The samples were left in the NaCl solution for at least 24 hrs for the sample to be dissolved. The solution was then centrifuged for 4 minutes at 3,000 rpm and 25 ml of the supernatant was decanted into another 50 ml centrifuge tube for barium sulphate precipitation. 25 ml of BaCl was added into each tube followed by 1 ml of 3N HCl to prevent the formation of barium carbonate. During each batch, a number of samples were tested with pH paper to ensure that the solution was acidic. The sample was then centrifuged for 4 minutes at

3,000 rpm and the supernatant was decanted off. The precipitated $BaSO_4$ was neutralised using double deionised water and centrifuged once more (as above) and decanted off. The precipitated $BaSO_4$ samples were placed in a drying oven set at 55°C and left for at least 24 hrs until dry: the barium sulphate precipitates were then transferred into microcentrifuge tubes for storage.

Bulk organic carbon isotope analysis was also performed on the sediments for each sample. Sediment samples on the order of 200 mg were transferred in to a 15 ml centrifuge. Two ml of 3N HCl was first added to assess the reactivity of the samples: there was usually little to no reaction in all samples. Although carbonate may not have been present a further 10 ml of HCl was added and left overnight in a fume hood at room temperature. The samples were subsequently centrifuged for 4 minutes at 3,000 rpm, and the HCl solution was decanted off and disposed. The samples were then neutralised using double-deionised water and centrifuged for a further 4 minutes at 3,000 rpm: this step was repeated three times. The residual sample was placed in a drying oven at 55°C and left for at least 48 hours until dry.

Carbon isotope analysis of the samples were performed using a Costech Elemental Analyser (ECS 4010) connected to a Thermo Scientific Delta V Advantage isotope ratio mass spectrometer. Carbon isotope ratios are corrected for ^{17}O contribution and reported in standard delta (δ) notation in per mil (‰) relative to Vienna Pee Dee Belemnite (VPDB). Isotopic accuracy was monitored through routine analyses of in-house standards, which were stringently calibrated against international standards (e.g., USGS 24, 40, IAEA 600, IAEA CH3, IAEA CH7): this provided a total linear range in $\delta^{13}C$ between –46‰ and 3‰. Analytical uncertainty in $\delta^{13}C$ was typically ±0.1‰ or better for

replicate analyses of the international standards. Total organic carbon was obtained as part of the isotopic analysis using an internal standard (glutamic acid, 40.82% C).

For sulphur isotope analysis, a series of international standards, NBS-127 (barium sulphate), IAEA-S-1 (silver sulphide), IAEA-S-2 (silver sulphide), and IAEA-S-3 (silver sulphide) were analysed each day. In addition, a suite of internal standards (silver sulphide and sulphanilamide) is analysed throughout the analytical day. The anhydrite/gypsum evaporite and $BaSO_4$ powders were weighed into tin capsules with a range between 0.4–0.6 mg: 1–3 mg of tungsten (VI) oxide (WO_3) was added to each tin capsule to aid in the combustion process. All surfaces were cleaned between weighing each sample, and gloves were worn at all times.

Sulphur isotopic analysis of collagen samples were performed using a Costech Elemental Analyser (ECS 4010) connected to a Thermo Scientific Delta V Plus isotope ratio mass spectrometer. Collagen was weighed out into 10x10mm tin capsules (between 4–6 mg) and approximately the same weight of vanadium pentoxide (V_2O_5) was added to aid in the combustion process to release sulphur. Isotopic accuracy was monitored using the following international sulphur standards: IAEA-S-2, IAEA-S-3, IAEA-S-4, IAEA-SO-5, and NBS 127. Analytical uncertainty in sulphur isotope analysis was typically <0.2‰ for replicate analyses of the international standards. Total sulphur was obtained as part of the isotopic analysis using the international standards listed above.

7. Results

Figure 13 shows the evaporite $\delta^{34}S$ and organic matter $\delta^{13}C$ record obtained from the Staithes-20 borehole, based on the core sample of Staithes-20 borehole. All of this data is reported in Appendix Table 1.

The Upper Permian Evaporite $\delta^{34}S$ data (between 3,473 to 3,130 ft.) exhibit a cyclic nature to the record. The late Permian $\delta^{34}S$ content is characterised with values ranging from 8‰ to 13‰, with an average of 10‰. Three positive anomalies are recorded right after the transition from the Upper Permian Evaporites to the overlying Sherwood Sandstone Group (Figure 13). The Sherwood Sandstone Group (at depth 3,130 to 2,088 ft.) $\delta^{34}S$ values show a gradual increase towards to the early Anisian, with $\delta^{34}S$ values ranging from 11‰ to 17‰ with a mean of 12‰. The Mercia Mudstone Group $\delta^{34}S$ values ranged from 14‰ to 28‰, with a mean of 18‰. The boundary between the Sherwood Sandstone Group and the overlying Mercia Mudstone Group records an abrupt rise to 28‰ at the early Anisian (Warrington, 2019). The $\delta^{34}S$ record of the Mercia Mudstone Group (at depth 2,088 to 1,280 ft.) is characterised by a steady decline towards the top of the core. The $\delta^{34}S$ record then started to increase at a depth 1,365 ft, from 13‰ to 18‰.

The overall $\delta^{13}C_{org}$ record from the late Permian to Late Triassic displayed relatively constant $\delta^{13}C$ values ranging from –22‰ to –30‰, except from those towards the bottom of the core, with high and positive values towards carbonates which will be excluded from this study. The Upper Permian Evaporites $\delta^{13}C$ values are very consistent, ranging from –25‰ to –30‰, with a mean value of –27.6‰. The Sherwood Sandstone Group of Early Triassic $\delta^{13}C$ values ranged from –24‰ to –29‰, followed by a fluctuated $\delta^{13}C$

values between –22‰ and –29‰ at the base of Anisian. The $\delta^{13}C$ record is followed by a decline of ~5‰, with $\delta^{13}C$ values ranging from –30‰ to –28‰ dominating the remaining part of Middle Triassic to pre-Rhaetian. The $\delta^{13}C$ record is specifically interrupted by variations in $\delta^{13}C$ values between –22‰ and –27‰, in prior the beginning of Rhaetian.

Figure 13. Stratigraphic column, with $\delta^{34}S$ and $\delta^{13}C_{org}$ curves of the Staithes-20 borehole. The boundaries of the Upper Permian Evaporites and the Penarth Group is defined by Woods (1973). The Olenekian–Anisian boundary is defined by palynological evidence (Warrington, 2019).

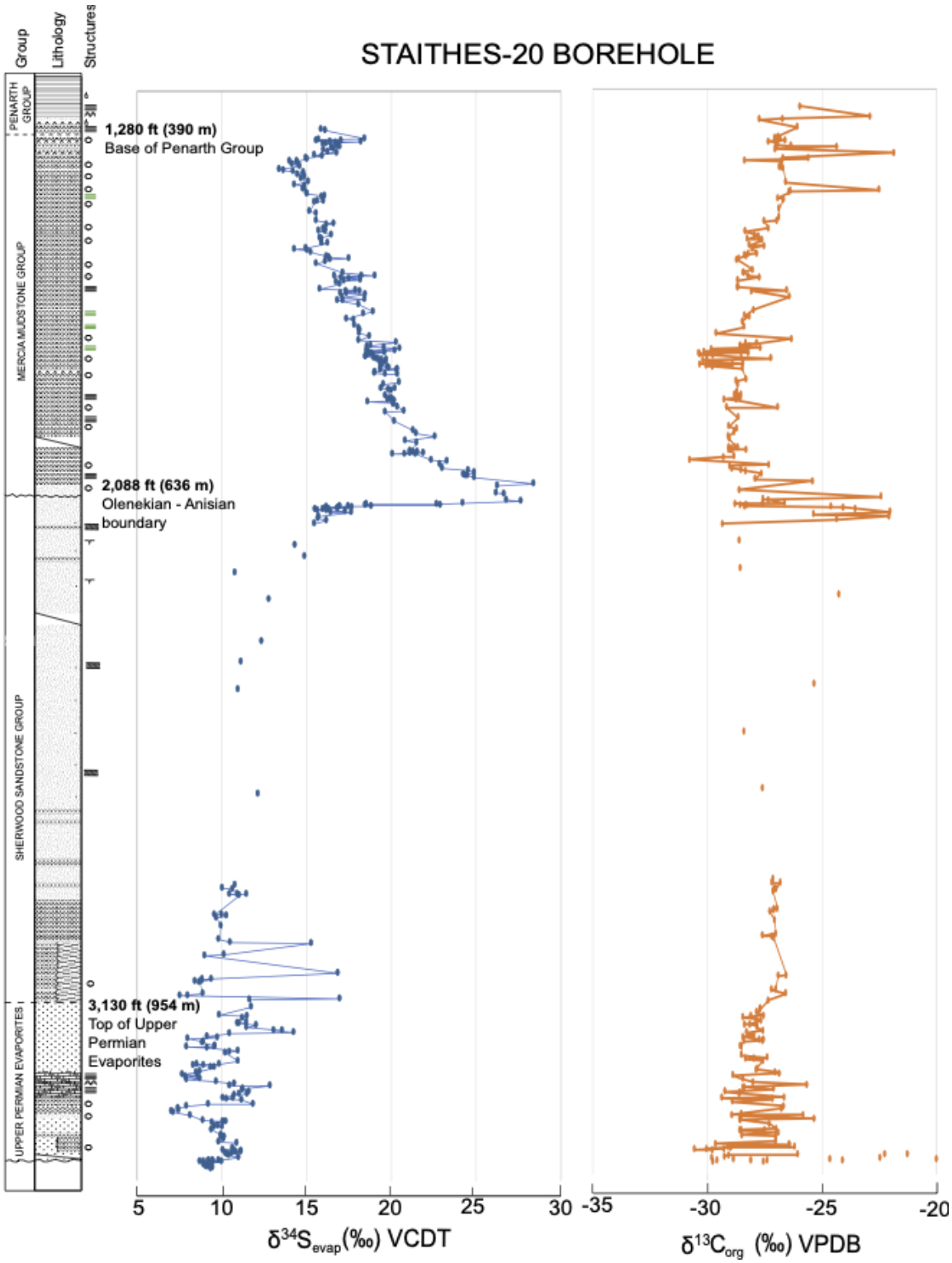

8. Discussion

8.1 Sulphur Isotope Curve

Overall, a total of 124 evaporite sulphate samples have been analysed from the upper Permian evaporites unit. The $\delta^{34}S$ values of 10‰ of late Permian evaporites (Figure 13) from Staithes-20 borehole are in good agreement with the previous $\delta^{34}S$ records ranging from 9‰ to 13‰, obtained from Austria (Spötl and Pak, 1996); Northern Germany (Kampschulte *et al.*, 1998); Abu Dhabi (Worden *et al.*, 1997); Persian Gulf (Insalaco *et al.*, 2006); the Alps (Longinelli and Flora, 2007); western Poland (Peryt *et al.*, 2010) and Northern Switzerland (Bernasconi *et al.*, 2017). The low seawater $\delta^{34}S$ value (~11‰) is very distinctive for the latest Permian (Claypool *et al.*, 1980; Cortecci *et al.*, 1981) and can therefore, be used for correlating purposes with other late Permian evaporites. If one was required to distinguish whether a sedimentary succession is late Permian versus Early Triassic or contains the PTB, sulphur isotope stratigraphy would be able to achieve this.

The late Permian $\delta^{34}S$ record is the lowest throughout the Phanerozoic (Paytan *et al.*, 2011). This low $\delta^{34}S$ content is suggested to result from weathering and oxidation of pyrite, decrease in pyrite burial and/or the deposition of the Zechstein evaporites with an unusually large deposition of sulphates (Hay *et al.*, 2006) in a 'super-anoxic' ocean during the latest Permian (Longinelli and Flora, 2007).

Additionally, the three positive $\delta^{34}S$ anomalies during the latest Permian can be due to a period of build-up of euxinic conditions in the global oceans (Newton *et al.*, 2004; Gorjan *et al.*, 2007), thus deposited the isotopically light sedimentary pyrite, leaving the ocean

enriched in the heavier sulphur isotope. Evidence for late Permian euxinia can be found in Greenland's Ravnefjeld Formation (Nielsen and Shen, 2004), China and the Australian Perth Basin (Grice *et al.*, 2005). Alternatively, since they are only individual $\delta^{34}S$ data points, they could be anomalous and therefore, are excluded from further discussion.

The Sherwood Sandstone Group exhibits $\delta^{34}S$ values that fluctuate between 11‰ to 17‰. The low marine $\delta^{34}S$ record in the earliest Triassic is suggested to still be the result of Zechstein evaporite deposition (Hay *et al.*, 2006) and oceanic anoxia in the latest Permian (Algeo *et al.*, 2011). It is important to note that our Staithes $\delta^{34}S$ curve contrasts with many previous studies of evaporite $\delta^{34}S$ records across the PTB and Early Triassic. This time interval typically shows a rapid increase in $\delta^{34}S$ from 10‰ to 30‰ followed by a gradual decline to 16‰ until the late Induan (Dienerian) (Worden *et al.*, 1997; Newton *et al.*, 2004; Cortecci *et al.*, 1981). Towards the upper part of the Sherwood Sandstone Group, there is a cluster (n = 16) of $\delta^{34}S$ values with a mean of 16.4‰. This part of the $\delta^{34}S$ record can be correlated with those obtained from Northern Italy (Cortecci *et al.*, 1981) and Northern Switzerland (Bernasconi *et al.*, 2017) for the Induan (Dienerian substage) period — thus, earliest Triassic. The highly elevated $\delta^{34}S$ values are missing in the Staithes S-20 record due to a hiatus in the sedimentary succession — this can be seen at ~2,058 ft (see Figure 12 and 13). As a result, it can be confidently stated that the earliest Triassic interval that records the major positive $\delta^{34}S$ event recorded globally is missing in the Staithes S-20 core. Other cores in the region or around the UK may record the event due to the localisation of unconformities in this type of depositional environment. However, the following findings for the Sherwood Sandstone Group can be summarised:

(1) the upper part of the Sherwood Sandstone Group contains the PTB

(2) the majority of the Sherwood Sandstone Group in this part of Yorkshire (at least) is actually Permian, and not Triassic as previously thought.

The $\delta^{34}S$ content in the late Induan may reflect short-lived events of isotopically light sulphur input from either volcanism or re-oxidation of sulphide stored in deeper anoxic oceans (Newton *et al.*, 2004). Alternatively, it may reflect an increase weathering continental rates after PTB extinction event as a consequence of the higher temperatures, resulted in an increase isotopically light sulphate fluxes from river into the ocean (Song *et al.*, 2014). As in warmer periods, the decrease in organic matter fluxes to the seafloor can lead to a decrease in the BSR zone thus limited the sulphate supply to the seafloor (Stebbins *et al.*, 2019).

At the base of the Mercia Mudstone Group (or top of the Sherwood Sandstone Group — depending on the placement of this lithostratigraphic boundary) the $\delta^{34}S$ values increase from 16‰ to a maximum of 28‰. This can be correlated with $\delta^{34}S$ values obtained from Utah (McKee, 1954; Larson, 1966), Germany (Nielsen, 1965), Northern Italy (Cortecci *et al.*, 1981) and Northern Switzerland (Bernasconi *et al.*, 2017). This positive shift in $\delta^{34}S$ record is known as the "Röt Event" (Holser, 1977), as documented in the upper-Lower Triassic Röt Member of the Buntsandstein in Germany (Nielsen and Rickle, 1964; Nielsen, 1965). Fortunately, this is the only part of the Staithes S-20 core that actually has palynological age-constraint — Olenekian–Anisian boundary (Warrington, 2019).

This positive shift in the $\delta^{34}S$ curve is proposed to be rapid (< 1 Myr) and is known as the 'Anisian recovery' that documents a change to a well-ventilated ocean (Isozaki, 1997). Prior to this the global oceans were anoxic — Spathian substage (late Olenekian) (Isozaki,

1997). The major climatic cooling during Spathian might have reinvigorated thermohaline overturning circulation in the global ocean, resulted in enhanced oceanic productivity, bringing nutrients from deep waters into the surface ocean via upwelling (Song *et al.*, 2014). Therefore, sustained marine productivity and an expanded BSR zone leading to increased pyrite burial (causing the residual ocean to become enriched in ^{34}S) (Song *et al.*, 2014).

A total of 215 evaporite samples were analysed from the Mercia Mudstone Group. The age of these deposits is poorly constrained due to a lack of investigation and geospatial variability in the depositional environments of these sediments. However, the Mercia Mudstone Group is generally assigned to an age spanning from the Anisian to the earliest Rhaetian. The $\delta^{34}S$ record of the remaining part of the Anisian to earliest Rhaetian (Figure 13) shows a gradual decrease, following $\delta^{34}S$ values of 25‰ in early Anisian down to 14‰ in the pre-Rhaetian. Despite the early Anisian $\delta^{34}S$ peak, the overall $\delta^{34}S$ values for the Mercia Mudstone Group ranged from 14‰ to 20‰, with a mean value of 17.5‰.

Although this displays a wide range in $\delta^{34}S$, the shape of the curve is not erratic but almost exponential. $\delta^{34}S$ data from the Middle and Late Triassic is sparser than the Early Triassic and Permian, which makes it difficult to correlate the curve globally with any certainty. However, the Staithes S-20 $\delta^{34}S$ values do show close agreement with those obtained from the East Irish Sea Basin, with $\delta^{34}S$ values from 18.6‰ to 21‰ in the Middle Triassic (Thompson and Meadow, 1997), ~18‰ from Northern Switzerland (Bernasconi *et al.*, 2017) and data obtained from Cheshire Basin, UK (Naylor *et al.*, 1989) and Cuba (Meyerhoff and Hatten, 1968; Kirkland and Gerhard, 1971). Hence, the lower part of the Mercia Mudstone Group in the Staithes S-20 core can be constrained to the Middle Triassic.

Towards the top of the Mercia Mudstone Group the lowest $\delta^{34}S$ values of the Mercia Mudstone Group are recorded, ~13.7‰. The $\delta^{34}S$ record is then followed by an increase to 18‰, which is in good agreement with other studies (e.g., Cortecci *et al*., 1981; Rick, 1990; Utrilla *et al*., 1992; Fanlo and Ayora, 1998; Alonso-Azcárate *et al*., 2006; Longinelli and Flora, 2007; Boschetti *et al*., 2011; Bernasconi *et al*., 2017). Thus, the uppermost part of the Mercia Mudstone Group in the Staithes S-20 core can be constrained to the Late Triassic.

The subsequent decline in $\delta^{34}S$ for the Middle to Late Triassic could be caused by either:

(1) a decrease in the burial of sedimentary pyrite;
(2) a change in the oxidation state of the oceans; and/or
(3) a change in the relative flux of magmatic SO_2.

There is very little evidence of decreased pyrite burial in the Middle and Late Triassic, mainly due to a lack of sedimentary sequences investigated or have appropriate depositional environments. This is also the case for the oxidation state of the oceans. Therefore, it would suggest that the change in magmatic flux of sulphur is the cause. Boschetti *et al*. (2011) suggested that the relatively low $\delta^{34}S$ values in the Late Triassic are caused by an input of more magmatic sulphate (0‰ to 3‰). Evidence for increased volcanism during the Middle to Late Triassic is extensive (e.g., Gust *et al*., 1985; Tikhomirov *et al*., 2004). During the Late Triassic oceanic rifting would have increased the amount of SO_2 released into the ocean–atmosphere system, providing substantial amounts of ^{34}S-depleted sulphate to the ocean through oxidation processes.

8.2 Organic Carbon Isotope Curve

The Upper Permian Evaporites (*n* = 124) of the Staithes-20 borehole display a large range in $\delta^{13}C_{org}$ values from –25‰ to –30‰, with a mean value of –27.6‰. Since the organic matter in these environments is possibly related to terrestrial organic matter or bacteria, these values are expected (Gröcke, 2020). At the base of the core the $\delta^{13}C_{org}$ values show a wider range down to –20‰, which is interpreted to be caused by the recycling of older, isotopically heavier, organic matter in the sediment — this is indicative of the erosive surface at the base of the core. $\delta^{13}C_{org}$ values of the latest Permian are certainly within the isotopic range reported here (Korte *et al*., 2004; Payne *et al*., 2004). The late Permian $\delta^{13}C$ values are suggested to be influenced by oceanic anoxia (Kajiwara *et al*., 1994; Isozaki, 1997), a reduction in global organic matter burial rates (Berner, 2005), erosion of coal deposits (enriched in ^{12}C) on land, large-scale volcanism (Siberian Large Igneous Province trap basalts) and the subsequent release of methane hydrates (Retallack, 1999) and hydrogen sulphide (H_2S) (Kump *et al*., 2005).

The $\delta^{13}C_{org}$ record for the lower part of the Sherwood Sandstone Group (*n* = 45) displays $\delta^{13}C_{org}$ values from –22‰ to –28.4‰, with an average of –26.6‰. There are two $\delta^{13}C_{org}$ datapoints of –28.4‰ and –27.6‰, which is similar to those obtained from Iran (Korte *et al*., 2004) and northern China (Payne *et al*., 2004), and may indicate that they are before, or after, the carbon isotope excursion associated with the PTB.

The cause of the negative CIE across the PTB has been linked to the massive collapse of the terrestrial and marine ecosystems. The cause is postulated to be related to large-scale volcanism (Siberian Traps Large Igneous Province) introducing toxic gases and heat that cause a sudden and a massive flux of terrestrial biomass oxidation (source of isotopically

light carbon, ^{12}C) into the ocean–atmosphere system, which triggered the significant biogeochemical changes recorded during this time interval (Dal Corso *et al.*, 2020). Additionally, the increase in carbon oxidation from a major marine regression coupled with a drop in primary productivity (Baud *et al.*, 1989) would have also introduced a large quantity of isotopically light carbon into the Earth system — and a negative $\delta^{13}C$ excursion in all carbon reservoirs (Dal Corso *et al.*, 2020). Furthermore, the upwelling of deep euxinic water would result in organic matter regeneration and isotope fractionation during BSR. The general negative trend across the PTB as recorded in $\delta^{13}C$ is suggested to be driven by a sudden release and overturning of deep, ^{12}C-enriched marine waters (Knoll *et al.*, 1996; Atudorei, 1998). Since deep euxinic water masses tend to be ^{12}C-enriched, upwelling of these waters into shallower water would have produced an environment more conducive also for pyrite formation and burial (Luo *et al.*, 2010) — and the subsequent positive $\delta^{34}S$ excursion in the Early Triassic. However, more sedimentary samples throughout the Staithes S-20 core are required to fully understand the nature of the curve, especially over this interval where the spatial resolution of the samples was limited to where evaporites were found —as discussed previously with the sulphur isotope curve the PTB may in fact be eroded and not present in this core.

At the Sherwood Sandstone Group – Mercia Mudstone Group boundary (at the Olenekian–Anisian boundary) the $\delta^{13}C_{org}$ record of the Staithes-20 borehole displays more ^{13}C-enriched values compared to the earlier record (–24‰ to –22‰, with a mean of –23.2‰). More positive $\delta^{13}C$ values have been previously recorded for this time interval from South China (Payne *et al.*, 2004; Song *et al.*, 2014). The cause of this positive CIE has been interpreted as either:

(1) an overturning ocean bringing deep-water nutrients to the surface ocean leading to an increase in primary productivity and subsequent burial of organic matter in the expanded oxygen minimum zone (Caravaca *et al*., 2017); or

(2) no oceanic changes but a substantial increase in terrestrial and marine biomass production during an Early Triassic recovery event (Horacek *et al*., 2007).

The remaining $\delta^{13}C_{org}$ curve for the Staithes-20 borehole is relatively constant, with values ranging from –25‰ to –30‰, with a mean of –28‰. Three outliers towards the top of the core probably represent sediment samples that have not been completely de-carbonated and/or represent true changes to the carbon cycle — as mentioned previously, more sedimentary samples need to be analysed to assess the true nature of the carbon isotope curve for this core. Having said that the $\delta^{13}C_{org}$ record presented here are in close agreement with those recorded from the Rhaetian of the Queen Charlotte Islands (Canada) (Williford *et al*., 2009) and Northern Tibet (Hu *et al*., 2020). The stabilisation of the $\delta^{13}C$ trend of the Middle to Late Triassic may reflect the cessation of the environmental forcing of carbon cycle perturbations or the recovery of the global ecosystem after the PTB and Early Triassic unstable period (Payne *et al*., 2004).

8.3 C–S Biogeochemical Cycling

The global biogeochemical cycles of sulphur and carbon can be linked through two main processes: (1) continental weathering; and (2) the coupled burial of sedimentary pyrite and organic matter in marine sediments (Gill *et al*., 2007). Pyrite burial is inherently linked with organic carbon and therefore, a proxy for atmospheric oxygen levels and weathering rate (Berner, 2005). Increased nutrient cycling in the surface water enhances

primary productivity and organic matter fluxes to the sediment, with the latter stimulated and maintained in the BSR zone (Stebbins *et al*., 2019). When organic matter is oxidised during BSR, it enhances the BSR rate and thus increasing the burial rate of pyrite (Berner and Raiswell, 1983). However, the relationship between organic matter and pyrite burial varies under euxinic environments, where limitations of sulphate and iron occur (Berner and Raiswell, 1983). Furthermore, continental weathering drives not only sulphate into the ocean, but also carbon through weathering of terrestrial organic matter and carbonate shelves. The subsequent burial of pyrite and organic matter in the oxygen minimum zones (or expanded oxygen minimum zones) show a positive correlation in modern and ancient marine environments (Gill *et al*., 2007).

The decoupling of the $\delta^{13}C$ and $\delta^{34}S$ record can be due to the decreased sensitivity of the marine sulphate reservoir to flux changes. Although the concentration of seawater sulphate in the global ocean is suggested to have increased through the Palaeozoic, however, a lower than modern marine sulphate concentration of 20 mM has been suggested for Permian and Triassic oceans based on marine evaporite fluid inclusion data (Horita *et al*., 2002; Lowenstein *et al*., 2003, 2005; Brennan *et al*., 2004). Furthermore, the emergence of the terrestrial ecosystems during the late-Middle to Late Palaeozoic also plays an important role in the decoupling of $\delta^{13}C$ and $\delta^{34}S$ records (Gill *et al*., 2007).

Variations in the $\delta^{34}S$ composition of seawater sulphate can be used to reflect the balance between evaporite deposition, rate of continental weathering and pyrite burial (Berner and Raiswell, 1983). It is very important to investigate the link between the global carbon and sulphur cycles, and thus provide better constrain on the mechanisms behind isotopic excursions throughout the geological record (Gill *et al*., 2007). Although the $\delta^{34}S$ curve from the Staithes S-20 core does not record the peak of the PTB–Early Triassic $\delta^{34}S$

excursion, it does record the end of that excursion at the Olenekian–Anisian boundary. The positive $\delta^{34}S$ excursion in the earliest Triassic can be explained through a combination of factors:

(1) increased pyrite burial, removing ^{32}S into the sedimentary record;
(2) reduced terrestrial input of isotopically light sulphur (^{32}S) into the ocean;
(3) increased marine productivity due to oceanic overturning, leading to an expansion in BSR; and/or
(4) catastrophic mixing of deep ^{34}S-enriched brine with the surface ocean.

During this period of elevated $\delta^{34}S$, the $\delta^{13}C$ curve exhibits more ^{13}C-enriched values suggestive of a positive CIE. Positive $\delta^{13}C$ excursions can be explained through a number of mechanisms:

(1) increased organic carbon burial in the terrestrial and/or marine environments;
(2) weathering of carbonate shelves introducing ^{13}C-enriched CO_2 to the oceans; and/or
(3) transgression of continental shelves and production of extensive carbonate shelves

Of the scenarios presented above the main carbon cycle mechanism that supports the sulphur isotope record from Staithes S-20 is the increase in organic carbon burial in the marine or terrestrial environments and deposition of carbonate shelves. It is proposed that the Early Triassic experienced a rise in global sea level, oceanic over-turning, transgression over exposed continental shelves, nutrient increases from mixing continental shelf material and upwelling of anoxic organic matter, resulting in increased

organic matter productivity and burial of organic matter, expanding oxygen minimum zones and BSR production rates, causing an increase in pyrite formation and burial. This environmental scenario would cause positive excursions in both $\delta^{34}S$ and $\delta^{13}C$ (Figure 13).

The organic matter burial response would have been dominated by the marine system, since the late Permian had high biomass forests whereas in the Early Triassic it was composed of low biomass herbaceous vegetation — which is based on palynological evidence (Visscher *et al.*, 1996; Looy *et al.*, 2001). Evidence for a change in terrestrial productivity and burial is evidenced by the 'coal gap' (Bestougeff, 1980; Retallack *et al.*, 1996) in the Early Triassic. Another contributor for the drop in organic carbon productivity and burial is through a change in climate. The Early Triassic reflects a climate that has intense aridification and with less vegetation and forested regions (Berner, 2005).

Conversely, the rapid rise in the burial of sedimentary pyrite (Berner and Raiswell, 1983), as evidenced in the $\delta^{34}S$ record across the globe occurs in the Early Triassic. It has been suggested to be related to the formation of a super-anoxic ocean in the late Permian to the early-Middle Triassic, which lasted up to 20 Myrs based on stratigraphic evidence (Holser *et al.*, 1989; Kajiwara *et al.*, 1994; Wignall and Twitchett, 1996, 2002; Isozaki, 1997; Nielsen and Shen, 2004).

Sea-surface temperature has been proposed to be an important regulator on the $\delta^{13}C$ and $\delta^{34}S$ curves. A warmer period might cause an expansion of the oceanic oxygen-minimum zone and therefore, lead to a chemocline upward excursion that introduces ^{34}S-depleted sulphide and ^{13}C-depleted carbon to the surface ocean layer (Kump *et al.*, 2005). The

following oxidation of H_2S would have generated more isotopically light sulphate, resulting in a lower $\delta^{34}S$ and $\delta^{13}C$ signature during warmer intervals (Algeo *et al*., 2011; Riccardi *et al*., 2006).

Song *et al*. (2014) suggested that ocean stratification might have been intensified during Early Triassic times which would have drastically decreased the nutrient supply in the surface ocean. During this condition, any minor changes in oceanic over-turning would have had a significant impact on marine productivity and hence be reflected in the $\delta^{34}S$ and $\delta^{13}C$ curve. However, since both oceanic mixing and volcanism are typically short-term geological processes, it is unlikely that they are responsible for sustaining the $\delta^{34}S$ and $\delta^{13}C$ shift during the Early Triassic that lasted several million years (Song *et al*., 2014).

9. Conclusions

A total of 389 sediment core samples spanning the late Permian to Late Triassic from Staithes-20 Borehole, Cleveland Basin, North East England, have been analysed for carbon and sulphur isotopes. Evaporite $\delta^{34}S$ and organic $\delta^{13}C$ data from the Upper Permian Evaporite, Sherwood Sandstone Group and Mercia Mudstone Group appear to correlate with global records, except for the PTB and Early Triassic, which seems to be missing due to an erosive surface in the upper Sherwood Sandstone Group in the Staithes S-20 core. The $\delta^{34}S$ curve from the Staithes S-20 core indicate that the Sherwood Sandstone Group is dominantly Permian in age in this region. The Middle to Late Triassic record of $\delta^{34}S$ has now been expanded on by this dataset, which is the first step towards generating a robust curve for future correlation. The $\delta^{34}S$ and $\delta^{13}C$ curves show correspondence in the late–Early to Middle Triassic suggest a period of increased organic productivity, burial and anoxia leading to enhanced pyrite burial. Future studies are encouraged to provide additional $\delta^{34}S$ and $\delta^{13}C$ core records from UK and Ireland cores for the purpose of developing a national/international curve for global correlation.

10. Limitations of the Dataset

As with every study, there will always be issues that affected the dataset or how they could have been improved. The following are a set of limitations for this study:

- Scarce evaporite sample collection (n = 45) from the Sherwood Sandstone Group.
- The general undivided unit of the Sherwood Sandstone Group and Mercia Mudstone Group due to the lack of major variation in these groups. This, therefore, limited the opportunity for a more detailed correlation with other Triassic sequences across the UK.
- The lack of numerical age constrain/radiometric dating assigned to the North East Yorkshire successions, as there is very few palynological studies (Warrington, 2019) and no magnetostratigraphy in this region.
- Evaporite sulphate samples that are analysed in this study are only based on one borehole site. Hence, any conclusions drawn based on the $\delta^{34}S$ composition of Britain must be treated with caution. Additional studies on the $\delta^{34}S$ record for the rest of the UK is necessary for wider application of this technique of correlation.
- Re-analysis the organic $\delta^{13}C$ composition of organic matter that gives carbonate values towards the bottom of the core, at depth 3,449 ft (1,051.26 m) downwards; and towards the top of the core, at depth 1413.67 ft (430.89 m), 1335.42 ft (407.04 m) and 1257.50 ft (383.29 m).
- Re-analysis the three $\delta^{34}S$ anomalies for the late Permian evaporite sequence at depth 3,114.75 ft (949.38 m), 3,059.33 ft (932.48 m) and 2,998.67 ft (913.99 m).

11. Recommendations for Future Work

Limitations and suggestions for further work have been discussed throughout this thesis. As mentioned previously, the large shift in sulphur isotope composition of sulphate across the PTB recorded is not observed in the Staithes S-20 core. In order to improve the resolution scale from the existing dataset, further and additional work can be conducted on other cores in the region that span the Sherwood Sandstone Group and do not contain a major erosive surface in the upper part of the stratigraphy. Other boreholes from different basins around the UK, such as Northern Ireland boreholes (e.g., Carnduff-02, Larne, Kilroot, Cairncastle-2, Belfast Harbour) (SLR Consulting Ireland, 2014) should be investigated in order to constrain localised lithostratigraphic units to a wider/broader lithostratigraphic framework — based on sulphur isotope stratigraphy and correlation. Other geochemical analyses would help to understand the depositional environment of the anhydrite/gypsum nodules, such as performing strontium isotope analysis on the evaporite samples across the PTB and the Olenekian-Anisian boundary.

References

Aigner, T. and Bachmann, G.H., 1989. Dynamic stratigraphy of an evaporite to red bed sequence, Gipskeuper (Triassic), Southwest Germanic Basin. Sedimentary Geology, 62, p. 5–25.

Algeo, T.J., Hannigan, R., Rowe, H., Brookfield, M., Baud, A., Krystyn, L. and Ellwood, B.B., 2007. Sequencing events across the Permian–Triassic boundary, Guryul Ravine (Kashmir, India). Palaeogeography, Palaeoclimatology, Palaeoecology, 252(1-2), p. 328-346.

Algeo T.J., Luo G.M., Song H.J., Lyons T.W. and Canfield D.E., 2015. Reconstruction of secular variation in seawater sulfate concentration. Biogeoscience 12, p. 2131–2151.

Algeo, T., Shen, Y., Zhang, T., Lyons, T., Bates, S., Rowe, H. and Nguyen, T.K.T., 2008. Association of 34S-depleted pyrite layers with negative carbonate δ13C excursions at the Permian-Triassic boundary: Evidence for upwelling of sulfidic deep-ocean water masses. Geochemistry, Geophysics, Geosystems, 9(4).

Algeo, T.J., Chen, Z.Q., Fraiser, M.L. and Twitchett, R.J., 2011. Terrestrial–marine teleconnections in the collapse and rebuilding of Early Triassic marine ecosystems. Palaeogeography, Palaeoclimatology, Palaeoecology, 308(1-2), p. 1-11.

Alonso-Azcárate, J., Bottrell, S.H. and Mas, J.R., 2006. Synsedimentary versus metamorphic control of S, O and Sr isotopic compositions in gypsum evaporites from the Cameros Basin, Spain. Chemical geology, 234(1-2), p. 46-57.

Altabet, M.A. and Francois, R., 1994. Sedimentary nitrogen isotopic ratio as a recorder for surface ocean nitrate utilization. Global biogeochemical cycles, 8(1), p. 103-116.

Ambrose, K., Hough, E., Smith, N.J.P. and Warrington, G., 2014. Lithostratigraphy of the Sherwood Sandstone Group of England, Wales and south-west Scotland.

Arthur, M.A., Dean, W.E. and Claypool, G.E., 1985. Anomalous 13C enrichment in modern marine organic carbon. Nature, 315(6016), p. 216-218.

Atudorei, N.V., 1998. Constraints on the Upper Permian to Upper Triassic marine carbon isotope curve: case studies from the Tethys (Doctoral dissertation, Université de Lausanne, Faculté des sciences)

Bachmann, G.H. and Kozur, H.W., 2004. The Germanic Triassic correlation with the international chronostratigraphic scale, numerical ages, Milankovitch cyclicity. Hallesches Jahrb, Geowiss, B26, p. 17-62.

Baud, A., Magaritz, M., Holser, W.T., 1989. Permian–Triassic of the Tethys: carbon isotope studies. Geologische Rundschau 78, p. 649–677.

Beerling, D.J. and Berner, R.A., 2002. Biogeochemical constraints on the Triassic–Jurassic boundary carbon cycle event. Global Biogeochemical Cycles 16, p. 101–113.

Benton, M., Cook, E. and Turner, P., 2002. Permian and Triassic Red Beds and the Penarth Group of Great Britain: Geological Conservation Review Series, 24, p. 3-28.

Bernasconi, S.M., Meier, I., Wohlwend, S., Brack, P., Hochuli, P.A., Bläsi, H., Wortmann, U.G. and Ramseyer, K., 2017, An evaporite-based high-resolution sulfur isotope record of Late Permian and Triassic seawater sulfate. Geochimica et Cosmochimica Acta 204, p. 331-349.

Berner, E.K. and Berner, R.A., 1987. The global water cycle: geochemistry environment (No. 551.49 B47).

Berner, R.A. and Canfield, D.E., 1989. A new model for atmospheric oxygen over Phanerozoic time. American Journal of Science 289, p. 333–361.

Berner, R.A. and Raiswell, R., 1983. Burial of organic carbon and pyrite sulfur in sediments over Phanerozoic time: a new theory. Geochimica et Cosmochimica Acta 47, p. 855–862.

Berner, R.A., 1970. Sedimentary pyrite formation. American Journal of Science 268, p. 1-23.

Berner, R.A., 1984. Sedimentary pyrite formation: an update. Geochimica et Cosmochimica Acta 48, p. 605-615.

Berner, R.A., 1989. Biogeochemical cycles of carbon and sulfur and their effect on atmospheric oxygen over Phanerozoic time. Global and Planetary Change 1, p. 97–122.

Berner, R.A., 1990. Atmospheric carbon dioxide levels over Phanerozoic time. Science, 249 (4975), p. 1382-1386.

Berner, R.A., 2005. The carbon and sulfur cycles and atmospheric oxygen from middle Permian to middle Triassic. Geochimica et Cosmochimica Acta, 69(13), p. 3211-3217.

Berner, R.A., 2006. Carbon, sulfur and O2 across the Permian–Triassic boundary. Journal of Geochemical Exploration, 88(1-3), p. 416-418.

Bestougeff M. A., 1980. Summary of world coal resources and reserves. 26th Int. Geol. Congr. Paris Colloq. C-2 35, p**.** 353–366.

Beutler, G. and Szulc, J., 1999. Die paläogeographische Entwicklung des Germanischen Beckens in der Trias und die Verbindung zur Tethys. Trias: eine ganz andere Welt: Pfeil Verlag, München, p. 71-80.

Boschetti, T., Cortecchi, G., Toscani, L. and Iacumin, P., 2011, Sulfur and oxygen isotope compositions of Upper Triassic sulfates from Northerm Apennines (Italy): palaeogeographic and hidrogeochemical implications. Geologica Acta, 9(2), p. 129-147.

Boschetti, T., Venturelli, G., Toscani, L., Barbieri, M., & Mucchino, C., 2005, The Bagni di Lucca thermal waters (Tuscany, Italy): an example of Ca-SO4 waters with high Na/Cl and low Ca/SO4 ratios. Journal of Hydrology, 307(1-4), p. 270-293.

Bottjer, D.J., Clapham, M.E., Fraiser, M.L. and Powers, C.M., 2008. Understanding mechanisms for the end-Permian mass extinction and the protracted Early Triassic aftermath and recovery. GSA Today, 18(9), p. 4-10.

Bottrell S.H. and Newton R.J., 2006. Reconstruction of changes in global sulfur cycling from marine sulfate isotopes. Earth-Science Reviews 75, p. 59-83.

Bottrell, S.H. and Raiswell, R., 2000. Sulphur isotopes and microbial sulphur cycling in sediments. In Microbial sediments (pp. 96-104). Springer, Berlin, Heidelberg.

Bourquin, S., Bercovici, A., López-Gómez, J., Diez, J.B., Broutin, J., Ronchi, A., Durand, M., Arché, A., Linol, B. and Amour, F., 2011. The Permian–Triassic transition and the onset of Mesozoic sedimentation at the northwestern peri-Tethyan domain scale: palaeogeographic maps and geodynamic implications. Palaeogeography, Palaeoclimatology, Palaeoecology, 299(1-2), p.265-280.

Brack, P., Rieber, H., Nicora, A. and Mundil, R., 2005. The global boundary stratotype section and point (GSSP) of the Ladinian Stage (Middle Triassic) at Bagolino (southern Alps, northern Italy) and its implications for the Triassic time scale: Episodes, volume 28, p. 233-244.

Brayard, A., Krumenacker, L.J., Botting, J.P., Jenks, J.F., Bylund, K.G., Fara, E., Vennin, E., Olivier, N., Goudemand, N., Saucède, T. and Charbonnier, S., 2017. Unexpected Early Triassic marine ecosystem and the rise of the Modern evolutionary fauna. Science Advances, 3(2), p. 1602159.

Brennan, S.T., Lowenstein, T.K. and Horita, J., 2004. Seawater chemistry and the advent of biocalcification. Geology 32, p. 473–476.

Brookins, D.G., 1988. Seawater 87Sr/86Sr for the Late Permian Delaware Basin evaporates (New Mexico, U.S.A.). Chemical Geology, 69, p. 209–214.

Burgess, S.D., Bowring, S. and Shen, S.Z., 2014. High-precision timeline for Earth's most severe extinction: Proceedings of the National Academy of Sciences, 111, p. 3316-3321.

Burke, W.H., Denison, R.E., Hetherington, E.A., Koepnick, R.B., Nelson, H.F. and Otto, J.B., 1982. Variation of seawater 87Sr/86Sr throughout Phanerozoic time: Geology, 10, p. 516– 519.

Cameron, E.M., 1982. Sulphate and sulphate reduction in early Precambrian oceans. Nature, 296(5853), p.145-148.

Canfield, D.E. and Thamdrup, B., 1994. The production of ^{34}S-depleted sulfide during bacterial disproportionation of elemental sulfur. Science 266, p. 1973–1975.

Cao, C., Love, G.D., Hays, L.E., Wang, W., Shen, S. and Summons, R.E., 2009. Biogeochemical evidence for euxinic oceans and ecological disturbance presaging the end-Permian mass extinction event. Earth and Planetary Science Letters, 281(3-4), p.188-201.

Canfield, D.E., 2001. Isotope fractionation by natural populations of sulfate-reducing bacteria. Geochimica et Cosmochimica Acta 65, p. 1117–1124.

Caravaca, G., Thomazo, C., Vennin, E., Olivier, N., Cocquerez, T., Escarguel, G., Fara, E., Jenks, J.F., Bylund, K.G., Stephen, D.A. and Brayard, A., 2017. Early Triassic fluctuations of the global carbon cycle: New evidence from paired carbon isotopes in the western USA basin. Global and Planetary Change, 154, p. 10-22.

Caruthers, A.H., Gröcke, D.R., Kaczmarek, S.E., Rine, M.J., Kuglitsch, J. and Harrison III, W.B., 2018, Utility of organic carbon isotope data from the Salina Group halite (Michigan Basin): A new tool for stratigraphic correlation and paleoclimate proxy resource. Bulletin, 130(11-12), p. 1782-1790.

Caswell, B.A. and Dawn, S.J., 2019. Recovery of benthic communities following the Toarcian oceanic anoxic event in the Cleveland Basin, UK. Palaeogeography, Palaeoclimatology, Palaeoecology, 521, p. 114-126.

Chadwick, R.A. and Evans, D.J., 1995. The timing and direction of Permo-Triassic extension in southern Britain. Geological Society, London, Special Publications, 91(1), p. 161-192.

Claypool, G.E., Holser, W.T., Kaplan, I.R., Sakai, H. and Zak, I., 1980. The age curves of sulfur and oxygen isotopes in marine sulfate and their mutual interpretation. Chem Geology 28, p. 199–260.

Corsetti, F.A., Baud, A., Marenco, P.J. and Richoz, S., 2005. Summary of Early Triassic carbon isotope records: Comptes Rendus Palevol, 4(6-7), p. 473-486.

Cortecci, G., Reyes, E., Berti, G. and Casati, P., 1981. Sulfur and oxygen isotopes in Italian marine sulfates of Permian and Triassic ages. Chemical Geology 34, p. 65–79.

Cousminer, H. L. and Manspeizer, W., 1976. Triassic pollen date Moroccan High Atlas and the incipient rifting of Pangea as middle Carnian. Science, 191, p. 943-945.

Cramer, B.D. and Jarvis, I., 2020. Carbon Isotope Stratigraphy. In Geologic Time Scale 2020. P. 309-343. Elsevier.

Crockford, P.W., Kunzmann, M., Bekker, A., Hayles, J., Bao, H., Halverson, G.P., Peng, Y., Bui, T.H., Cox, G.M., Gibson, T.M. and Wörndle, S., 2019. Claypool continued: Extending the isotopic record of sedimentary sulfate. Chemical Geology, 513, p. 200-225.

Dal Corso, J., Mills, B.J., Chu, D., Newton, R.J., Mather, T.A., Shu, W., Wu, Y., Tong, J. and Wignall, P.B., 2020. Permo–Triassic boundary carbon and mercury cycling linked to terrestrial ecosystem collapse. Nature Communications, 11(1), p.1-9.

Detmers, J., Bruchert, V., Habicht, K.S. and Kuever, J., 2001. Diversity of sulfur isotope fractionation by sulfate-reducing prokaryotes. Applied and Environmental Microbiology 67, p. 888–894.

Doornenbal, H. and Stevenson, A., 2010. Petroleum geological atlas of the Southern Permian Basin area. EAGE.

Erwin, D., 1994. The Permo-Triassic Extinction. Nature 367 (6460), p. 231-236.

Evans, D.J., Rees, J.G. and Holloway, S., 1993. The Permian to Jurassic stratigraphy and structural evolution of the central Cheshire Basin. Journal of the Geological Society, 150(5), p. 857-870.

Fang, L., Bjerrum, C.J., Hesselbo, S.P., Kotthoff, U., McCarthy, F.M., Huang, B. and Ditchfield, P.W., 2013. Carbon-isotope stratigraphy from terrestrial organic matter through the Monterey event, Miocene, New Jersey margin (IODP Expedition 313). Geosphere, 9(5), p. 1303-1318.

Fanlo, I. and Ayora, C., 1998. The evolution of the Lorraine evaporite basin: implications for the chemical and isotope composition of the Triassic ocean. Chemical Geology, 146(3-4), p. 135-154.

Felber, R., Weissert, H.J., Furrer, H. and Bontognali, T.R., 2015. The Triassic–Jurassic boundary in the shallow-water marine carbonates from the western Northern Calcareous Alps (Austria). Swiss Journal of Geosciences, 108(2-3), p. 213-224.

Filomena, C.M. and Stollhofen, H., 2011. Ultrasonic logging across unconformities—outcrop and core logger sonic patterns of the Early Triassic Middle Buntsandstein Hardegsen unconformity, southern Germany. Sedimentary Geology, 236(3-4), p.185-196.

Fowler, A. and Robbie, J.A., 1961. Geology of the Country around Dungannon. Memoir of Geological Survey of Northern Ireland, 274.

Galfetti, T., Hochuli, P.A., Brayard, A., Bucher, H., Weissert, H. and Vigran, J.O., 2007. Smithian-Spathian boundary event: Evidence for global climatic change in the wake of the end-Permian biotic crisis. Geology, 35(4), p. 291-294.

Gallois, R W. 2001. The lithostratigraphy of the Mercia Mudstone Group (mid to late Triassic) of the south Devon coast. Geoscience in south-west England, volume 10, p. 195–204.

Gardiner, P.R.R. and Visscher, H., 1971. Permian-Triassic Transition Sequence at Kingscourt, Ireland: Nature Physical Science, 229, p. 209-210.

Gatliff, R.W., Richards, P.C., Smith, K., Graham, C.C., McCormac, M., Smith, N.J.P., Long, D., Cameron, T.D.J., Evans, D., Stevenson, A.G. and Bulat, J., 1994. United Kingdom offshore regional report: the geology of the central North Sea. British Geological Survey.

Gill, B.C., Lyons, T.W. and Saltzman, M.R., 2007. Parallel, high-resolution carbon and sulfur isotope records of the evolving Paleozoic marine sulfur reservoir. Palaeogeography, Palaeoclimatology, Palaeoecology, 256(3-4), p. 156-173.

Gorjan, P., Kaiho, K., Kakegawa, T., Niitsuma, S., Chen, Z. Q., Kajiwara, Y., and Nicora, A., 2007. Paleoredox, biotic and sulfur-isotopic changes associated with the end-Permian mass extinction in the western Tethys. Chemical Geology, 244(3-4), p. 483-492.

Gradinaru, E., Orchard, M.J., Nicora, A., Gallet, Y., Besse, J., Krystyn, L., Sobolev, E.S., Atudorei, N-V. and Ivanova, D., 2007. The Global Boundary Stratotype Section and Point (GSSP) for the base of the Anisian Stage: Desli Caira Hill, North Dobrogea, Romania: Albertiana, volume 36, p. 54-71.

Gradstein, F.M., Ogg, J.G., Schmitz, M. and Ogg, G. eds., 2012. The geologic time scale 2012. Elsevier.

Grice, K., Cao, C., Love, G.D., Böttcher, M.E., Twitchett, R.J., Grosjean, E., Summons, R.E., Turgeon, S.C., Dunning, W. and Jin, Y., 2005. Photic zone euxinia during the Permian-Triassic superanoxic event. Science, 307(5710), p. 706-709.

Gröcke, D.R., 2020. Carbon isotope stratigraphy: Principles and applications. Carbon Isotope Stratigraphy, 5, p.1.

Gust, D.A., Biddle, K.T., Phelps, D.W. and Uliana, M.A., 1985. Associated Middle to Late Jurassic volcanism and extension in southern South America. Tectonophysics, 116(3-4), p. 223-253.

Habicht, K.S. and Canfield, D.E., 1996. Sulphur isotope fractionation in modern microbial mats and the evolution of the sulphur cycle. Nature 382, p. 342–343.

Habicht, K.S. and Canfield, D.E., 1997. Sulfur isotope fractionation during bacterial sulfate reduction in organic-rich sediments. Geochimica et Cosmochimica Acta 61, p. 5351–5361.

Habicht, K.S. and Canfield, D.E., 2001. Isotope fractionation by sulfate- reducing natural populations and the isotopic composition of sulfide in marine sediments. Geology 29, p. 555–558.

Hay, W.W., Migdisov, A., Balukhovsky, A.N., Wold, C.N., Flögel, S. and Söding, E., 2006. Evaporites and the salinity of the ocean during the Phanerozoic: Implications for climate,

ocean circulation and life. Palaeogeography, Palaeoclimatology, Palaeoecology, 240(1-2), p. 3-46.

Herrmann, A., Hinze, C. and Stein, V., 1967. Die halotektonische Deutung der Elfas-Überschiebung im südniedersächsischen Bergland.

Hesselbo, S.P., Robinson, S.A., Surlyk, F. and Piasecki, S., 2002. Terrestrial and marine extinction at the Triassic-Jurassic boundary synchronized with major carbon-cycle perturbation: A link to initiation of massive volcanism? Geology, 30(3), p. 251-254.

Hochuli, P.A., Sanson-Barrera, A., Schneebeli-Hermann, E. and Bucher, H., 2016. Severest crisis overlooked—Worst disruption of terrestrial environments postdates the Permian–Triassic mass extinction. Scientific Reports, 6, p. 28372.

Holser W.T. and Kaplan I.R., 1966. Isotope geochemistry of sedimentary sulfates. Chemical Geology, 1, p. 93–135.

Holser, W.T., 1977. Catastrophic chemical events in the history of the ocean. Nature, 267, p. 403-407.

Holser, W.T., Maynard, J.B. and Cruikshank, K.M., 1989. Modelling the natural cycle of sulphur through Phanerozoic time. Evolution of the global biogeochemical sulphur cycle, p. 21-56.

Holser, W.T., Schidlowski, M., Mackenzie, F.T. and Maynard, J.B., 1988. Geochemical cycles of carbon and sulfur. In: Gregor, C.B., Garrels, R.M., Mackenzie, F.T., Maynard, J.B. (Eds.), Chemical Cycles in the Evolution of the Earth. John Wiley and Sons, Inc., p. 276.

Horacek, M., Brandner, R. and Abart, R., 2007. Carbon isotope record of the P/T boundary and the Lower Triassic in the Southern Alps: evidence for rapid changes in storage of organic carbon. Palaeogeography, Palaeoclimatology, Palaeoecology, 252(1-2), p. 347-354.

Horacek, M., Brandner, R., Richoz, S. and Karadeniz, E.P., 2010. Lower Triassic sulphur isotope curve of marine sulphates from the Dolomites, N-Italy. Palaeogeography, Palaeoclimatology, Palaeoecology, 290, p. 65-70.

Horita, J., Zimmermann, H. and Holland, H.D., 2002. Chemical evolution of seawater during the Phanerozoic: implications from the record of marine evaporites. Geochimica et Cosmochimica Acta 66, p. 3733–3756.

Howard, A. S., Warrington, G., Ambrose, K., and Rees, J. G., 2008. A formational framework for the Mercia Mudstone Group (Triassic) of England and Wales: British Geological Survey Research Report, RR/08/04.

Hu, F., Fu, X., Lin, L., Song, C., Wang, Z. and Tian, K., 2020. Marine Late Triassic-Jurassic carbon-isotope excursion and biological extinction records: New evidence from the Qiangtang Basin, eastern Tethys. Global and Planetary Change, 185, p.103093.

Insalaco, E., Virgone, A., Courme, B., Gaillot, J., Kamali, M., Moallemi, A., Lotfpour, M. and Monibi, S., 2006. Upper Dalan Member and Kangan Formation between the Zagros Mountains and offshore Fars, Iran: depositional system, biostratigraphy and stratigraphic architecture. GeoArabia, 11(2), p. 75-176.

Isozaki, Y., 1997. Permo-Triassic boundary superanoxia and stratified superocean: records from lost deep sea. Science, 276 (5310), p. 235-238.

Isozaki, Y., 2009. Illawarra Reversal: the fingerprint of a superplume that triggered Pangean breakup and the end- Guadalupian (Permian) mass extinction. Gondwana Research, 15, p. 421–432.

Jarvis, I., Lignum, J.S., Gröcke, D.R., Jenkyns, H.C. and Pearce, M.A., 2011. Black shale deposition, atmospheric CO_2 drawdown, and cooling during the Cenomanian- Turonian Oceanic Anoxic Event. Paleoceanography, 26, Pa3201.

Jarvis, I., Trabucho-Alexandre, J., Gröcke, D.R., Uličný, D. and Laurin, J., 2015. Intercontinental correlation of organic carbon and carbonate stable isotope records: evidence of climate and sea-level change during the Turonian (Cretaceous). The Depositional Record, 1(2), p. 53-90.

Jeans, C.V., 2006. Clay mineralogy of the Permo-Triassic strata of the British Isles: onshore and offshore. Clay Minerals, 41(1), p. 309-354.

Kaiho, K., Kajiwara, Y., Nakano, T., Miura, Y., Kawahata, H., Tazaki, K., Ueshima, M., Chen,Z., Shi, G.R., 2001. End-Permian catastrophe by a bolide impact; evidence of a gigantic release of sulfur from the mantle. Geology 29 (9), p. 815–818.

Kajiwara, Y., Yamakita, S., Ishida, K., Ishiga, H. and Imai, A., 1994. Development of a largely anoxic stratified ocean and its temporary massive mixing at the Permian/Triassic boundary supported by the sulfur isotopic record. Palaeogeography, Palaeoclimatology, Palaeoecology 111, p. 367–379.

Kampschulte, A. and Strauss, H., 2004. The Sulfur Isotopic Evolution of Phanerozoic Sea Water Based on the Analysis of Structurally Substituted Sulfate in Carbonates, Chemical Geology, 204, p. 255-286.

Kampschulte, A., Buhl, D. and Strauss, H., 1998. The sulfur and strontium isotopic compositions of Permian evaporites from the Zechstein basin, northern Germany. Geologische Rundschau, 87(2), p. 192-199.

Kani, T., Fukui, M., Isozaki, Y. and Nohda, S., 2008. The Paleozoic minimum of 87Sr/86Sr ratio in the Capitanian (Permian) mid-oceanic carbonates: a critical turning point in the Late Paleozoic. Journal of Asian Earth Sciences, 32, p. 22–33.

Kent, P. E., 1967. Outline Geology of the Southern North Sea Basin: Proceedings of the Yorkshire Geological Society, volume 36, part 1, no. 1, p. 1-22.

Kirkland, D.W. and Gerhard, J.E., 1971. Jurassic salt, central Gulf of Mexico, and its temporal relation to circum-Gulf evaporites. American Association of Petroleum Geologists Bulletin, 55, p. 680-686.

Knoll, A.H., Bambach, R.K., Canfield, D.E., and Grotzinger, J.P., 1996, Comparative Earth history and Late Permian mass extinction: Science, volume 273, p. 452–457.

Knies, J., Grasby, S.E., Beauchamp, B. and Schubert, C.J., 2013. Water mass denitrification during the latest Permian extinction in the Sverdrup Basin, Arctic Canada. Geology, 41(2), p. 167-170.

Kocsis, Á.T. and Scotese, C.R., 2020. Mapping paleocoastlines and continental flooding during the Phanerozoic. Earth-Science Reviews, p.103463.

Korte, C. and Ullmann, C.V., 2018. Permian strontium isotope stratigraphy. In Lucas, S. G. & Shen, S. Z. (eds.) The Permian Timescale. Geological Society, London, Special Publications, 450.

Korte, C., Jasper, T., Kozur, H.W. and Veizer, J., 2006. 87Sr/86Sr record of Permian seawater. Palaeogeography, Palaeoclimatology, Palaeoecology, 240, p. 89–107.

Korte, C., Kozur, H.W. and Veizer, J., 2005. δ13C and δ18O values of Triassic brachiopods and carbonate rocks as proxies for coeval seawater and palaeotemperature. Palaeogeography, Palaeoclimatology, Palaeoecology, 226(3-4), p.287-306.

Korte, C., Kozur, H.W., Bruckschen, P. and Veizer, J., 2003. Strontium isotope evolution of Late Permian and Triassic seawater. Geochemica et Cosmochimica Acta, 67, p. 47–62.

Korte, C., Kozur, H.W., Joachimski, M.M., Strauss, H., Veizer, J., Schwark, L., 2004. Carbon, sulfur, oxygen and strontium isotope records, organic geochemistry and biostra-tigraphy across the Permian/Triassic boundary in Abadeh, Iran. International Journal of Earth Science 93, p. 565–581.

Kramm, U. and Wedepohl, K.H., 1991. The Isotopic Composition of Strontium and Sulfur in Seawater of Late Permian (Zechstein) Age, Chemical Geology, 90, 253.

Krouse, H.R. and Grinenko, V.A., 1991. Stable isotopes: natural and anthropogenic sulphur in the environment.

Kump, L.R., 1991. Interpreting carbon-isotope excursions – Stangelove oceans. Geology, 19, p. 299–302.

Kump, L.R., Pavlov, A. and Arthur, M.A., 2005. Massive release of hydrogen sulfide to the surface ocean and atmosphere during intervals of oceanic anoxia. Geology 33, p. 397–400.

Kürschner, W.M. and Herngreen, G.F.W., 2010. Triassic palynology of central and northwestern Europe: a review of palynofloral diversity patterns and biostratigraphic subdivisions. In: Lucas, S.G. (Ed.), The Triassic Timescale: Geological Society, London, Special Publications, 334, p. 263–283.

Kutzbach, J.E. and Gallimore, R.G., 1989. Pangaean climates – Megamonsoons of the megacontinent. Journal of Geophysical Research – Atmospheres, 94, p. 3341–3357.

Larson, A. L., 1966. Stratigraphy and Paleontology of the Moenkopi Formation in southern Nevada. Ph.D. Dissertation, University of California, Los Angeles, California.

Legler, B. and Schneider, J. W., 2008. Marine ingressions into the Middle/Late Permian saline lake of the Southern Permian Basin (Rotliegend, Northern Germany) possibly linked to sea-level highstands in the Arctic rift system. Palaeogeogr. Palaeoclimatol. Palaeoecol. 267, p. 102–114.

Legler, B., Gebhardt, U., Schneider, J.W., 2005. Late Permian non-marine–marine transitional profiles in the central Southern Permian Basin, north Germany. Int. J. Earth Sci. (Geol. Rundsch.) 94, p. 851–862.

Lehrmann, D.J., Ramezani, J., Bowring, S.A., Martin, M.W., Montgomery, P., Enos, P., Payne, J.L., Orchard, M.J., Wang, H. and Wei, J., 2006. Timing of recovery from the end-Permian extinction: Geochronologic and biostratigraphic constraints from south China. Geology 34, p. 1053-1056.

Lervik, K.S., Spencer, A.M. and Warrington, G., 1989. Outline of Triassic stratigraphy and structure in the central northern North Sea. In: Collinson, J. D. (eds.) Correlation in Hydrocarbon Exploration, Graham & Trotman, London. p. 173-189.

Longinelli, A. and Flora, O., 2007. Isotopic composition of gypsum samples of Permian and Triassic age from the north-eastern Italian Alps: Palaeoenvironmental implications. Chemical Geology, 245(3-4), p. 275-284.

Looy C. V., Twitchett R. J., Dilcher D. L., Van Konijnenburg-Van Cittert J. H. A., and Visscher H., 2001. Life in the end-Permian dead zone. Proc. Natl. Acad. Sci. U. S. A. 98, p. 7879–7883.

Lowenstein, T.K., Hardie, L.A., Timofeeff, M.N. and Demicco, R.V., 2003. Secular variation in seawater chemistry and the origin of calcium chloride basinal brines. Geology 31, p. 857–860.

Lowenstein, T.K., Timofeeff, M.N., Kovalevych, V.M. and Horita, J., 2005. The major-ion composition of Permian seawater. Geochimica et Cosmochimica Acta 69, p. 1701–1719.

Lucas, S.G., 2013. A new Triassic timescale. In Tanner, L. H., Spielmann, J. A. and Lucas, S, G. (eds.), 2013. The Triassic System. New Mexico Museum of Natural History and Science, Bulletin 61.

Lucas, S.G., 2010. The Triassic timescale: an introduction. Geological Society, London, Special Publications, 334(1), p. 1-16.

Luo, G., Kump, L.R., Wang, Y., Tong, J., Arthur, M.A., Yang, H., Huang, J., Yin, H. and Xie, S., 2010. Isotopic evidence for an anomalously low oceanic sulfate concentration following end-Permian mass extinction. Earth and Planetary Science Letters, 300(1-2), p. 101-111.

Luo, G., Wang, Y., Algeo, T.J., Kump, L.R., Bai, X., Yang, H., Yao, L. and Xie, S., 2011. Enhanced nitrogen fixation in the immediate aftermath of the latest Permian marine mass extinction. Geology, 39(7), p. 647-650.

MacNamara, J., Thode, H. G., 1950. Comparison of the isotopic constitution of terrestrial and meteoritic sulphur. Physics Review 78, p. 307.

Magaritz, M., Krishnamurthy, R.V. and Holser, W.T., 1992. Parallel trends in organic and inorganic carbon isotopes across the Permian/Triassic boundary. American Journal of Science;(United States), 292(10).

Manning, P.I., Robbie, J.A. and Wilson, H.E., 1970. Geology of Belfast and Lagan Valley. Memoirs of Geological Survey Northern Ireland. 242.

Marenco, P.J., Corsetti, F.A., Hammond, D.E., Kaufman, A.J. and Bottjer, D.J., 2008a. Oxidation of pyrite during extraction of carbonate associated sulfate. Chemical Geology, 247(1-2), p. 124-132.

Marenco, P.J., Corsetti, F.A., Kaufman, A.J. and Bottjer, D.J., 2008b. Environmental and diagenetic variations in carbonate associated sulfate: an investigation of CAS in the Lower Triassic of the western USA. Geochimica et Cosmochimica Acta, 72(6), p. 1570-1582.

McKee, E.D., 1954. Stratigraphy and history of the Moenkopi Formation of Triassic age (Volume 61). Geological Society of America.

McKie, T. and Williams, B., 2009. Triassic palaeogeography and fluvial dispersal across the northwest European Basins. Geological Journal, 44(6), p. 711-741.

McKie, T., 2017. Paleogeographic evolution of latest Permian and Triassic salt basins in Northwest Europe. In Permo-Triassic Salt Provinces of Europe, North Africa and the Atlantic Margins (pp. 159-173). Elsevier.

Meyer, K.M., Yu, M., Lehrmann, D., Van de Schootbrugge, B. and Payne, J.L., 2013. Constraints on Early Triassic carbon cycle dynamics from paired organic and inorganic carbon isotope records. Earth and Planetary Science Letters, 361, p. 429-435.

Meyerhoff, A.A. and Hatten, C.W., 1968. Diapiric structures in central Cuba. American Association of Petroleum Geologists Memorial, 8, p. 315-357.

Mietto, P., Manfrin, S., Preto, N., Rigo, M., Roghi, G., Furin, S., Gianolla, P., Posenato, R., Muttoni, G., Nicora, A. and Buratti, N., 2012. The global boundary stratotype section and point (GSSP) of the Carnian stage (Late Triassic) at Prati di Stuores/Stuores Wiesen section (Southern Alps, NE Italy). Episodes-Newsmagazine of the InternationalUnion of Geological Sciences, 35(3), p. 414.

Naylor, H., Turner, P., Vaughan, D.J., Boyce, A.J. and Fallick, A.E., 1989. Genetic studies of red bed mineralization in the Triassic of the Cheshire Basin, Northwest England. Journal of the Geological Society, London, 146, p. 685-700.

Neretin, L.N., Böttcher, M.E. and Grinenko, V.A., 2003. Sulfur isotope geochemistry of the Black Sea water column. Chemical Geology, 200(1-2), p. 59-69.

Newton, R. and Bottrell, S., 2007. Stable isotopes of carbon and sulphur as indicators of environmental change: past and present. Journal of the Geological Society, 164(4), p. 691-708.

Newton, R.J., Pevitt, E.L., Wignall, P.B., Bottrell, S.H., 2004. Large shifts in the isotopic composition of seawater sulphate across the Permo-Triassic boundary in northern Italy. Earth and Planetary Science Letters 218, p. 331–345.

Nielsen, H., 1965. Schwefelisotope im marinen Kreislauf und das d34S der früheren Meere. Geologische Rundschau 55, p. 127–140.

Nielsen, H., Ricke, W., 1964. Schwefel-Isotopenverhältnisse von Evaporiten aus Deutschland; Ein Beitrag zur Kenntnis von d34S im Meerwasser-Sulfat. Geochimica Cosmochimica Acta 28, p. 577–591.

Nielsen, J.K. and Shen, Y., 2004. Evidence for sulfidic deep water during the Late Permian in the East Greenland Basin. Geology, 32(12), p. 1037-1040.

Ohkouchi, N., Kawamura, K., Kajiwara, Y., Wada, E., Okada, M., Kanamatsu, T. and Taira, A., 1999. Sulfur isotope records around Livello Bonarelli (northern Apennines, Italy) black shale at the Cenomanian-Turonian boundary. Geology, 27(6), p. 535-538

Orchard, M.J., 2010. Triassic conodonts and their role in stage boundary definition; in Lucas, S.G., ed., The Triassic timescale: Geological Society London, Special Publication 334, p. 139-161.

Orchard, M.J., 2013. Five new genera of conodonts from the Carnian- Norian boundary beds of Black Bear Ridge, northeast British Columbia, Canada: New Mexico Museum of Natural History and Science, Bulletin 61, this volume.

Orchard, M.J., Gradinaru, E. and Nicora, A., 2007. A summary of the conodont succession around the Olenekian-Anisian boundary at Desli Caira, north Dobrogea, Romania: New Mexico Museum of Natural History and Science, Bulletin 41, p. 341-346.

Ovtcharova, M., Bucher, H., Schaltegger, U., Galfetti, T., Brayard, A. and Guex, J., 2006. New Early to Middle Triassic U-Pb ages from South China: Calibration with ammonoid biochronozones and implications for the timing of the Triassic biotic recovery. Earth Planet. Sci. Lett. 243, p. 463-475.

Pak, E. 1978. Schwefelisotopenuntersuchungen am Institut für Radiumforschung und Kernphysik, II Anz. Österr. Akad. Wiss., Math.-Naturwiss. Kl. (1978), pp. 7-22.

Parrish, J.T., 1993. Climate of the supercontinent Pangaea. Journal of Geology, 101, p. 215–233.

Pattison, J., Smith, D.B. and Warrington, G., 1973. A Review of Late Permian and Early Triassic Biostratigraphy in the British Isles: Permian Triassic Systems and Their Mutual Boundary, Memoir 2, p. 220-260.

Payne, J.L., Lehrmann, D.J., Wei, J., Orchard, M.J., Schrag, D.P. and Knoll, A.H., 2004. Large perturbations of the carbon cycle during recovery from the end-Permian extinction. Science, 305(5683), p. 506-509.

Paytan A. and Gray E. T., 2012. Sulfur Isotope Stratigraphy in Gradstein, F. M., Ogg, J. G., Schmitz, M. D. and Ogg, G. M., eds., The Geological Timescale: Elsevier, chapter 9, p. 167- 180.

Paytan, A., Gray, E.T., Ma, Z., Erhardt, A. and Faul, K., 2011, Application of sulphur isotopes for stratigraphic correlation. Isotopes in environmental and health studies, 48(1), p. 195-206.

Paytan, A., Yao, W., Faul, K.L. and Gray, E.T., 2020. Sulfur isotope stratigraphy. In Geologic Time Scale 2020. P. 259-278. Elsevier.

Pearson, F.J., Balderer, W., Loosli, H.H., Lehmann, B.E., Matter, A., Peters, T., Schmassmann, H. and Gautschi, R.U. eds., 1991. Applied isotope hydrogeology: a case study in northern Switzerland. Elsevier.

Peryt, T., Morawiec, H.T., Czapowski, G., Hryniv, S.P., Pueyo, J.J., Eastoe, C.J. and Vovnyuk, S., 2005. Polyhalite occurrence in the Werra (Zechstein, Upper Permian) peribaltic basin of Poland and Russia: Evaporite facies constraints: Carbonates and Evaporites, 20, 2, p. 182-194.

Peryt, T.M., Jasionowski, M., Karoli, S., Petrichenko, O.I., Poberegski, A.V. and Turchinov, I.I., 1998. Correlation and sedimentary history of the Badenian gypsum in the Carpathian Foredeep (Ukraine, Poland, and Czech Republic). Przegląd Geologiczny, 46(8-2), p. 729-732.

Peryt, T.M., Lalas, S. and Hryniv, S.P., 2010. Sulphur and oxygen isotope signatures of late Permian Zechstein anhydrites, West Poland: seawater evolution and diagenetic constraints: Geological Quarterly, 54 (4), p. 387-400.

Porter, E. M., 2003. The Triassic System in N. Ireland: Earth Science Conservation Review 1192.

Present, T.M., Adkins, J.F. and Fischer, W.W., 2020. Variability in sulfur isotope records of Phanerozoic seawater sulfate. Geophysical Research Letters, 47(18), p.e2020GL088766.

Raab, M. and Spiro, B., 1991. Sulfur isotopic variations during seawater evaporation with fractional crystallization. Chemical Geology: Isotope Geoscience section, 86(4), p. 323-333.

Rees, C.E., 1970. The sulphur isotope balance of the ocean: an improved model. Earth and Planetary Science Letters, 7(4), p. 366-370.

Rees, C.E., Jenkins, W.J. and Monster, J., 1978. The sulphur isotopic composition of ocean water sulphate. Geochimica et Cosmochimica Acta, 42(4), p. 377-381.

Retallack G. J., Veevers J. J., and Morante R., 1996. Global coal gap between Permian-Triassic extinction and middle Triassic recovery of peat-forming plants. Geological Society American Bulletin 108**,** p. 195–207.

Retallack, G.L., 1999. Postapocalyptic greenhouse paleoclimate revealed by earliest Triassic paleosols in the Sydney Basin, Australia. Geological Society of America Bulletin 111, p. 52–70.

Riccardi, A.L., Arthur, M.A. and Kump, L.R., 2006. Sulfur isotopic evidence for chemocline upward excursions during the end-Permian mass extinction. Geochimica et Cosmochimica Acta, 70(23), p. 5740-5752.

Richoz, S., 2006. Stratigraphie et variations isotopiques du carbone dans le Permien supérieur et le Trias inférieur de quelques localités de la Néotéthys (Turquie, Oman et Iran) (pp. 1-275). Univ. de Lausanne-Institut de Géologie et Paléontologie.

Richoz, S., Krystyn, L., Horacek, M. and Spötl, C., 2007. Carbon isotope record of the Induan-Olenekian candidate GSSP Mud and comparison with other sections. Albertiana, 35, p. 35-40.

Rick, B., 1990. Sulphur and oxygen isotopic composition of Swiss Gipskeuper (Upper Triassic). Chemical Geology: Isotope Geoscience section, 80(3), p. 243-250.

Ruffell, A. and Shelton, R., 1999. The control of sedimentary facies by climate during phases of crustal extension examples from the Triassic of onshore and offshore England and Northern Ireland. Journal of the Geological Society of London, volume 156, p. 779-789.

Ruhl, M., Veld, H. and Kürschner, W.M., 2010. Sedimentary organic matter characterization of the Triassic–Jurassic boundary GSSP at Kuhjoch (Austria). Earth and Planetary Science Letters, 292(1-2), p. 17-26.

Saitoh, M., Ueno, Y., Nishizawa, M., Isozaki, Y., Takai, K., Yao, J. and Ji, Z., 2014. Nitrogen isotope chemostratigraphy across the Permian–Triassic boundary at Chaotian, Sichuan, South China. Journal of Asian Earth Sciences, 93, p.113-128.

Saltzman, M.R. and Thomas, E., 2012. Carbon isotope stratigraphy. The geologic time scale, 1, p. 207-232.

Sanson-Barrera, A., Hochuli, P.A., Bucher, H., Meier, M., Schneebeli-Hermann, E., Weissert, H. and Bernasconi, S.M., 2013. Latest Permian to Early Triassic high-resolution stable carbon isotope record from North-east Greenland.

Schobben, M., Joachimski, M.M., Korn, D., Leda, L. and Korte, C., 2014. Palaeotethys seawater temperature rise and an intensified hydrological cycle following the end-Permian mass extinction. Gondwana Research, 26(2), p. 675-683.

Scholze, F., Schneider, J. W. and Werneburg, R., 2016. Conchostracans in continental deposits of the Zechstein-Buntsandstein transition in central Germany: Taxonomy and biostratigraphic implications for the position of the Permian-Triassic boundary within the Zechstein Group. Palaeogeography Palaeoclimatology Palaeoecology, 449, p. 174-193.

Scholze, F., Wang, X., Kirscher, U., Kraft, J., Schneider, J.W., Götz, A.E., Joachimski, M. M. and Bachtadse, V., 2017. A multistratigraphic approach to pinpoint the Permian-Triassic boundary in continental deposits: The Zechstein-Lower Buntsandstein transition in Germany: Global and Planetary Change 152, p. 129-151.

Scotese, C.R., 2001. Paleomap Project.

Selwood, B.W. and Valdes, P.J., 2007. Mesozoic climates. In: Haywood, W. M., Gregory, A. M. and Schmidt, D. N. (eds.) Deep-time perspectives on climate change: marrying the signal from computer models and biological proxies. The Micropalaeontological Society, Special Publications. The Geological Society, London, p. 201–224.

Simms, M.J. and Ruffell, A.H., 1989. Synchroneity of climatic change and extinctions in the Late Triassic. Geology, 17(3), p. 265-268.

Simms, M.J. and Ruffell, A.H., 1990. Climatic and biotic change in the late Triassic. Journal of the Geological Society, 147(2), pp.321-327.

SLR Consulting Ireland, 2014. Compressed Air Energy Storage Larne, Co. Antrim, Carnduff 02 Final Well Report.

Smith, D. B., 1989. The late Permian palaeogeography of north-east England: Proceedings of the Yorkshire Geological Society, Vol. 47, Part 4, p. 285-312.

Smith, D.B., Brunstrom, R.G.W., Manning, P.I., Simpson, S. and Shotton, F.W., 1974. A correlation of Permian rocks in the British Isles: Geological Society, special report no. 5, volume, 130, p. 1-45.

Smith, F.W., Dearlove, J.P.L., Kemp, S.J., Bell, C.P., Milne, C.J. and Pottas, T.L., 2014. Potash—recent exploration developments in North Yorkshire. In Proceedings of the 17th Extractive Industry Geology Conference, EIG Conferences Ltd (p. 45-50).

Smith, R. A., 1986. Permo-Triassic and Dinantian rocks of the Belfast Harbour Borehole. Report of the British Geological Survey, Volume 18, number 6.

Song, H., Tong, J., Algeo, T.J., Horacek, M., Qiu, H., Song, H., Tian, L. and Chen, Z.Q., 2013. Large vertical δ13C DIC gradients in Early Triassic seas of the South China craton: Implications for oceanographic changes related to Siberian Traps volcanism. Global and Planetary Change, 105, p. 7-20.

Song, H., Tong, J., Algeo, T.J., Song, H., Qiu, H., Zhu, Y., Tian, L., Bates, S., Lyons, T.W., Luo, G. and Kump, L.R., 2014. Early Triassic seawater sulfate drawdown. Geochimica et Cosmochimica Acta, 128, p. 95-113.

Song, H., Wignall, P.B. and Dunhill, A.M., 2018. Decoupled taxonomic and ecological recoveries from the Permo-Triassic extinction. Science Advances, 4(10), p.5091.

Spötl, C. and Pak, E., 1996. A strontium and sulfur isotopic study of Permo-Triassic evaporites in the Northern Calcareous Alps, Austria. Chemical Geology, 131(1-4), p. 219-234.

Spinks, S.C., Parnell, J. and Bowden, S.A., 2010. Reduction spots in the Mesoproterozoic age: implications for life in the early terrestrial record. International Journal of Astrobiology, 9(4), p. 209.

Stampfli, G.M. and Borel, G.D., 2002. A plate tectonic model for the Paleozoic and Mesozoic constrained by dynamic plate boundaries and restored synthetic oceanic isochrons. Earth Planetary Science Letters 196, p. 17–33.

Stebbins, A., Algeo, T.J., Krystyn, L., Rowe, H., Brookfield, M., Williams, J., Nye Jr, S.W. and Hannigan, R., 2019. Marine sulfur cycle evidence for upwelling and eutrophic stresses during Early Triassic cooling events. Earth-Science Reviews, 195, p. 68-82.

Steel, R.J. and Ryseth, A., 1990. The Triassic-early Jurassic succession in the northern North Sea: megasequence stratigraphy and intra-Triassic tectonics. In: Hardman, R. F. P. and Brooks, J. (eds.) Tectonic Events Responsible for Britain's Oil and Gas Reserves. Geological Society, London, Special Publication, 55, p. 139-168.

Stone, P. (2015) Permian and Mesozoic basins of England and Wales, Bedrock geology UK south: Earthwise, British Geological Survey, P.785821 (online) <http://earthwise.bgs.ac.uk/images/4/4c/P785821.jpg>. Last accessed on 20/1/2021.

Strauss, H., 1997. The isotopic composition of sedimentary sulfur through time. Palaeogeography, palaeoclimatology, palaeoecology, 132(1-4), p. 97-118.

Strohmenger, C. and Strauss, C., 1996. Sedimentology and palynofacies of the Zechstein 2 Carbonate (Upper Permian, Northwest Germany): implications for sequence stratigraphic subdivision. Sedimentary Geology 102, p. 55–77.

Strohmenger, C., Voigt, E. and Zimdars, J., 1996. Sequence stratigraphy and cyclic development of Basal Zechstein carbonate-evaporite deposits with emphasis on Zechstein 2 off-platform carbonates (Upper Permian, Northeast Germany). Sed. Geol. 102, p. 33–54.

Szurlies, M., 2005. Zyklostratigraphische Kalibrierung 2005, Buntsandstein. In: Menning, M., Gast, R., Hagdorn, H., Käding, K. -C., Simon, T., Szurlies, M. and Nitsch, E. (Eds.), Zeitskala für Perm und Trias in der Stratigraphischen Tabelle von Deutschland 2002, zyklostratigraphische Kalibrierung der höheren Dyas und Germanischen Trias und das Alter der Stufen Roadium bis Rhaetium 2005. Newsl. Stratigr., volume 43, p. 173-210.

Szurlies, M., 2007. Latest Permian to Middle Triassic cyclo-magnetostratigraphy from the Central European Basin, Germany: implications for the geomagnetic polarity timescale. Earth and Planetary Science Letters 261, p. 602–619.

Szurlies, M., Geluk, M.C., Krijgsman, W. and Kürschner, W.M., 2012. The continental Permian-Triassic boundary in the Netherlands: Implications for the geomagnetic polarity time scale. Earth and Planetary Science Letters, 317-318, p. 165-176.

Tavakoli, V., 2015. Chemostratigraphy of the Permian–Triassic strata of the offshore Persian Gulf, Iran. In Chemostratigraphy, Elsevier. P. 373-393.

Thode, H. G. and Monster, J., 1965. Sulfur-isotope Geochemistry of Petroleum, Evaporites, and ancient seas, in Young, A. and Galley, J. E., eds., Fluids in Subsurface Environments: American Association of Petroleum Geologists, Volume 4, p. 367-377.

Thompson, J. and Meadows, N.S., 1997. Clastic sabkhas and diachroncity at the top of the Sherwood Sandstone Group: East Irish Sea Basin: Geological Society, London, Special Publications, 124, p. 237-251.

Tikhomirov, P.L., Chalot-Prat, F. and Nazarevich, B.P., 2004. Triassic volcanism in the Eastern Fore-Caucasus: evolution and geodynamic interpretation. Tectonophysics, 381(1-4), p.119-142.

Tollmann, A. and Kristan-Tollmann, E., 1985. Late Permian to early Mesozoic rifting and sedimentation offshore NW Ireland: Marine and Petroleum Geology, 6, p. 49-59.

Trusheim, F. 1963. Zur Gliederung des Buntsandsteins. Erdoel Zschr. 7, p. 277-292.

Uličný, D., Jarvis, I., Gröcke, D.R., Čech, S., Laurin, J., Olde, K., Trabucho-Alexandre, J., Švábenická, L. and Pedentchouk, N., 2014. A high-resolution carbon-isotope record of the Turonian stage correlated to a siliciclastic basin fill: Implications for mid-Cretaceous sea-level change. Palaeogeography, Palaeoclimatology, Palaeoecology, 405, p. 42-58.

Utrilla, R., Pierre, C., Orti, F. and Pueyo, J.J., 1992. Oxygen and sulphur isotope compositions as indicators of the origin of Mesozoic and Cenozoic evaporites from Spain. Chemical Geology, 102(1-4), p. 229-244.

Veizer, J. and Compston, W., 1974. 87Sr/86Sr composition of seawater during the Phanerozoic. Geochimica et Cosmochimica Acta, 38, p. 1461–1484.

Veizer, J., Holser, W.T. and Wilgus, C.K., 1980. Correlation of 13C/12C and 34S/32S secular variations. Geochimica et Cosmochimica Acta, 44, p. 579-587.

Visscher H., Brinkhuis H., Dilcher D. L., Elsik W. C., Eshet Y., Looy C. V., Rampino W. R., and Travers A., 1996. The terminal Paleozoic fungal event: Evidence of terrestrial ecosystem destabilization and collapse. Proc. Natl. Acad. Sci. U. S. A. 93, p. 2155–2158.

Visscher, H., 1971. The Permian and Triassic of the Kingscourt outlier: a palynological investigation related to regional stratigraphical problems in the Permian and Triassic of western European Geological Survey Ireland Special Paper 1, p. 1–114.

Von Hillebrandt, A., Krystyn, L. and Kuerschner, W.M., with contributions from Bown, P. R., McRoberts, C., Ruhl, M.S., Simms, M., Tomasovych, A. and Urlichs, M., 2007. A candidate GSSP for the base of the Jurassic in the Northern Calcareous Alps (Kuhjoch section, Karwendel Mountains, Tyrol, Austria: International Subcommission on Jurassic Stratigraphy Newsletter, no. 34, p. 2-20.

Ware, D., Bucher, H., Brayard, A., Schneebeli-Hermann, E. and Brühwiler, T., 2015. High-resolution biochronology and diversity dynamics of the Early Triassic ammonoid recovery: the Dienerian faunas of the Northern Indian Margin. Palaeogeography, Palaeoclimatology, Palaeoecology, 440, p. 363-373.

Warrington, G. and Ivimey-Cook, H. C. 1992. Triassic. 97-106 in Atlas of palaeogeography and lithofacies. Cope, J. C. W., Ingham, J. K., and Rawson, P. F. (editors). Memoir of the Geological Society of London, No. 13.

Warrington, G, and Ivimey-Cook, H C. 1995. The Late Triassic and Early Jurassic of coastal sections in west Somerset and south and mid-Glamorgan. P. 9–30 in Field Geology of the British Jurassic. (London: Geological Society of London.)

Warrington, G., 2005. Late Triassic (Rhaetian) palynomorphs from near York, North Yorkshire, UK. Proceedings of the Yorkshire Geological Society, 55(4), p. 305-306.

Warrington, G., 2019. Personal communication.

Warrington, G., Audley-Charles, M. G., Elliott, R. E., Evans, W. B., Ivimey-Cook, H. C., Kent, P. E., Robinson, P. L., Shotton, F. W. and Taylor, F. M., 1980, A correlation of Triassic rocks in the British Isles, in Rawson, P. F (eds): Geological Society, London, Special Report No. 13, 78 pages.

Whittaker, A. (ed.). 1985. Atlas of Onshore Sedimentary Basins in England and Wales: Post-Carboniferous Tectonics and Stratigraphy. Blackie, Glasgow and London.

Wignall, P.B. and Twitchett, R.J., 1996. Oceanic anoxia and the end Permian mass extinction. Science, 272(5265), p. 1155-1158.

Wignall, P.B. and Twitchett, R.J., 2002. Extent, duration, and nature of the Permian-Triassic superanoxic event. Special Papers-Geological Society of America, p. 395-414.

Williford, K.H., Ward, P.D., Garrison, G.H. and Buick, R., 2009. An extended organic carbon-isotope record across the Triassic–Jurassic boundary in the Queen Charlotte Islands, British Columbia, Canada. Palaeogeography, Palaeoclimatology, Palaeoecology, 244(1-4), p. 290-296.

Woods, P.J.E., 1973. Potash exploration in Yorkshire: Boulby mine pilot borehole: Institution of Mining and Metallurgy, 550.822.3: 533.632 (427.4).

Worden, R.H., Smalley, P.C. and Fallick, A.E., 1997. Sulfur cycle in buried evaporites. Geology, 25(7), p. 643-646.

Yao, W., Wortmann, U.G. and Paytan, A., 2019. Sulfur isotopes—Use for stratigraphy during times of rapid perturbations. In Stratigraphy & Timescales, Volume 4, p. 1-33. Academic Press.

Yin, H., Zhang, K., Tong, J., Yang, Z. and Wu, S., 2001. The Global stratotype section and point (GSSP) of the Permian–Triassic boundary. Episodes 24, p. 102–114.

Zhang, F., Romaniello, S.J., Algeo, T.J., Lau, K.V., Clapham, M.E., Richoz, S., Herrmann, A.D., Smith, H., Horacek, M. and Anbar, A.D., 2018. Multiple episodes of extensive marine anoxia linked to global warming and continental weathering following the latest Permian mass extinction. Science advances, 4(4), p. 1602921.

Ziegler, P. A., 1987. Evolution of the Western Approaches Trough. Tectonophysics, 137. p. 341-346.

Ziegler, P.A., 1990. Geological atlas of western and central Europe, 239 pp. Shell Internationale Petroleum Maatschappij BV.

Appendices

Appendix Figures

Appendix Figure 1. Vertical salt band (10 inches in length, 3 cm wide) at depth 3,442 ft (1,049 m).

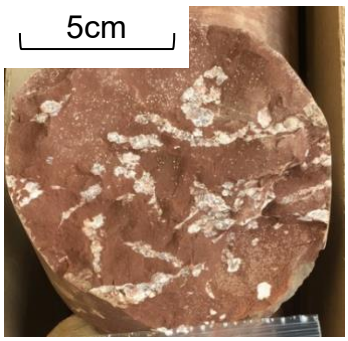

Appendix Figure 2. Micro/macroscale of salt nodules in fine sand mudstone, at depth 3,407 ft (1,038 m).

Appendix Figure 3. Microscale size anhydrite and gypsum crystals, at depth 3,383 ft (1031 m).

Appendix Figure 4. Green reduction spot (8cm wide), at depth 3,365 ft (1026 m).

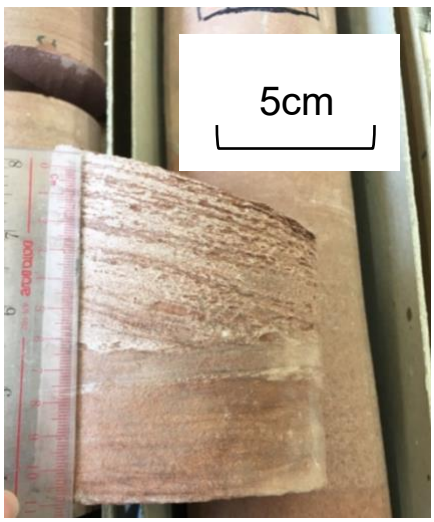

Appendix Figure 5. Cross bedding structure at depth 2,105 ft (642 m).

Appendix Figure 6. Grey crystalline anhydrite mudstone, at depth 2,069 ft (631 m).

Appendix Figure 7. Green reduction laminated layers in very fine-grained red mudstone, at depth 1,692 ft (516 m).

Appendix Figure 8. Laminated pale-green to green reduction layers, at depth 1,774 ft (541 m).

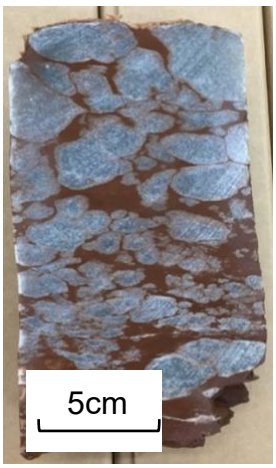

Appendix Figure 9. Large salt nodules cross section (4 cm in diameter) (wet surface), at depth 1,592 ft (485 m).

Appendix Figure 10. Large salt nodules, at depth 1,352 ft (412 m).

Appendix Figure 11. Salt nodules (~ 2 cm in diameter), at depth 1,311 ft (400 m).

Appendix Figure 12. Anhydrite band at depth 1,334 ft (407 m).

Appendix Figure 13. Anhydrite vein at depth 1,453 ft (443 m).

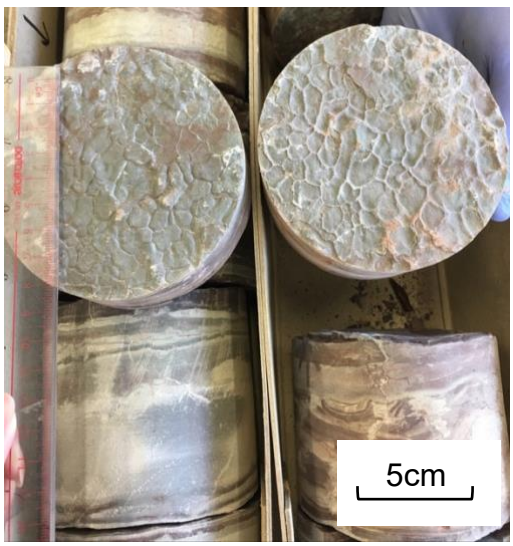

Appendix Figure 14. Mud desiccations at depth 1,863 ft (568 m).

Appendix Table

Table 1. Sulphur and organic carbon isotopic composition of late Permian to Late Triassic from sulphate evaporites from Staithes-20 Borehole

Sample ID	Depth (ft)	Depth (m)	Nodule, vein, bed	S (wt. %)	$^{\delta 34}$S (‰)	C (wt. %)	δ13C (‰)
109999	1236.83	376.99	109999	-	-	2.06	-25.96
110180	1257.50	383.29	110180 n	-	-	1.34	-22.91
110181	1259.08	383.77	110181 n	-	-	-	-
110182	1262.58	384.83	110182 n	-	-	1.43	-26.74
109917	1264.00	385.27	109917 n	-	-	1.92	-27.73
109918	1280.17	390.20	109918 b	18.46	15.86	2.82	-26.08
109919	1280.67	390.35	109919 b	18.51	16.13	-	-
109920	1300.00	396.24	109920 b	27.92	18.44	1.16	-26.91
109921	1300.17	396.29	109921	16.64	15.72	-	-
109922	1303.00	397.15	109922 b	28.10	17.05	0.67	-27.07
109923	1303.92	397.43	109923	22.66	15.60	-	-
109924	1304.67	397.66	109924 n	26.52	16.40	0.60	-27.01
109925	1305.17	397.82	109925 n	27.75	18.22	-	-
109926	1306.67	398.27	109926 n	24.84	16.72	1.50	-26.82
109927	1309.00	398.98	109927 n	27.48	15.98	0.59	-26.61
109693	1310.08	399.31	109693 n	27.47	16.14	-	-
109694	1311.00	399.59	109694 n	24.77	16.87	1.49	-27.35
109695	1312.08	399.92	109695 b	28.31	16.85	0.66	-26.99
109928	1313.00	400.20	109928 n	29.60	16.85	0.78	-26.96

109929	1316.42	401.24	109929 n	24.22	16.99	0.72	-26.93
109930	1319.00	402.03	109930 b	22.83	16.49	0.70	-27.02
109931	1320.67	402.54	109931 n	23.49	16.61	0.81	-26.35
109932	1322.33	403.05	109932 b	22.11	16.00	0.46	-24.36
109933	1327.00	404.47	109933 n	23.99	16.26	0.45	-27.05
109934	1328.58	404.95	109934 b	24.29	16.81	-	-
109935	1334.00	406.60	109935	21.54	15.47	-	-
110199	1335.42	407.04	110199 n	24.14	15.94	0.99	-21.86
110200	1340.42	408.56	110200 b	19.45	14.99	-	-
110201	1342.17	409.09	110201 b	23.73	15.06	-	-
110202	1345.67	410.16	110202 n	24.08	14.43	0.56	-26.71
110203	1347.08	410.59	110203	18.65	14.02	0.96	-25.61
110204	1350.50	411.63	110204	8.61	14.51	2.20	-28.39
110205	1352.00	412.09	110205	20.66	14.14	0.44	-26.76
110206	1357.00	413.61	110206 n	23.08	14.62	0.52	-26.79
110207	1364.00	415.75	110207 n	26.38	13.40	0.87	-26.86
110208	1365.67	416.26	110208 n	21.40	13.65	0.74	-26.81
110209	1368.00	416.97	110209 n	25.97	14.23	0.69	-26.70
110210	1370.00	417.58	110210	23.87	14.85	-	-
110211	1375.00	419.10	110211 n	25.07	14.47	-	-
110212	1379.00	420.32	110212 n	21.87	14.92	-	-
110213	1383.25	421.61	110213 v	24.26	14.70	-	-
110214	1389.50	423.52	110214	23.15	15.11	-	-
110215	1396.00	425.50	110215	22.34	14.29	-	-
110216	1397.92	426.09	110216 v	23.32	14.89	0.65	-26.58

110217	1402.00	427.33	110217 v	22.18	14.91	-	-
110218	1405.00	428.24	110218 v	21.18	14.81	-	-
110219	1413.67	430.89	110219 v	21.01	15.01	2.08	-22.52
110220	1416.17	431.65	110220 n	9.85	15.06	0.73	-26.39
110221	1419.50	432.66	110221 n	27.10	16.07	0.99	-26.45
110222	1421.25	433.20	110222 b	28.43	15.90	-	-
110223	1430.67	436.07	110223 v	22.03	16.02	-	-
110224	1431.25	436.25	110224	26.13	15.65	0.73	-26.93
110225	1433.25	436.85	110225 v	22.80	15.47	0.62	-26.69
110226	1453.08	442.90	110226 v	19.20	15.20	1.02	-26.88
110227	1456.67	443.99	110227 v	21.04	15.58	-	-
110228	1472.00	448.67	110228 v	21.23	15.57	0.49	-26.90
110229	1479.25	450.88	110229	12.51	16.61	0.83	-26.98
110230	1480.33	451.20	110230 b	21.65	16.21	0.23	-27.53
110231	1489.50	454.00	110231 v	22.05	16.02	-	-
110232	1492.25	454.84	110232	22.44	16.14	-	-
110233	1494.00	455.37	110233 v	22.62	16.14	-	-
110234	1494.25	455.45	110234 v	21.17	15.73	0.17	-27.34
110235	1501.00	457.50	110235 v	22.41	16.49	0.14	-28.36
110236	1507.58	459.51	110236 n	16.84	15.80	0.19	-27.94
110237	1510.50	460.40	110237 n	6.47	15.92	0.19	-27.78
110238	1517.33	462.48	110238 v	23.19	15.90	0.20	-28.27
110239	1519.00	462.99	110239 v	22.88	15.89	0.20	-27.73
110240	1520.17	463.35	110240 v	23.14	16.25	0.15	-27.63
110241	1525.83	465.07	110241	-	-	-	-

110242	1528.00	465.73	110242	-	-	-	-
110243	1530.75	466.57	110243 n	22.85	14.96	0.10	-28.17
110244	1532.00	466.95	110244 b	24.02	14.31	0.08	-27.53
110245	1532.17	467.01	110245	-	-	-	-
110247	1534.00	467.56	110247	21.32	15.03	-	-
110246	1538.08	468.81	110246 n	19.68	15.27	0.12	-28.07
110248	1548.17	471.88	110248 v	17.76	16.19	0.10	-27.85
110249	1549.42	472.26	110249 n	22.89	16.34	0.16	-28.22
110250	1551.58	472.92	110250 n	25.94	17.53	0.18	-28.39
110251	1553.08	473.38	110251 b	24.50	16.39	0.09	-28.32
110252	1558.83	475.13	110252 n	24.58	16.13	0.12	-28.63
110253	1561.67	476.00	110253 n	13.01	15.59	0.25	-28.72
110254	1583.00	482.50	110254 v	23.79	17.17	0.15	-28.03
110255	1587.58	483.89	110255 n	24.88	19.06	0.18	-28.43
110256	1588.17	484.07	110256 n	22.86	16.65	0.36	-28.43
110257	1589.58	484.50	110257 b	23.97	18.27	-	-
110258	1592.00	485.24	110258 n	23.77	17.04	-	-
110259	1593.25	485.62	110259 b	23.96	18.21	-	-
110260	1594.75	486.08	110260 n	24.06	17.50	-	-
110261	1596.67	486.67	110261 v	24.97	18.19	0.15	-28.23
110262	1599.33	487.48	110262 v	24.85	17.21	0.09	-27.74
110263	1602.42	488.42	110263 n	12.34	16.75	-	-
110264	1605.00	489.20	110264 n	4.29	16.99	0.17	-28.68
110265	1616.00	492.56	110265 n	3.20	15.80	-	-
110266	1618.00	493.17	110266 v	22.65	17.90	0.22	-28.67

110267	1620.00	493.78	110267 n	8.02	17.33	0.18	-28.68
110268	1622.00	494.39	110268 v	22.83	18.18	-	-
110269	1625.75	495.53	110269	21.46	17.00	-	-
110270	1626.33	495.71	110270 v	23.14	17.36	0.17	-26.54
110350	1628.50	496.37	110350 v	22.67	18.49	0.27	-28.08
110351	1633.00	497.74	110351 n	-	-	-	-
110352	1634.92	498.32	110352 n	22.36	17.13	-	-
110353	1638.58	499.44	110353 n	23.15	18.45	-	-
110354	1640.67	500.08	110354 n	9.31	17.17	0.59	-26.44
110355	1641.08	500.20	110355 n	6.34	16.84	-	-
110356	1649.42	502.74	110356 n	22.54	18.10	-	-
110357	1664.00	507.19	110357 n	20.93	18.94	-	-
110358	1667.83	508.35	110358 n	22.82	18.39	0.61	-28.00
110359	1680.17	512.12	110359 b	20.54	17.36	0.64	-28.38
110360	1681.00	512.37	110360 b	22.61	17.81	0.46	-28.19
110433	1692.00	515.72	110433 v	22.27	17.83	0.39	-28.48
110434	1698.00	517.55	110434 v	22.73	18.07	-	-
110435	1703.75	519.30	110435 v	23.07	18.15	0.53	-28.40
110436	1709.75	521.13	110436 n	16.55	18.14	-	-
110437	1717.00	523.34	110437 v	25.15	18.75	0.87	-29.64
110438	1725.25	525.86	110438 n	17.83	18.10	-	-
110439	1729.67	527.20	110439 v	24.44	20.30	0.52	-26.33
110440	1736.17	529.18	110440 b	23.84	18.82	-	-
110441	1738.67	529.95	110441 n	23.31	18.60	0.68	-27.85
110442	1739.00	530.05	110442 n	21.57	19.60	0.64	-28.33

110443	1742.42	531.09	110443 n	24.31	20.53	0.35	-28.57
110444	1745.25	531.95	110444 n	20.65	18.56	0.39	-28.57
110445	1746.00	532.18	110445 n	23.31	20.25	0.47	-28.17
110446	1747.58	532.66	110446 n	17.09	18.67	0.58	-27.69
110447	1750.67	533.60	110447 v	25.19	19.65	0.58	-29.84
110448	1753.08	534.34	110448	21.51	18.67	-	-
110449	1753.83	534.57	110449 n	14.23	18.83	0.31	-28.31
110450	1756.00	535.23	110450 n	22.61	18.97	0.80	-30.15
110451	1757.50	535.69	110451 n	20.85	18.55	0.39	-28.55
110452	1758.33	535.94	110452 n	22.61	18.48	0.36	-28.22
110453	1760.42	536.58	110453 n	23.28	19.00	0.48	-30.39
110454	1762.50	537.21	110454 v	22.61	19.25	0.20	-30.33
110455	1763.58	537.54	110455 b	20.12	19.13	0.30	-30.02
110456	1764.67	537.87	110456 n	21.69	19.74	0.53	-29.77
110457	1765.75	538.20	110457 n	10.51	19.47	-	-
110458	1769.67	539.40	110458 b	19.95	19.68	0.53	-28.52
110459	1771.00	539.80	110459 n	17.46	19.33	0.28	-27.23
110460	1774.08	540.74	110460 n	22.98	19.48	0.41	-30.20
110461	1776.00	541.32	110461 n	22.65	19.42	0.26	-30.02
110462	1781.42	542.98	110462 b	21.72	19.81	0.29	-28.45
110463	1783.00	543.46	110463 b	16.27	19.37	0.46	-30.34
110464	1784.00	543.76	110464 b	19.28	19.88	0.26	-28.90
110465	1786.08	544.40	110465 b	20.01	20.37	0.67	-30.06
110466	1787.08	544.70	110466 b	20.92	20.36	-	-
110467	1787.50	544.83	110467 n	22.22	19.40	0.69	-29.79

110468	1791.50	546.05	110468 b	9.64	19.06	0.36	-28.48
110469	1794.00	546.81	110469 b	12.21	19.02	-	-
110470	1796.00	547.42	110470 b	23.49	19.68	-	-
110471	1796.92	547.70	110471 n	23.58	20.39	-	-
110472	1814.00	552.91	110472 v	19.23	20.48	0.33	-28.32
110473	1818.00	554.13	110473 n	17.25	19.56	0.53	-28.75
110474	1825.33	556.36	110474	19.16	19.40	-	-
110475	1825.92	556.54	110475 v	16.79	20.25	0.53	-28.69
110476	1828.00	557.17	110476 v	21.37	19.85	-	-
110477	1830.33	557.88	110477 v	23.30	20.01	-	-
110478	1841.00	561.14	110478 n	18.65	19.68	0.29	-28.73
110479	1846.92	562.94	110479 n	21.31	20.06	0.15	-28.82
110480	1847.25	563.04	110480 n	14.03	19.97	0.17	-28.55
110481	1849.25	563.65	110481 b	19.85	20.05	0.23	-28.78
110482	1850.08	563.90	110482 b	19.70	19.79	-	-
110483	1851.42	564.31	110483 b	23.96	20.20	0.62	-28.67
110484	1854.42	565.23	110484 n	22.47	18.62	0.40	-28.57
110485	1856.00	565.71	110485	23.29	20.13	-	-
110486	1857.83	566.27	110486 n	23.54	20.13	0.20	-29.29
110487	1858.83	566.57	110487 b	21.39	20.16	0.25	-28.76
110488	1864.67	568.35	110488 v	22.67	20.37	-	-
110489	1874.00	571.20	110489	3.93	20.79	0.42	-26.94
110490	1875.00	571.50	110490 n	22.41	19.68	0.28	-29.17
110491	1895.42	577.72	110491 v	23.45	20.22	0.37	-28.66
110492	1914.00	583.39	110492 v	19.84	21.32	0.38	-29.06

110493	1920.50	585.37	110493 v	22.70	21.49	0.30	-28.73
110494	1927.00	587.35	110494	21.76	22.59	0.29	-28.84
110495	1936.00	590.09	110495 n	22.83	20.85	0.27	-29.11
110496	1941.00	591.62	110496 n	19.41	21.52	0.21	-29.05
110497	1958.00	596.80	110497 n	18.03	21.12	0.46	-28.79
110498	1959.33	597.20	110498 b	19.42	21.33	0.50	-28.68
110499	1960.33	597.51	110499 n	26.04	21.56	0.25	-29.08
110500	1962.75	598.25	110500 b	21.99	21.93	0.25	-28.96
110501	1963.25	598.40	110501 b	22.73	21.15	0.09	-28.33
110502	1964.00	598.63	110502 b	19.84	20.11	0.26	-28.97
110503	1964.42	598.76	110503 b	26.99	20.81	0.23	-29.08
110504	1965.58	599.11	110504 v	19.88	21.47	0.29	-28.94
110505	1978.42	603.02	110505 b	22.60	22.40	0.31	-28.84
110506	1979.40	603.32	110506 n	26.85	23.33	0.23	-29.31
110507	1985.58	605.20	110507 v	19.81	22.87	0.25	-30.79
110508	1995.42	608.20	110508 n	15.57	23.04	0.42	-27.32
110509	1998.67	609.19	110509 v	22.72	24.58	0.56	-29.03
110510	2004.00	610.82	110510 v	23.10	24.92	0.52	-28.94
110511	2006.75	611.66	110511 v	22.90	24.29	0.13	-28.54
110512	2009.00	612.34	110512 v	20.63	24.38	1.05	-28.34
110513	2010.75	612.88	110513 v	20.13	24.54	-	-
110514	2015.00	614.17	110514 b	21.43	24.94	0.15	-27.66
110515	2026.25	617.60	110515 n	20.88	28.43	0.40	-27.93
110516	2030.83	619.00	110516 v	17.73	26.28	0.25	-25.43
110517	2046.67	623.83	110517 n	19.52	26.23	-	-

110518	2049.00	624.54	110518 b	21.91	26.69	0.24	-28.61
110551	2062.17	628.55	110551 v	17.51	26.84	-	-
110552	2064.00	629.11	110552 b	19.06	27.70	5.29	-22.42
110553	2068.75	630.56	110553 b	21.65	24.26	-	-
111143	2069.75	630.86	111143	21.42	22.72	0.19	-27.59
111144	2071	631.24	111144	4.90	18.54	0.52	-27.36
111145	2071.58	631.42	111145	4.77	22.94	-	-
111146	2072.33	631.65	111146	-	-	-	-
111147	2073.5	632.00	111147	5.00	18.47	-	-
111148	2073.92	632.13	111148	22.06	18.85	-	-
111149	2074.42	632.28	111149	15.36	17.47	-	-
111150	2075.5	632.61	111150	2.13	17.00	-	-
110554	2076.50	632.92	110554 n	16.99	16.20	0.34	-26.63
110555	2076.75	632.99	110555 n	20.91	16.18	-	-
111151	2077.5	633.22	111151	23.37	17.70	-	-
111152	2078.17	633.43	111152	21.79	16.86	0.15	-27.61
111153	2078.83	633.63	111153	21.84	16.84	0.15	-28.79
111154	2079	633.68	111154	19.42	16.15	-	-
111155	2080.52	634.14	111155	16.48	15.99	0.10	-28.35
111156	2080.75	634.21	111156	20.68	16.33	0.14	-28.57
111157	2081.5	634.44	111157	16.38	15.52	0.70	-28.28
110556	2083.00	634.90	110556 n	20.94	15.67	-	-
111158	2084.25	635.28	111158	23.58	16.20	0.17	-28.39
111159	2085	635.51	111159	-	-	-	-
110557	2085.33	635.61	110557 n	21.87	17.29	0.44	-24.62

110558	2087.08	636.14	110558 n	21.29	16.44	0.41	-24.08
110559	2088.83	636.68	110559	22.81	17.66	0.88	-23.55
110560	2096.00	638.86	110560 n	18.66	15.74	0.39	-22.03
110561	2101.00	640.38	110561 v	17.28	15.68	0.14	-25.38
110562	2105.00	641.60	110562 v	17.00	16.18	0.23	-22.09
110563	2111.67	643.64	110563 v	18.10	15.47	0.12	-24.35
111160	2120.58	646.35		-	-	0.71	-29.36
111161	2157.33	657.55	111161	14.24	14.34	0.70	-28.61
111162	2181	664.77	111162	18.77	14.92	-	-
111163	2214.83	675.08	111163	4.35	10.78	0.37	-28.56
111164	2272	692.51	111164	3.45	12.80	0.05	-24.27
111165	2359	719.02	111165	16.16	12.35	-	-
111166	2403.17	732.49	111166	3.61	11.14	-	-
111167	2461	750.11	111167	19.08	10.97	0.21	-25.35
108656	2560.5	780.44	108656	-	-	0.12	-28.40
108657	2682	817.47	108657	9.10	12.16	0.30	-27.60
108658	2874.42	876.12	108658	4.77	10.78	0.32	-27.15
108659	2881.58	878.31	108659	11.31	10.04	0.24	-27.18
108660	2882.25	878.51	108660	4.80	10.65	0.24	-26.83
108661	2893.83	882.04	108661	6.37	10.94	0.27	-27.00
108662	2894.25	882.17	108662	2.27	11.46	0.31	-27.06
108663	2894.83	882.34	108663	3.75	10.45	0.48	-27.06
111312	2896.00	882.70	111312	1.72	11.04	0.19	-27.09
111313	2898.58	883.49	111313	-	-	0.30	-27.15
111314	2936.33	894.99	111314	21.68	9.57	0.22	-26.95

111315	2936.92	895.17	111315	18.80	10.00	0.15	-27.10
111316	2939.33	895.91	111316	11.30	10.27	0.27	-27.12
111317	2943.83	897.28	111317	12.73	9.67	0.22	-27.27
111320	2960.00	902.21	111320	1.27	9.97	0.33	-27.08
111321	2990.00	911.35	111321	1.06	9.83	0.26	-27.02
111322	2994.42	912.70	111322	-	-	0.90	-27.59
111323	2995.42	913.00	111323	4.33	10.49	0.38	-27.19
111324	2998.67	913.99	111324	2.82	15.30	0.21	-27.11
111318	3022.25	921.18	111318	1.63	10.13	-	-
111319	3023.83	921.66	111319	5.53	8.98	-	-
111325	3059.33	932.48	111325	20.05	16.87	-	-
111326	3074.08	936.98	111326	8.02	8.87	-	-
111327	3074.25	937.03	111327	4.99	9.38	-	-
111328	3077.50	938.02	111328	6.14	8.81	0.26	-26.56
111329	3078.00	938.17	111329	8.76	8.43	-	-
111330	3079.75	938.71	111330	11.61	8.66	0.27	-26.92
111331	3103.83	946.05	111331	14.47	8.90	-	-
111332	3108.25	947.39	111332	13.82	7.51	0.22	-27.03
111333	3108.50	947.47	111333	13.75	7.99	0.12	-27.21
111334	3114.75	949.38	111334	12.01	16.98	-	-
111335	3116.25	949.83	111335	9.35	11.64	0.21	-26.58
111336	3131.67	954.53	111336	4.77	11.74	0.58	-27.34
111337	3149.00	959.82	111337	17.39	9.86	0.64	-27.69
111338	3150.33	960.22	111338	14.00	11.49	0.22	-27.71
111339	3156.00	961.95	111339	17.18	11.20	0.58	-27.85

111340	3163.50	964.23	111340	-	-	0.74	-27.56
111341	3165.00	964.69	111341	18.87	11.46	0.85	-28.10
111342	3165.67	964.90	111342	16.53	10.93	-	-
111343	3166.58	965.17	111343	22.31	11.03	0.46	-28.46
111344	3171.42	966.65	111344	11.49	12.02	0.85	-27.87
111345	3174.25	967.51	111345	19.38	11.46	0.57	-27.67
111346	3181.17	969.62	111346	14.12	13.59	0.42	-28.15
111347	3182.00	969.87	111347	6.56	13.06	0.14	-28.39
111348	3185.00	970.79	111348	9.28	14.25	0.68	-27.84
111349	3188.50	971.85	111349	22.06	10.45	0.52	-27.83
111350	3194.58	973.71	111350	9.91	9.13	0.47	-27.57
111351	3195.75	974.06	111351	17.67	9.77	-	-
111352	3198.42	974.88	111352	19.79	7.99	0.63	-28.29
111353	3206.08	977.21	111353	21.55	8.94	0.60	-27.98
111354	3208.00	977.80	111354	20.01	8.84	0.10	-28.45
111355	3214.67	979.83	111355	20.13	9.61	0.51	-27.56
111356	3214.83	979.88	111356	22.71	9.57	0.45	-27.74
111357	3215.75	980.16	111357	15.39	7.94	0.54	-27.60
111358	3217.58	980.72	111358	15.54	9.13	0.10	-28.42
111359	3225.17	983.03	111359	15.16	10.97	-	-
111360	3226.67	983.49	111360	18.24	10.45	0.41	-28.56
111361	3228.00	983.89	111361	15.76	10.21	0.32	-28.52
111362	3246.33	989.48	111362	23.09	10.98	0.54	-28.52
111363	3251.92	991.19	111363	13.01	9.86	0.63	-27.39
111364	3253.67	991.72	111364	12.56	8.54	0.59	-27.98

111365	3253.83	991.77	111365	9.75	8.32	-	-
111366	3254.92	992.10	111366	15.86	8.91	0.54	-28.34
111367	3258.33	993.14	111367	13.86	9.34	-	-
111368	3258.75	993.27	111368	11.02	9.55	0.71	-27.59
111369	3266.58	995.65	111369	-	-	-	-
111370	3267.75	996.01	111370	21.92	8.70	-	-
111371	3269.50	996.54	111371	18.32	8.50	-	-
111372	3273.25	997.69	111372	15.22	7.66	-	-
111373	3275.42	998.35	111373	19.20	8.56	0.78	-27.84
111374	3277.50	998.98	111374	17.36	7.86	0.61	-27.87
111375	3282.42	1000.48	111375	12.04	8.71	0.25	-27.05
110361	3285.33	1001.37	110361 n	18.19	7.90	0.12	-26.86
110362	3289.00	1002.49	110362 n	13.84	9.68	0.29	-28.89
111376	3293.67	1003.91	111376	21.01	10.74	-	-
111377	3297.50	1005.08	111377	21.53	10.46	-	-
110363	3297.58	1005.10	110363 n	18.84	12.86	0.21	-28.45
111378	3303.75	1006.98	111378	14.55	11.27	0.43	-28.02
111379	3306.50	1007.82	111379	21.19	11.21		
110364	3310.00	1008.89	110364 n	18.51	11.59	0.10	-25.66
110365	3315.00	1010.41	110365 n	17.44	11.52	0.21	-28.44
110366	3315.50	1010.56	110366 n	21.80	11.02	0.21	-28.39
111380	3318.50	1011.48	111380	10.72	10.74	0.39	-27.11
111381	3324.50	1013.31	111381	15.66	10.08	-	-
110367	3324.67	1013.36	110367 n	16.34	10.67	0.30	-29.24
111382	3326.50	1013.92	111382	11.26	10.29	0.36	-28.58

111383	3328.00	1014.37	111383	22.56	11.19	0.52	-28.61
110368	3335.92	1016.79	110368	21.49	11.87	0.15	-26.66
111384	3337.50	1017.27	111384	20.07	9.20	0.79	-29.37
111385	3340.92	1018.31	111385	17.65	7.93	0.31	-27.17
110369	3345.00	1019.56	110369 n	17.69	7.41	0.30	-28.91
111386	3349.00	1020.78	111386	14.18	7.47	-	-
111387	3352.00	1021.69	111387	19.12	7.04	-	-
110370	3355.00	1022.60	110370 n	20.20	7.12	0.18	-26.68
110371	3360.00	1024.13	110371 n	15.85	8.15	0.13	-26.77
110372	3370.67	1027.38	110372 n	15.97	8.89	0.28	-28.52
110373	3372.92	1028.07	110373 n	21.67	10.06	0.28	-28.94
110374	3374.00	1028.40	110374 v	21.83	10.24	0.55	-25.84
110375	3376.00	1029.00	110375 n	18.57	9.42	0.27	-28.51
110376	3381.75	1030.76	110376 n	19.64	9.78	0.17	-25.34
110377	3383.50	1031.29	110377	20.18	10.02	0.20	-28.58
110378	3384.58	1031.62	110378 n	21.54	9.56	0.40	-28.58
110379	3392.00	1033.88	110379 n	20.67	9.40	0.40	-27.31
110380	3402.33	1037.03	110380	19.85	9.95	0.23	-27.00
110381	3405.00	1037.84	110381 n	23.82	10.14	0.20	-28.59
110382	3406.00	1038.15	110382 n	23.00	9.97	0.20	-27.50
110383	3407.00	1038.45	110383 n	24.21	10.14	0.28	-28.51
110384	3411.17	1039.72	110384 n	22.40	10.10	0.14	-26.92
110385	3416.83	1041.45	110385 n	21.05	9.81	0.15	-28.50
110386	3418.92	1042.09	110386 n	22.69	10.90	0.30	-27.02
110387	3429.42	1045.29	110387	20.86	10.63	0.25	-27.03

110388	3435.25	1047.06	110388 v	21.31	10.08	0.30	-29.66
110389	3435.92	1047.27	110389 b	26.00	11.13	0.10	-26.43
110390	3436.50	1047.45	110390 v	18.94	10.76	-	-
110391	3437.00	1047.60	110391 v	25.81	11.15	-	-
110392	3438.50	1048.05	110392 n	18.08	10.87	0.09	-26.44
110393	3439.92	1048.49	110393 n	20.76	10.62	0.23	-28.96
110394	3441.50	1048.97	110394 v	19.94	10.20	0.11	-26.21
110395	3442.00	1049.12	110395 b	-	-	0.33	-29.12
110396	3443.00	1049.43	110396 v	22.87	10.34	0.17	-29.00
110397	3445.25	1050.11	110397 b	-	-	0.20	-30.05
110398	3446.00	1050.34	110398 b	2.08	10.42	0.07	-29.28
110399	3446.67	1050.55	110399 b	-	-	0.43	-30.57
110400	3448.00	1050.95	110400 b	-	-	0.37	-29.80
110401	3448.50	1051.10	110401	2.50	11.01	-	-
110402	3449.00	1051.26	110402 b	-	-	0.24	-6.73
110403	3451.00	1051.86	110403 b	-	-	0.11	-12.83
110404	3452.50	1052.32	110404 b	-	-	0.90	-1.69
110405	3454.00	1052.78	110405 b	-	-	0.22	-11.43
110407	3455.75	1053.31	110406	7.99	9.82	0.11	-11.70
110406	3455.83	1053.34	110407	8.52	9.45	0.24	-8.40
110408	3456.00	1053.39	110408	-	-	0.09	-21.27
110409	3456.50	1053.54	110409	9.91	9.25	0.12	-22.27
110410	3456.92	1053.67	110410	10.11	8.91	0.22	-15.37
110411	3457.42	1053.82	110411	4.00	9.51	0.21	-17.90
110412	3458.00	1054.00	110412	8.35	9.17	0.44	-26.06

110413	3458.42	1054.13	110413	8.40	8.70	0.05	-29.08
110414	3459.00	1054.30	110414	1.42	9.99	-	-
110415	3462.00	1055.22	110415 b	-	-	0.10	-29.27
110416	3463.00	1055.52	110416	-	-	0.23	-7.28
110417	3464.00	1055.83	110417	-	-	0.20	-7.61
110418	3464.50	1055.98	110418	11.34	8.91	1.19	-12.36
110419	3465.00	1056.13	110419	2.65	9.41	0.17	-29.80
110420	3465.42	1056.26	110420 b	-	-	0.10	-14.65
110421	3466.00	1056.44	110421 b	-	-	0.21	-22.47
110422	3466.17	1056.49	110422	-	-	0.10	-20.01
110423	3467.00	1056.74	110423	10.85	9.26	0.10	-19.20
110424	3467.75	1056.97	110424	-	-	0.11	-24.65
110425	3468.75	1057.28	110425	9.06	9.16	0.12	-28.86
110426	3469.17	1057.40	110426	6.89	9.07	0.13	-27.40
110428	3470.75	1057.88	110428 b	-	-	0.10	-24.10
110427	3470.83	1057.91	110427	-	-	0.86	-29.58
110429	3471.33	1058.06	110429	7.05	9.47	0.09	-28.11
110430	3472.00	1058.27	110430	7.94	9.36	0.19	-27.55
110431	3472.58	1058.44	110431	-	-	0.24	-29.77
110432	3473.00	1058.57	110432	-	-	-	-